Doctoral Dissertation

Numerical study on nonlinear wave-body interaction in time domain based on ALE-HOBEM

Zhang Jie

July 2017

Department of Naval Architecture and Ocean Engineering
Division of Global Architecture
Graduate School of Engineering,
Osaka University

"To build a ship, first to be a man with ocean inside."

Zhang Jie

OSAKA UNIVERSITY

Abstract

Graduate School of Engineering
Department of Naval Architecture and Ocean Engineering

Doctor of Engineering

by Zhang Jie

When extreme incident waves and/or large-amplitude body motions are involved, nonlinear effects in hydrodynamics of wave-body interaction problems become critically important in the design of ships and offshore structures. In the present research, a solver named ALE-HOBEM is developed based on potential-flow theory and applied to study fully nonlinear wave-body interaction problem, where large-amplitude motion, moving boundary, complex geometry and nonlinear incident waves are involved.

To develop this solver, two problems should be solved: (i) proper treatment on moving boundary, which requires not only the exact position of free surface should be tracked but the mesh on free surface should be able to self-adapt to body's large-amplitude motion; (ii) accurate evaluation on hydrodynamic force (moment), which is related to calculation of temporal derivative of velocity potential. Regarding problem (i), an Arbitrary Lagrangian-Eulerian (ALE) scheme is proposed in the research, which is regarded as an optimized combination of the mixed-Euler-Lagrange (MEL) and semi-Lagrange (SL) scheme. Regarding problem (ii), the temporal derivative of velocity potential is directly evaluated by solving a reconstructed boundary value problem (BVP) with much simplicity compared to the original method. In addition, a higher-order boundary element method (HOBEM) is used as a BVP solver.

Three nonlinear wave-body interaction problems with increasing of complexity are investigated in detail: nonlinear wave diffraction, nonlinear wave radiation and interaction between nonlinear incident waves and a freely floating body. In the computation, several body's geometries (from circular cylinder to practical ship) are used. By a systematic validation, the ALE-HOBEM is proved to be accurate and robust in study nonlinear wave-body interaction problems.

Acknowledgements

First and foremost, I would like to thank my supervisor, Professor Masashi Kashiwagi, for his rigorous academic attitude, sense of responsibility, and encouragement along the journey to get my Ph.D degree. Whenever I am frustrated by slow research progress, he is there to encourage me and push me forward. I also cannot thank him enough for the continuous support for my living in Japan. There is an old Chinese saying, "a teacher of one day, a mentor of lifetime". This is exactly how I feel towards Professor Masashi Kashiwagi.

I am also indebted and thankful to Professor Munehiko Minoura in the laboratory who was giving critical and constructive comments during laboratory meeting. I also very much appreciate his support in emergency when my computer was in trouble.

I would also like to thank Professor Hinatsu Munehiko for his kind support in acceleration of reviewing my paper.

Special thanks to Dr. Guanghua He, his work in the Lab avoid me starting from zero. I am so grateful to Dr. Lucas Letournel for the fruitful discussions and valuable advices on my research. Many thanks to Mr. Zhen Yang for his help to provide results from HydroSTAR.

My great appreciation goes to Ms.Yoshimura Ohta and Ms. Tamae Miyabe for their kind support in my daily life.

Furthermore, I should say that I have been blessed with friendly and cheerful laboratory members. Special thanks goes to Mr. Junki Yoshida, Yuta Seki, Asaumi Taiga, Dali Zhou and Ms. Mariko Miki, Jing Zhu for their support in my experiment. Special thanks to Mr. Iida Takahito and Ardhana Wicaksono that we have studied together for successive 3 years and wish them good luck. Many thanks to Mr. Ryohei Iwane, Keita Inoue, Kyohei Ishigami for their help when I came to Japan. Also many thanks to Dr. Chen Chen and Mr. Mingchun Zhou and Ms. Jianping Ma, we have shared many happy times together, which helps me remain positive at any time.

Most importantly, I must thank to my wife Xiaoxiao Ren whose endless understanding and encouragement supported me to come this far. My gratitude also goes to my parents and my sister whose everlasting love and prayers made my life path possible.

The research is supported by China Scholarship Council and Osaka University.

Finally I would like to take this opportunity to pay my sincere tribute to my grandfather, who passed away when I was preparing for my graduation and to whom I dedicate this thesis.

Osaka, August 2017

Jie Zhang

Contents

List of Figures

List of Tables

Abbreviations

FNPT	fully nonlinear potential theory
NS	Navier-Stokes
BEM	boundary element method
BVP	boundary value problem
MEL	mixed-Euler-Lagrange
SL	semi-Lagrange
MSL	modified semi-Lagrange
ALE	arbitrary-Lagrange-Eutherian
3D	three dimensioanl
2D	two dimensioanl
HOBEM	higher-order boundary element method
CAD	computer aid design
CAE	computer aid engineering
IGA	iso-geometric approach
NURBS	non-uniform rational B-spline
TBEM	Taylor expansion boundary element method
pFFT-BEM	precorrected-fast fourier transformation boundary element method
FMM	fast multipole method
GMRES	generalized minimal residual
DOF	degree of freedom
SC	sectional line
CPM	constant panel method
KC	Keulegan-Carpenter

Symbols

A	amplitude of incident wave or amplitude of body's oscillation	m
a	number of collocation point	
a_{ij}	hydrodynamic added mass	kg
A_n	non-dimensionalized sectional area curve of optimized hull	
B	ship breadth	m
B_{ij}	hydrodynamic damping coefficient	kgs^{-1}
$c(p)$	solid angle at p	
D	diameter	m
dl	distance	m
ds	distance	m
E_i	ith element	
F_i	hydrodynamic force or moment	
f_i	hydrodynamic force	kgs^{-2}
G	center of gravity or Green function	
g	gravitational acceleration	ms^{-2}
H	wave hight	m
H_i	angular momentum	$\mathrm{kgm}^2/\mathrm{s}$
$\{H\}$	coefficient matrix	
I^b	inertia matrix	
$\boldsymbol{J}$	Jacobian	
k	wave number	
$\boldsymbol{L}$	vector	
$\boldsymbol{l}$	tangential vector	
L_m	shape function	
$\boldsymbol{n}$	normal vector	

m	mass	kg
$\boldsymbol{M}$	moment	kgm^2/s^2
$\boldsymbol{n}$	normal vector	m
O	Order of some variable	
o	origin of earth-fixed coordinate system	
o^b	origin of body-fixed coordinate system	
OG	distance of center buoyancy to center of gravity	m
p	pressure or point	
q	source point	
R	distance	m
r	distance	m
S_b	ship wetted surface	m^2
S_f	free surface	m^2
S_c	control surface	m^2
S_h	bottom surface	m^2
t	time	s
T	period	s
Tr	matrix	
u	parameter	
$\boldsymbol{U}$	translational velocity of the body	m/s
$\boldsymbol{V}$	velocity at point on body surface	m/s
$\boldsymbol{V}_p$	velocity at point on p	m/s
$\boldsymbol{x}$	coordinates in earth-fixed system	m
$\boldsymbol{x}^b$	coordinates in body-fixed system	m
$\boldsymbol{X}$	coordinates in earth-fixed system	m
α	parameter	
β	parameter	
λ	wavelength	m
∇	gradient operator	
ω	angular frequency	$rads^{-1}$
Ω^b	rotational velocity	$rads^{-1}$
$\phi,\ \psi$	velocity potential	m^2s^{-1}

Φ_t	temporal derivative of velocity potential	m^2s^{-2}
ρ	water density	kgm^{-3}
η	wave elevation	m
ξ_i	displacement of motion in i-th mode	m
δ_{ij}	Kronecker delta function	
κ	scalar	
χ	scalar	
Ψ	variable	
ς	parameter	
τ	parameter	
ε	small parameter	
θ	angle	degree
σ	source strength	
μ	damping parameter	
ζ_a	wave amplitude	m

Chapter 1

Introduction

1.1 Background

When extreme incident waves and/or large-amplitude body motions are involved, nonlinear effects in hydrodynamics of wave-body interaction problems become critically important in the design of ships and offshore structures. Numerical simulations taking into account nonlinear effects e.g. large-amplitude motion, moving boundary, complex geometry and nonlinear incident waves, are still challenging due to complex physics behind of the problem.

In ocean engineering, for the problems that no wave breaking and flow separation exist or viscosity and strong free-surface nonlinearities are confined in a small flow region, the numerical simulation based on fully nonlinear potential theory (FNPT) is still an economical choice, compared to the Naiver-Stokes (NS) equation based solver.

In the framework of FNPT, even the mathematical model is much simplified compared to the original problem, there still some problems remain open or not well resolved. Note that at present research we only focus on wave-structure interaction without a forward speed. When developing a scheme to solve problems of nonlinear wave interaction with structures, one need to firstly consider the following issues:

- Free surface tracking scheme

  In order to track an exact position of free surface, generally, the free surface is represented by a group of fluid particles (Lagrangian's view) or infinitesimal probes (Euler' s view), where their movement denotes free surface deformation. However, when a moving body is involved, the free surface near the body would be split and/or merged frequently. The associated problem is to make fluid marker self-adapt to body's motion. Otherwise, the subsequent problems would occur, for instance, incorrect intersection updating and low-quality mesh near the body.

- Decouple the mutual dependence of fluid/structure motion

  This problem is related to the so-called *acceleration* potential problem. Although a variety of schemes have been proposed as we will introduce later, to reproduce some of them is not a easy task in a three-dimensional computation because of complexity of the scheme.

- Accuracy and efficiency of boundary element method (BEM)

  BEM is a popular solver in the framework of FNPT. In most of practical applications, it is required that the BEM solver should be capable of evaluating not only the unknowns of fluid field but spatial derivatives of the solution. Generally speaking, the spatial derivatives with order beyond one is difficult to evaluate with a promising accuracy. However, the second spatial derivatives is common in marine hydrodynamics e.g. m-term. On the other hand, the efficiency is another concern when developing a BVP solver based on BEM. As known, in BEM the resulting matrix of coefficient is fully populated and unsymmetrical, and thus to build up and solve this matrix would consume most of the computational time.

- Proper radiation condition at far field

  In computation, the computational domain is usually truncated at a distance far from the body. To avoid unwanted wave reflection from this boundary, an appreciate boundary condition should be imposed.

1.2 Literature review

1.2.1 On free surface updating scheme

Typically, there are two extensively used approaches for free surface updating, Mixed-Euler-Lagrange (MEL) approach ((Longuet-Higgins and Cokelet[1]) and Semi-Lagrange (SL) approach. The former allows multi-value of the free surface i.e., wave overturning, while the later requires the single-value of the free surface. Since in SL method, the horizontal motion of fluid particle is prescribed and it only moves freely in vertical direction, this scheme is mainly applied to wave generation without a body or wave interaction with simple-geometrized body [2][3].

Xue [4] and Liu, Xue and Yue [5] used the Mixed-Euler-Lagrange approach to study the generation of three-dimensional ship bow waves. For avoiding clustering of the Lagrange particle, a regridding scheme is used. For updating the intersection point between free surface and body surface, an arbitrary-Lagrange-Eutherian (ALE) scheme is proposed. Yan [6] also used this method to study nonlinear wave-structure interaction. Bai and Taylor [7], Zhou and Ning [8] studied nonlinear wave radiation by MEL scheme. Wang [9] develop an unstructured Mixed-Euler-Lagrange approach. As the name indicates, they use unstructured grid on free surface

combined with a desingular BEM solver. It is claimed that this method is more efficient and robust than structured one.

Besides MEL and SL scheme, there are also some other schemes for free surface updating worthy to mention. Sung and Grilli [10] applied an alternative method to study nonlinear wave-body interaction, by combining semi-Lagrangian and Lagrangian free surface boundary conditions to the problem of a pressure perturbation moving on the water surface. In their model, Lagrange approach is used near the body since nonlinearity is dominated in this region, while Semi-Lagrange approach is used at region far from the ship. Spring assumption is another representative method that all nodes on free surface are considered to be connected by springs and the free surface deforms like a spring system, for instance, Ma and Yan [11]. In order to remove the *wall-sided* restriction in SL scheme, Zhang [12] developed a modified SL and applied this scheme to study sloshing in a non-wall-sided tank.

1.2.2 On acceleration potential

To solve wave induced motions of floating body, one should first get wave induced loads acting on the body by Bernoulli's equation. The temporal derivative of velocity potential i.e. ϕ_t in Bernoulli's equation should be well evaluated. For achieving a promising accuracy of this term, a BVP for evaluating this term is constructed by Van Daalen [13] and Tanizawa [14]. However in body boundary condition for ϕ_t it contains unknown body acceleration which in turn requires wave induced force or ϕ_t. It reflects the coupling between fluid and body motion. Fortunately, we have a supplementary equation, body motion equation based on Newton's law. Substituting body motion equation into body boundary condition yields a closed BVP for ϕ_t. This is the method used by Van Daalen [13] and Tanizawa [14]. Because this term is related to fluid acceleration, sometimes it called as 'acceleration potential'.

Wu [15][16] proposed an explicit method to directly get hydrodynamic force acting on the body following above principle. In his method, an auxiliary function is introduced, which satisfies very simple boundary conditions. Bandyk and Beck [17] gave an overview of existing method. Letournel and Ducrozet et.al [18] proved that the existing BVPs for evaluating ϕ_t with different form are identical in principle.

Another issue in dealing with ϕ_t is that there is second special derivative terms appearing in body's boundary condition, which relates to curvature of local surface. In 3D computations, the expression for calculating this term is very much complicated, see Berkvens [19] and Shirakura and Tanizawa [20]. In order to circumvent this difficulty, Wu and Hu [21] introduced an auxiliary function and transformed this term into free surface. As a result, the second order derivative terms are reduced by order one.

More recently, Sclavounos [22][23] developed a nonlinear impulse theory for motions of floating body. In his formulation, $\iint \partial\phi/\partial t ds$ is converted to $d/dt \iint \phi ds$ by momentum conservation, which circumvents the need for calculating $\partial\phi/\partial t$.

1.2.3 On BVP solver

After the pioneering work of Hess and Smith [24], the subsequent researchers pay more attention to either improving accuracy or increasing efficiency of the BEM. Initially, the higher-order boundary element method (HOBEM) is a logical improvement compared to constant panel method, where both geometry and filed variable are discreted by piecewise polynomial defined over specific element. Many published works has done by HOBEM since it is easily extended from constant panel method with improved accuracy and convergency. However, HOBEM can not provide good smoothness of the solution because of C^0 continuity at collocation node.

To circumvent this problem, Spline based BEM is developed. Maniar [25] carried out a systematic research to a 3rd-order B-Spline based BEM. The accurate result is achieved with rapid convergency and C^2 continuity is guaranteed. Lee, Maniar, and Newman [26] applied this method to diverse problems.

However, B-spline (NURBS) based method is also not perfect. For complex geometry it has to split into several 'patches' and there is connection problem between patches. And also, the geometry model generated by CAD (computer aid design) has to be modified as the analytical model for CAE (computer aid engineering). To unify both procedure, IsoGeometric Approach (IGA) is proposed. The benefit includes, geometry and analysis models unified; exact geometry is used throughout and mesh repair procedures is prevented. Under this concept, the IGA-BEM is proposed and T-spline is used as the basis function. Because T-spline is a generalized NURBS, it keeps all the good features of NURBS and also offers several advantages superior to NURBS. Ginnisa, Kostasb, and Politisb [27] applied this method for ship hull optimization for minimum wave resistance. As reported, the T-spline bases offers local-refinement capabilities and achieves same error level for many fewer degrees of freedom as compared with the corresponding NURBS-based Isogeometric-BEM. Taus [28] carried out a systematic research to IGA-BEM as his doctoral dissertation.

To improve smoothness of the solution, there are several compromises between lower-order BEM and spline-based BEM. Duan [29][30][30] proposed a Taylor Expansion Boundary Element Method (TBEM). In the method, the field variable is expanded at centroid of the element with a Taylor series expansion up to 2^{nd} order. The ϕ as well as its first and second spatial derivative appearing in the expansion is solved by corresponding BIE. In their method, although geometry is approximated by flat panel, the reported results are accurate even in the sharp corner. Guiggiani [31] proposed a hypersingular boundary integral equations by directly differentiating

the boundary integral equation with respect to **x** (coordinate of field point). As a consequence the spatial derivative of ϕ is expressed by a hypersingular boundary integral equation. Frangi and Guiggiani [32] extended this method to solve 2^{nd} and 3^{rd}-order derivatives, which involves more free terms and higher singularity ($1/r^4$ and $1/r^5$). In terms of these singular integral, Gao [33][34] proposed an very accurate scheme to solve integral with kernel $1/r^n$, $n = 1 \sim 5$.

On the other hand, for improving computational efficiency, some accelerated BEMs are proposed. Two representative approaches are preFFT-BEM and Fast Multipole Method accelerated BEM. As reported, the computational effort is $O(NlogN)$ and $O(N)$, respectively, where N is the number of boundary unknowns. Harris and Dombre et al [35], investigated the efficiency of FMM-BEM in their numerical wave tank model. They suggested that for problems of moderate size, a parallelization scheme is superior to FMM acceleration. For larger problems, with around 10^5 collocation nodes, it is perhaps fastest by simply applying FMM directly at each GMRES iteration. Yan and Liu [36] also reported the efficiency of the pFFT-BEM.

1.2.4 On non-reflecting boundary condition

In time domain simulation, the computational domain have to be truncated at a distance far from the body for saving computation. An appropriate boundary condition should be imposed on this artificial boundary, which should consider the effect of the exclude domain or at least prevent wave reflecting from this boundary. The existing solutions can be categorized in several groups: (i) artificial damping approach (ii) simple far field solutions (matching scheme) (iii) differential equations matching the outer solution, e.g., modified Sommerfeld method; (iv) feedback control wave maker (generating a destructive wave).

Kim [37][38] studied the theoretical background of artificial damping aiming to optimize some parameters. Kim, Ko and Hong [39] applied five types of artificial damping scheme to fully nonlinear wave generation problem in 3D numerical wave tank. They concluded that artificial damping schemes with two damping terms in free surface conditions showed better damping performance.

However, artificial damping method is not economic for long wave (low frequency) since it requires long damping zone. Clément [40] combined artificial damping method with piston-like Neumann condition, which benefits from their different bandwidth: the numerical beach, very efficient in the high frequency range, and a piston-like Neumann condition, asymptotically ideal for low frequencies. As proved, the coupling method gives excellent results in the whole range of frequencies of interest.

Jennings, Karni and Rauch [41][42] studied the non-reflecting boundary condition of linear water waves using the analytical method, where the linear water wave equation is factored as

a product of one-way equations. However, we do not know the possibility to extend current method to nonlinear equation of water waves. Spinneken, Christou, and Swan [43] proposed a force-feedback control method for a wave maker generating destructive wave at another extremity of numerical wave tank. The strategy is that 'to destroy a wave means to create a wave', i.e., the reflecting wave is counteracted with the newly generated wave at a distance from the body. They tested this scheme in 2D numerical wave tank with success. However, to apply this method to 3D multi-directional wave is not trivial.

1.3 Outline of the dissertation

This dissertation is concerned with nonlinear wave-structure interaction with the motivation to develop a computational algorithm, which is capable of prediction of featured nonlinear phenomena. To achieve this objective, an ALE-type free surface conditions are derived with the feature that the fluid marker on free surface is able to self-adapt to body's large-amplitude motion and body's complex geometry above waterline. On the other hand, the mutual dependence of fluid/body motion is decoupled in an easy and accurate manner by solving a sets of reconstructed BVPs. Regarding solving a BVP, HOBEM with slight modification is adopted in the research, since it is an economical choice for our purpose, compared to constant panel method and spline-based BEM. In the dissertation, the computational algorithm is named as ALE-HOBEM to highlight its feature.

Chapter 1 of this dissertation describes the introduction, including the background, state-of-the-art, and objectives of the study. In **Chapter 2**, the mathematical formulations related to governing equations and boundary conditions of the problem are described. Description of the computed model is provided in **Chapter 3**. **Chapter 4** describes the application of ALE-HOBEM to nonlinear wave diffraction problem. Both numerical and experimental study are described in this chapter.

A step further, nonlinear wave radiation problem is studied in **Chapter 5**. As an attempt to study nonlinear wave interaction with a freely floating body, motion in heave mode is studied. The second-order and third-order motion resonance in heave mode is also investigated, which are described in detail in **Chapter 6**. In **Chapter 7** we list several conclusions related to our *user experience* of the ALE-HOBEM and some observations when solving the nonlinear problems.

Chapter 2

Mathematical formulation

In this chapter, the general equations governing fluids motion and body motion would be described. Two right-handed Cartesian coordinate systems are defined as shown in Fig. 2.1. One is a space-fixed coordinate system $oxyz$ with its origin on the mean free surface and z-axis being positive upwards. The other is a body-fixed coordinate system $o^b x^b y^b z^b$ with o^b placed at center of gravity of the body. When the body is at its equilibrium position, these two sets of coordinate systems are parallel. The relationship between those two coordinates can be found in many reference [6][44]. The fluid domain is enclosed by several boundaries i.e. free surface S_f, body surface S_b, control surface S_c and seabed S_h, as shown in the figure.

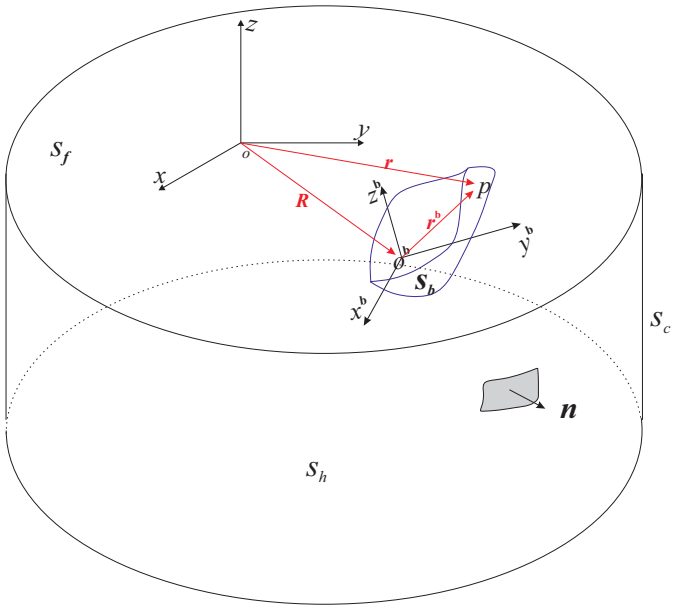

FIGURE 2.1: Sketch of coordinate systems and computation domain.

2.1 Equations of fluid motion

The fluid is assumed to be inviscid and incompressible, and the flow is irrotational. A velocity potential ϕ can therefore be introduced, which satisfies the Laplace equation in the fluid domain

$$\nabla^2\phi = 0 \tag{2.1}$$

This is also known as continuity equation, which indicates conservation of mass of the fluid.

For wave-body interaction problem, appropriate boundary conditions should be imposed on those surface according to their physical functions. A free surface requires two boundary conditions to be applied, a kinematic condition which relates the motion of free surface to the motion of fluid particle on the free surface; and a dynamic condition which connects with the force balance on the free surface. The corresponding mathematical expressions are written as follows

$$\begin{cases} \dfrac{\partial\eta}{\partial t} + \nabla\phi\cdot\nabla\eta = \dfrac{\partial\phi}{\partial z} \quad \boldsymbol{x}\in S_f \\ \dfrac{\partial\phi}{\partial t} + \dfrac{1}{2}\nabla\phi\cdot\nabla\phi + g\eta = 0 \quad \boldsymbol{x}\in S_f \end{cases} \tag{2.2}$$

where $z = \eta(x, y, t)$ denotes free surface elevation. It should be noted here that Eq.(2.2) is expressed from Euler's point of view and another alternative is Lagrange's method. The features of both methods as well as their combination would be discussed in detail in next chapter.

Because of existence of a body, the interface between fluid and body requires a non-penetrable boundary condition, which can be written as follows

$$\frac{\partial\phi}{\partial n} = \boldsymbol{V}\cdot\boldsymbol{n} \quad \boldsymbol{x}\in S_b \tag{2.3}$$

where $\boldsymbol{n} = (n_1, n_2, n_3)$ is the unit normal vector (out of the fluid) and $\boldsymbol{V}$ is the velocity of a point on body surface relative to the $Oxyz$ frame. Following the same requirement, the boundary on seabed can be written in a similar form

$$\frac{\partial\phi}{\partial n} = 0 \quad \boldsymbol{x}\in S_h \tag{2.4}$$

At far field, the asymptotic property of velocity potential requires

$$\phi \to 0 \quad \boldsymbol{x}\to\infty \tag{2.5}$$

However, in computation, the computational domain can not be infinite and thus it has to be truncated at some artificial surface e.g. S_c. And on S_c some proper boundary condition should be imposed to approximate the far field property of fluid flow described by Eq.(2.5).

On the other hand, the fully-nonlinear wave-body interaction is generally solved in a time domain with a time-stepping scheme. And thus the initial status of the fluid and body (position and velocity) should be given as the starting of the computation, which is defined as follows

$$\begin{cases} \eta(x,y,0) = f(x,y) \quad \boldsymbol{x} \in S_f \\ \phi(x,y,\eta,0) = ff(x,y,\eta) \quad \boldsymbol{x} \in S_f \\ \xi(0)_{i=1,6} = c_{i=1,6} \\ \boldsymbol{V}(x,y,z,0) = cc(x,y,z) \quad \boldsymbol{x} \in S_b \end{cases} \tag{2.6}$$

where $\xi(t)_{i=1,6}$ denotes displacement of the six degree-of-freedom (DOF) motions.

2.2 Equations of wave-body interaction

2.2.1 Hydrodynamic forces (moments) and motion equations of a body

Once the velocity potential is solved from above-mentioned equations, the pressure p can be determined following Bernoulli's Equation,

$$p = -\rho(\frac{\partial \phi}{\partial t} + \frac{1}{2}\nabla\phi \cdot \nabla\phi + gz) \tag{2.7}$$

where ρ denotes density of water and g gravitational acceleration. And the corresponding force in ith direction can be evaluated by the following expression

$$F_i = \iint_{S_b} p n_i ds \quad i = 1,6 \tag{2.8}$$

where $(n_1, n_2, n_3) = \boldsymbol{n}$ and $(n_4, n_5, n_6) = \boldsymbol{r}^b \times \boldsymbol{n}$, with r^b being the vector from the mass center to the point considered.

The body may undergo six DOF motions with three translational motions i.e. surge (ξ_1), sway (ξ_2) and heave (ξ_3), and three rotational motions i.e. roll (ξ_4), pitch (ξ_5) and yaw (ξ_6), where the translational velocities are denoted by $\boldsymbol{U} = (U_1, U_2, U_3)$ and the rotational velocities $\boldsymbol{\Omega}^b = (\Omega_1^b, \Omega_2^b, \Omega_3^b)$. Note that, the angular velocity is defined in the body-fixed coordinated system following the tradition in physics.

Following Newton's second law, the three translational motion equations can be expressed as follows

$$m\frac{dU_i}{dt} = F_i - \delta_{i3}mg \quad i = 1,3 \tag{2.9}$$

where δ_{ij} denotes Kronecker delta function and m mass of the body. Note that those motion equations are described in earth-fixed coordinate system.

The equation of rotational body motions are,

$$\frac{dH_i}{dt} = F_i \quad i = 4, 6 \tag{2.10}$$

where H_i is the angular momentum defined in earth-fixed frame with respect to center of gravity o^b. However, in the earth-fixed coordinate system, the inertia matrix of rotation is time-dependent and thus it is not convenient for computation. Alternatively, the left-hand side of Eq.(2.10) is expressed in the body-fixed coordinate system and written in the vector form,

$$\begin{cases} \boldsymbol{H} = Tr\boldsymbol{H}^b = Tr(I^b\boldsymbol{\Omega}^b) \\ \dfrac{d\boldsymbol{H}}{dt} = Tr(\dfrac{d\boldsymbol{H}^b}{dt}) = Tr[I^b\dot{\boldsymbol{\Omega}}^b + \boldsymbol{\Omega}^b \times (I^b\boldsymbol{\Omega})] \end{cases} \tag{2.11}$$

where Tr represents the transformation from $o^b x^b y^b z^b$ to $oxyz$, I^b the 3×3 inertia matrix in body-fixed frame with the property that I^b is time invariant and $\boldsymbol{H}^b$ the associated angular momentum in body-fixed frame.

Combining Eq.(2.10) and Eq.(2.11) yields

$$Tr(I^b\dot{\boldsymbol{\Omega}}^b) = \boldsymbol{M} - Tr(\boldsymbol{\Omega}^b \times (I^b\boldsymbol{\Omega}) \tag{2.12}$$

where $\boldsymbol{M}$ denotes the external moment on body with $M_{i=1,3} = F_{i=4,6}$.

2.2.2 Nonlinear coupling between fluid motion and body motion

In wave-body interaction problem, the fluid field and body motion are related by Bernoulli's equation see Eq.(2.7) and Eq.(2.8). However, to evaluate the temporal derivative of velocity potential is not straightforward, unless a backward finite-difference scheme is used, which as known is not accurate and causes instability problem. In order to solve ϕ_t ($\dfrac{\partial\phi}{\partial t}$) in an accurate manner, an appreciate boundary value problem (BVP) should be defined for ϕ_t, which is analogous to BVP of ϕ.

Comparing to ϕ, one may find that ϕ_t also satisfies Laplace equation. And recalling the dynamic free-surface condition of ϕ, one can immediately obtain the free-surface condition for ϕ_t. However, the body boundary condition for ϕ_t is not apparent. We would derive body boundary condition of ϕ_t starting from Eq.(2.3). Specifically, body boundary condition for ϕ can be rewritten as follows

$$\nabla\phi \cdot \boldsymbol{n} = (\boldsymbol{U} + \boldsymbol{\Omega^b} \times \boldsymbol{r^b}) \cdot \boldsymbol{n} \quad \boldsymbol{x} \in S_b \tag{2.13}$$

Following a point p on body surface, where p adheres to body surface without relative motion, see Fig. 2.2, the following expressions hold due to the fact that p only follows a rigid body motion.

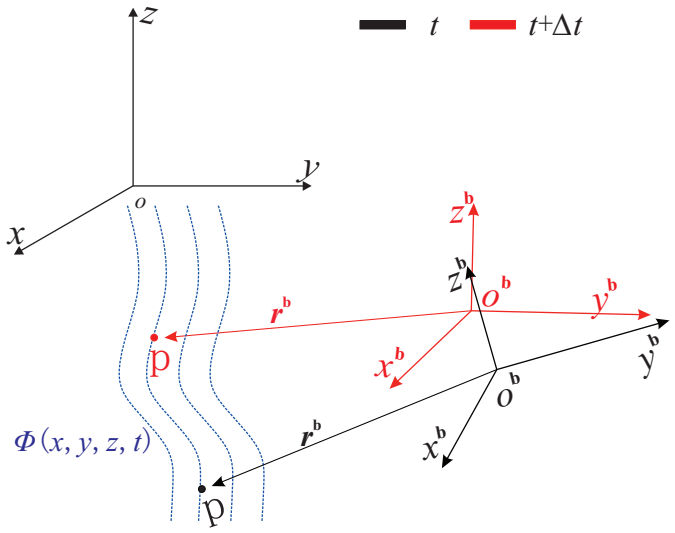

FIGURE 2.2: Time derivative when following a fixed point p on body surface.

$$\begin{cases} \boldsymbol{x}_p = \boldsymbol{oo^b} + \boldsymbol{r^b} \\ \boldsymbol{V}_p = \dfrac{d\boldsymbol{oo}^b}{dt} + \dfrac{d\boldsymbol{r}^b}{dt} = \boldsymbol{U} + \boldsymbol{\Omega}^b \times \boldsymbol{r}^b \end{cases} \tag{2.14}$$

If p moves in a field, for instance $\phi(x, y, z, t)$, the material derivative can be defined as follows

$$\frac{d\phi}{dt} = \frac{\partial \phi}{\partial t} + (\boldsymbol{V}_p \cdot \nabla) \cdot \nabla \phi \tag{2.15}$$

With those information in mind, taking time derivative in left-hand side of Eq.(2.13), yields

$$\frac{d}{dt}(\nabla\phi \cdot \boldsymbol{n}) = \frac{d}{dt}(\nabla\phi) \cdot \boldsymbol{n} + \nabla\phi \cdot \frac{d\boldsymbol{n}}{dt} \tag{2.16}$$

It is easy to derive the following expression according to Eq.(2.14) and Eq.(2.15).

$$\begin{cases} \dfrac{d}{dt}(\nabla\phi) = \nabla\phi_t + [(\boldsymbol{U} + \boldsymbol{\Omega}^b \times \boldsymbol{r}^b) \cdot \nabla]\nabla\phi \\ \dfrac{d\boldsymbol{n}}{dt} = \boldsymbol{\Omega}^b \times \boldsymbol{n} \end{cases} \tag{2.17}$$

Substituting Eq.(2.17) into Eq.(2.16) yields

$$\begin{aligned} \frac{d}{dt}(\nabla\phi \cdot \boldsymbol{n}) &= \nabla\phi_t \cdot \boldsymbol{n} + \{[(\boldsymbol{U} + \boldsymbol{\Omega}^b \times \boldsymbol{r}^b) \cdot \nabla]\nabla\phi\} \cdot \boldsymbol{n} + \nabla\phi \cdot (\boldsymbol{\Omega}^b \times \boldsymbol{n}) \\ &= \frac{\partial}{\partial n}(\phi_t) + (\boldsymbol{U} + \boldsymbol{\Omega}^b \times \boldsymbol{r}^b) \cdot \frac{\partial \nabla\phi}{\partial n} + \nabla\phi \cdot (\boldsymbol{\Omega}^b \times \boldsymbol{n}) \\ &= \frac{\partial}{\partial n}(\phi_t) + \boldsymbol{U} \cdot \frac{\partial \nabla\phi}{\partial n} + \boldsymbol{\Omega}^b \cdot \frac{\partial}{\partial n}(\boldsymbol{r}^b \times \nabla\phi) \end{aligned} \tag{2.18}$$

The last equation holds using the identity $\dfrac{\partial r^b}{\partial n} = \boldsymbol{n}$.

Taking time derivative in right-hand side of Eq.(2.13), yields

$$\begin{aligned}\frac{d}{dt}[(\boldsymbol{U} + \boldsymbol{\Omega^b} \times \boldsymbol{r^b}) \cdot \boldsymbol{n}] &= [\dot{\boldsymbol{U}} + \dot{\boldsymbol{\Omega}}^b \times \boldsymbol{r}^b + \boldsymbol{\Omega}^b \times (\boldsymbol{\Omega}^b \times \boldsymbol{r}^b)] \cdot \boldsymbol{n} \\ &+ (\boldsymbol{U} + \boldsymbol{r^b} \times \boldsymbol{\Omega^b}) \cdot (\boldsymbol{\Omega}^b \times \boldsymbol{n}) \\ &= (\dot{\boldsymbol{U}} + \dot{\boldsymbol{\Omega}}^b \times \boldsymbol{r}^b) \cdot \boldsymbol{n} + \boldsymbol{\Omega}^b \cdot (\boldsymbol{n} \times \boldsymbol{U})\end{aligned} \tag{2.19}$$

Combining Eq.(2.18) and Eq.(2.19) gives

$$\nabla\phi_t \cdot \boldsymbol{n} = (\dot{\boldsymbol{U}} + \dot{\boldsymbol{\Omega}}^b \times \boldsymbol{r}^b) \cdot \boldsymbol{n} - \boldsymbol{U} \cdot \frac{\partial \nabla\phi}{\partial n} + \boldsymbol{\Omega}^b \cdot \frac{\partial}{\partial n}[\boldsymbol{r}^b \times (\boldsymbol{U} - \boldsymbol{\nabla\phi})] \tag{2.20}$$

This is the body boundary condition of ϕ_t, which indicates the normal acceleration of a fluid particle on body surface is identical with body's normal acceleration at the same point.

To sum up, the governing equations as well as boundary conditions of ϕ_t can be written as follows

$$\begin{cases} \nabla^2\phi_t = 0 \\ \dfrac{\partial\phi}{\partial t} = -\dfrac{1}{2}(\nabla\phi)^2 - gz \quad \boldsymbol{x} \in S_f \\ \dfrac{\partial\phi_t}{\partial n} = (\dot{\boldsymbol{U}} + \dot{\boldsymbol{\Omega}}^b \times \boldsymbol{r}^b) \cdot \boldsymbol{n} - \boldsymbol{U} \cdot \dfrac{\partial \nabla\phi}{\partial n} + \boldsymbol{\Omega}^b \cdot \dfrac{\partial}{\partial n}[\boldsymbol{r}^b \times (\boldsymbol{U} - \boldsymbol{\nabla\phi})] \quad \boldsymbol{x} \in S_b \end{cases} \tag{2.21}$$

Since ϕ_t is relevant to pressure distribution, see Bernoulli's equation Eq.(2.7), the terms containing body's acceleration in Eq.(2.21) indicates a mutual dependence of fluid/structure motions. And therefore additional effort should be focused on this issue when developing a numerical scheme. The above-mentioned procedures for deriving a BVP for ϕ_t can also be found in Wu[45].

Chapter 3

Numerical implementations

In order to have a global view of the wave-body interaction problem, a brief computational flow used for design of numerical scheme is illustrated in Fig.3.1. And following this sketch, the

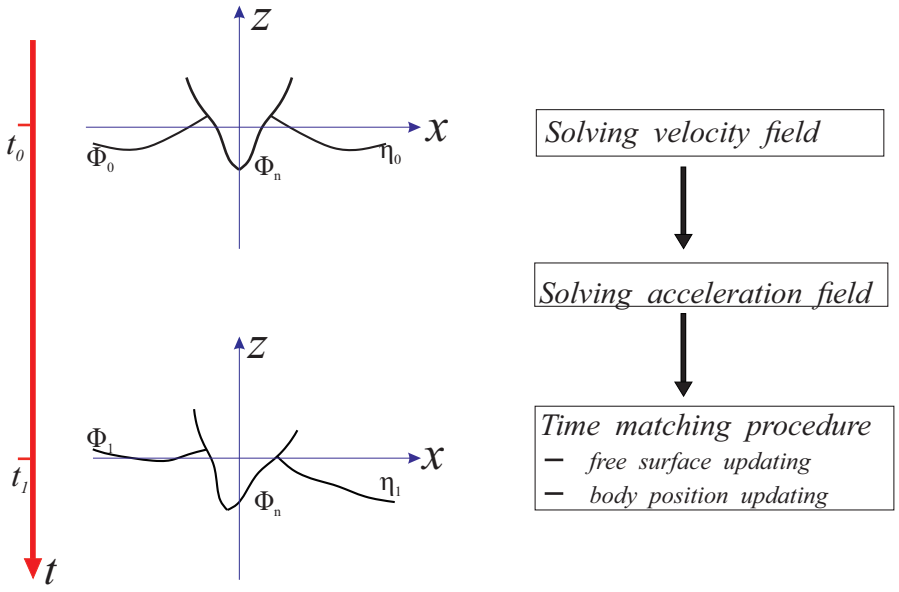

FIGURE 3.1: Sketch of computational flow.

wave-body interaction problem can be divided into parts, i.e. subproblems:

- To develop a boundary value problem solver for the purpose of solving velocity field.
- To develop a scheme in order to decouple the mutual dependence of fluid/structure motions.
- To develop a scheme for updating free surface as well as the field value defined on the free surface.

Those three subproblems would be described in detail in this chapter.

3.1 Schemes for free surface updating

As described in Chapter 2, the free-surface is expressed in a Eulerian form,

$$\begin{cases} \dfrac{\partial \eta}{\partial t} + \nabla\phi \cdot \nabla\eta = \dfrac{\partial \phi}{\partial z} \quad \boldsymbol{x} \in S_f \\ \dfrac{\partial \phi}{\partial t} + \dfrac{1}{2}\nabla\phi \cdot \nabla\phi + g\eta = 0 \quad \boldsymbol{x} \in S_f \end{cases} \tag{3.1}$$

However, this type of free surface conditions is not suitable for design a numerical scheme and some modifications should be made.

In the framework of potential flow theory, especially when the fluid field is solved by a BEM method, a free surface tracking scheme (e.g. MEL and SL scheme) is more straightforward than surface capture scheme (e.g. VOF method). In free surface tracking scheme, the free surface is represented by a bunch of fluid particles or infinitesimal probes on free surface, where their motion denotes free surface deformation. By following these fluid markers (fluid particles or infinitesimal probes), the evolution of free surface as well as other variable defined on it can be determined using a typical time-steeping scheme. With different definitions of fluid markers, Eq.(3.1) can be modified into several equivalent forms, which is suitable for design of numerical scheme.

3.1.1 Lagrangian method

In this method, the free surface is represented by a group of *real* fluid particles. Moving with these particles, the time variation of some values in the fluid field can be determined by a material derivative

$$\frac{D}{Dt} = \frac{\partial}{\partial t} + \nabla\phi \cdot \nabla \tag{3.2}$$

where $\nabla\phi$ is identical to velocity of fluid particle. From viewpoint of Lagrangian method, the associated free-surface conditions can be rewritten as follows

$$\begin{cases} \dfrac{D\boldsymbol{X}}{Dt} = \nabla\phi \quad \boldsymbol{x} \in S_f \\ \dfrac{D\phi}{Dt} = \dfrac{1}{2}\nabla\phi \cdot \nabla\phi - g\eta \quad \boldsymbol{x} \in S_f \end{cases} \tag{3.3}$$

where $\boldsymbol{X}(t)$ is position vector of a fluid particle at time t. Since the free surface is described in a Lagrangian form while the field equation (Laplace equation) is solved in a Eulerian manner, this scheme as a whole is referred to as mixed-Eulerian-Lagrangian scheme[1]. Due to flexibility of particle motion, this scheme could handle complex deformation of free surface e.g. overturning wave. The idea of this scheme is sketched in left-hand side of Fig.3.2.

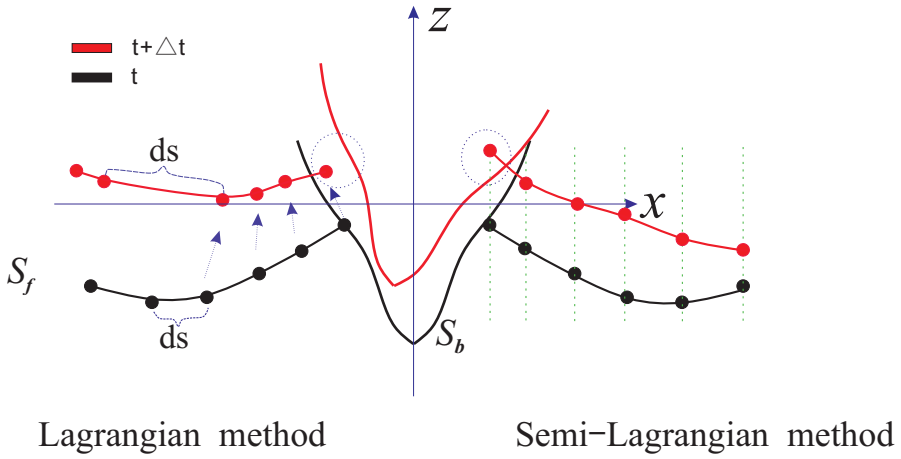

FIGURE 3.2: Illustration of different schemes.

3.1.2 Semi-Lagrangian method

In the semi-lagrangian (SL) scheme, the free surface is represented by a group of infinitesimal probes floating on free surface. In contrast to the MEL scheme where the fluid particle moves freely following deformation of free surface, in the SL scheme, the horizontal motion of fluid marker (probe) is fixed and the marker only moves vertically following the free surface as shown in right-hand side of Fig.3.2. In such case, the associated free-surface conditions can be written as follows

$$\begin{cases} \dfrac{\delta\eta}{\delta t} = \dfrac{\partial\phi}{\partial z} - \nabla\phi\cdot\nabla\eta \quad \boldsymbol{x}\in S_f \\ \dfrac{\delta\phi}{\delta t} = -\dfrac{1}{2}\nabla\phi\cdot\nabla\phi - g\eta + \dfrac{\delta\eta}{\delta t}\cdot\nabla\phi \quad \boldsymbol{x}\in S_f \end{cases} \tag{3.4}$$

where $\dfrac{\delta}{\delta t} = \dfrac{\partial}{\partial t} + \dfrac{\partial\eta}{\partial t}\cdot\nabla$ denotes material derivative by following the fluid marker. Note that $\dfrac{\delta\eta}{\delta t} = \dfrac{\partial\eta}{\partial t}$ denotes vertical velocity of fluid marker. Since the horizontal motion of fluid marker is prescribed, it is relatively easy to manage mesh on free surface compared to MEL scheme.

3.1.3 Remakes on both methods

Both methods are firstly proposed for simulating evolution of nonlinear water waves without existence of a floating body. When applied to nonlinear wave-body interaction problem, some modifications towards the original schemes should be made in order to solve some featured problems. The following two conditions should be considered, when a floating body is involved : (1) the intersection should be captured and updated exactly; (2) the mesh on the free surface should be self-adapted in order to conform to the body motion or complex geometry above the still waterline. With those requirements in mind, the MEL and SL scheme are re-examined.

The MEL scheme as described above is extensively used in the literature due to several advantages, such as easy implementation and capability of dealing with overturning waves. However, due to the nature of this scheme that fluid particle moves with much freedom, the unwanted motion of fluid particle may cause some problems, see left-hand side of Fig.3.2. And thus some modifications should be made, when applying to wave-body interaction problems. In order to meet condition (1) mentioned above, Shirakura and Tanizawa [20] and Liu, Xue and Yue [5] derived an ALE-type formulation for updating the intersection point. For avoiding a situation that the distance between two neighboring fluid particles becomes too close or too far, a regridding scheme is applied frequently, which is related to condition (2). However, the regridding scheme as an artificial procedure would cause lose of information of fluid flow.

Alternatively, the SL scheme [2] is also widely used in wave-body interaction problems. Compared to MEL scheme, the regridding scheme is circumvented in SL scheme due to the fact that the horizontal distance between two neighbouring markers is time-inerrant (condition (2)). However a drawback of this scheme is that it is applicable only to cases when the body surface is vertical near the waterline (condition (1)).

Comparative study of different schemes for tracking the free surface may be summarized as follows. The excessive freedom of Lagrangian fluid particle makes the MEL scheme capable to handle complex deformation of the free surface, but the fluid particle must be relocated frequently to dismiss unwanted motion of the particle. On the other hand, relocation of the fluid marker is avoided in the SL scheme by restricting the horizontal motion of the fluid marker at the sacrifice of flexibility to treat a body with large flare.

3.1.4 Arbitrary Lagrangian-Eulerian scheme

After the review described above, a logical question arises. Is there an optimized compromise between MEL and SL schemes, where advantages of both methods are reserved while disadvantages are minimized? The answer is positive. The starting point for realizing this optimized compromise is to increase flexibility of the SL scheme. In order to take into account a complex body geometry above the waterline, a curved path analogous to the body's local geometry is introduced for each fluid marker on the free surface, where the movement of the marker along this path represents the free surface deformation. On the other hand, in order to adapt to a large-amplitude motion of the body, the prescribed path may also translate and/or rotate in connection with the body motion. The idea of this method is illustrated in Fig.3.3. By carefully designing these parameters, i.e. the shape, motion, and arrangement of these paths, the mesh on the free surface can be well controlled. Detailed discussion on this method would be introduced later. Since the inherent idea of this method is taken from the ALE scheme [46], this scheme will be referred to as the ALE scheme hereafter.

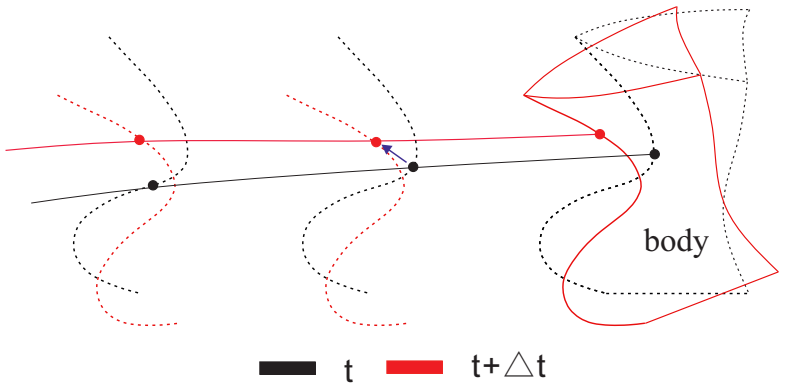

FIGURE 3.3: Illustration of ALE scheme.

3.1.4.1 Derivation of ALE scheme, (body fixed)

To demonstrate the ALE procedure, we take updating of intersection point p illustrated in Fig. 3.4 as an example to show the central idea. And extending this approach to update the remaining fluid markers on free surface is straightforward. In the following contents we first apply ALE to cases where the tangential vector on cross section of body surface is constant i.e. inclined flare without curvature, see case (a) in Fig.3.4 and extend the approach to general cases where body geometry can be arbitrary, for instance, case (b) in Fig.3.4.

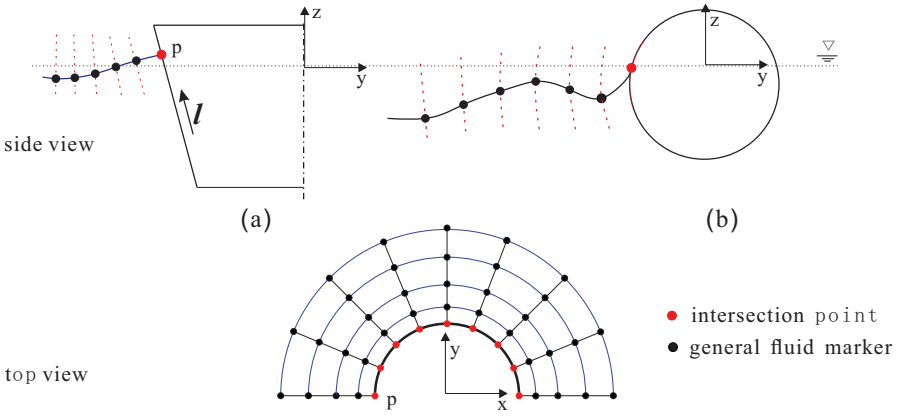

FIGURE 3.4: Sketch of computational domain (half), side and top view. (a) an axisymmetrical body with inclined flare; (b) a sphere with curved flare.

As far as intersection point p is concerned, physically it always stays on both body surface and free surface. And the corresponding mathematical constraint conditions are: (i) the velocity of p must parallel with tangential vector $\boldsymbol{l}$ on body surface; (ii) the motion of p must satisfy kinematic condition on free surface.

According to condition (i), velocity of p should parallel with $\boldsymbol{l}$.

$$\boldsymbol{V_p} = (\frac{dx}{dt}, \frac{dy}{dt}, \frac{dz}{dt}) = \kappa \boldsymbol{l} = \kappa(l_x, l_y, l_z) \tag{3.5}$$

where $\boldsymbol{V_p}$ is the velocity of p and κ is a scalar. Following condition (ii), fluid marker on intersection should also meet kinematic free surface condition,

$$\frac{\delta\eta}{\delta t} = \frac{\partial\eta}{\partial t} + \boldsymbol{V_p}\cdot\nabla\eta = \frac{\partial\phi}{\partial z} + \boldsymbol{V_p}\cdot\nabla\eta - \nabla\phi\cdot\nabla\eta \tag{3.6}$$

where $\frac{\delta}{\delta t} = \frac{\partial}{\partial t} + \boldsymbol{V_p}\cdot\nabla$ is material derivative by following fluid marker p. Note that $\frac{\delta\eta}{\delta t} = \frac{dz}{dt}$ according to the definition of η, and substituting this relation into Eq.(3.6) yields

$$\kappa l_z = \frac{\partial\phi}{\partial z} + \kappa(l_x\eta_x + l_y\eta_y) - (\phi_x\eta_x + \phi_y\eta_y) \tag{3.7}$$

and the corresponding vector form is

$$\kappa\boldsymbol{l}\cdot\nabla(z-\eta) = \nabla\phi\cdot\nabla(z-\eta) \tag{3.8}$$

note that the unit normal vector on free surface is $\boldsymbol{n} = \nabla(z-\eta)/\mid\nabla(z-\eta)\mid$ and the final expression is

$$\kappa = \frac{\phi_n}{l_n} \tag{3.9}$$

A step forward, $\boldsymbol{V_p}$ can be expressed as

$$\boldsymbol{V_p} = (\frac{dx}{dt}, \frac{dy}{dt}, \frac{dz}{dt}) = \frac{\phi_n}{l_n}\boldsymbol{l} \tag{3.10}$$

This expression indicates as long as intersection p moves according to this formulation, p always stay on body surface and free surface. It is apparent that this expression can be used for time stepping of new position of p in next step.

Correspondingly, substituting $\boldsymbol{V_p}$ into dynamic free surface condition yields

$$\frac{\delta\phi}{\delta t} = \frac{\partial\phi}{\partial t} + \boldsymbol{V_p}\cdot\nabla\phi = -g\eta - \frac{1}{2}(\nabla\phi)^2 + \frac{\phi_n}{l_n}\boldsymbol{l}\cdot\nabla\phi \tag{3.11}$$

and thus new ϕ at next time step can be obtained by time integration of this expression. Note that if we take $\boldsymbol{l} = (0,0,1)$ that indicates the body has wall-sided geometry near waterline, Eq.(3.10) and Eq.(3.11) can be reduced to Eq.(3.4), which is the frequently used semi-lagrangian approach with a restriction that the body must be wall-sided around waterline. Shirakura and Tanizawa[20] and Liu, Xue and Yue [5] also used this method to update intersection while MEL is used for updating free surface.

Following the similar idea which is proposed in above contents, we apply the ALE approach to more general case where the body has curved flare near waterline, which indicates the tangential vector on cross section line of the body is no longer a constant, see case (b) in Fig.3.4. Instead

of using Cartesian coordinate system, a parametric coordinate system is used along the cross section line of the body. For arbitrary 3D curve its parametric expression is

$$\boldsymbol{X} = \boldsymbol{X}(u) \tag{3.12}$$

where $\boldsymbol{X} = (x, y, z)$ is coordinate of a point on cross section line of the body and u is a parameter. In the present study u denotes arc-length of this 3D curve and the curve is approximated by a cubic spline. Suppose the motion of intersection p on this curve is

$$u = u(t) \tag{3.13}$$

The corresponding velocity of p is

$$\boldsymbol{V}_p = \frac{du}{dt}\boldsymbol{l} = (x_u, y_u, z_u)\frac{du}{dt} \tag{3.14}$$

where $\boldsymbol{l}(u)$ is unit tangential vector at $\boldsymbol{X}(u)$. Note that $\boldsymbol{l}(u) = (x_u, y_u, z_u)$ under the condition that u denotes arc-length.

Substituting Eq.(3.14) to kinematic free surface condition and following similar procedure mentioned above yields

$$\frac{du}{dt} = (\frac{\partial \phi}{\partial z} - \nabla\phi \cdot \nabla\eta)/(z_u - x_u\eta_x - y_u\eta_y) \tag{3.15}$$

Because of the relationship of u and $\boldsymbol{X}$, see Eq.(3.12), once u is determined the corresponding $\boldsymbol{X}$ can also be determined. And thus this expression can be further used for time stepping new position of intersection point p at next time step. Recalling the definition of unit normal vector on free surface, the above equation can be finally written as

$$\frac{du}{dt} = \frac{\phi_n}{l_n} \tag{3.16}$$

this expression is elegant and consistent with Eq.(3.9). The only difference compared with Eq.(3.9) is that $\boldsymbol{l}(u)$ is no longer a constant.

A step forward, substituting $\boldsymbol{V}_p = \frac{\phi_n}{l_n}\boldsymbol{l}$ into dynamic free surface condition, yields

$$\frac{\delta\phi}{\delta t} = -g\eta - \frac{1}{2}(\nabla\phi)^2 + \boldsymbol{l} \cdot \nabla\phi\frac{du}{dt} \tag{3.17}$$

And Eq.(3.17) can be used for time steeping new ϕ at new intersection point p.

Thus far, we have derived expressions for time stepping the position of intersection point as well as velocity potential on the intersection. Eq.(3.10) and Eq.(3.11) can be applied to body with inclined flare (without curvature) around still waterline. And Eq.(3.16) together with Eq.(3.17)

can be applied to more general cases where the body has curved flare around still waterline. For the remaining fluid marker on the free surface, this approach can be easily extended by introducing a path with tangential vector $\tilde{l}$, see dotted line in Fig.3.4. For easy implementation, it need not to define specific path for each maker. In present study, we group the markers who belonging to same cross section of the computational domain, see Fig.3.4, and for markers in the same group the path can be simply generated by translation of the cross section line of the body.

3.1.4.2 Derivation of ALE scheme, (body in motion)

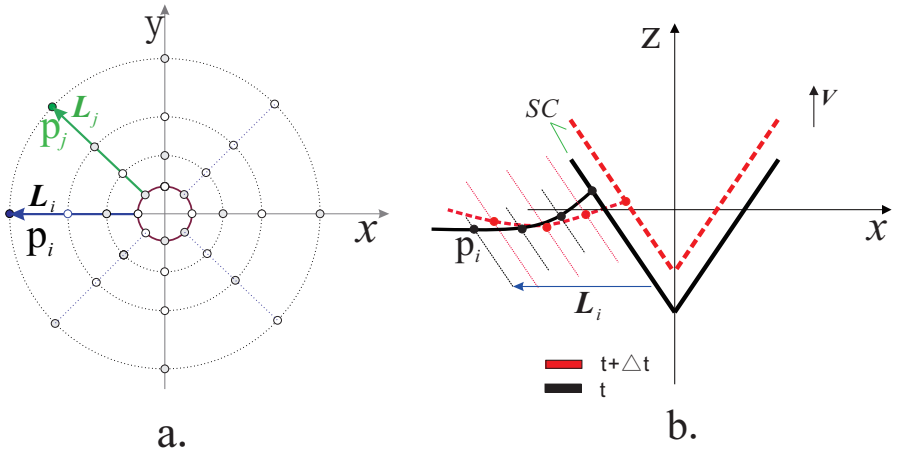

FIGURE 3.5: Illustration of ALE scheme, where radiated waves is generated by a heaving circular cone. a. top view of initial mesh of free surface; b. side view of computation domain.

As explained above, the feature of ALE scheme is to introduce a prescribed path for each node on free surface. When body is in motion, the complexity of the problem is increased compared to the above-mentioned procedure. For completeness, we list below all the associated problems, even though some of them has been described in previous subsection,

(i) how to design an appropriate path for each fluid marker;

(ii) how to collocate all of those pathes in space, which at least the path should not intersect with each other;

(iii) how to optimize the motion (translation and/or rotation) of each path in order to adapt to large-amplitude motion of the body.

In terms of problem (i), in the present research, the path is generated by translation of sectional line on the body, see Fig.3.5. More specifically, the path of point p_i, for instance, illustrated in Fig.3.5 is generated by translation of body's sectional line (SC) along a stationary vector (in

most cases) $\boldsymbol{L}_i$. And how to determine vector $\boldsymbol{L}_i$ would be discussed later. This strategy enable us to only define and store very few curves as pathes for all of fluid markers.

Because the prescribed path serves as trajectory of fluid marker, too close or too far distance of two pathes is directly affect the quality of free surface mesh. This problem related to problem (ii) can be resolved at the initial stage, where free surface is discretized by a fine mesh at the beginning as we can see in Fig.3.5 a. At this stage, each fluid marker is provided with a unique vector e.g. $\boldsymbol{L}_i$ of p_i, which indicates the path of p_i would always keep its distance and orientation from the body surface. By this way, the relative position of neighbouring fluid markers is locked and thus the aspect ratio of each element on free surface is time-invariant. This strategy retains good topology of initial mesh throughout the long-time simulation.

Regarding problem (iii), as we can see in Fig.3.5 b, the body's motion may cause increase of projected free surface area on horizontal plane, and the mesh near this region would be stretched if there is no proper adjustment. In order to make the mesh self-adjust associated with body's motion, in the ALE scheme all the paths are defined to move with the body's sectional line which the path is translated from. By doing so, mesh near waterline can be self-adjust when body is in large-amplitude motion. What's more, since all nodes on free surface move uniformly following the body's motion, this strategy enables us to simulate motions with large horizontal displacement by limited computational domain and mesh, for instance, ship's maneuvering test.

Taking into account those considerations mentioned above, in the ALE scheme, the position of prescribed path and body's sectional line can be related by following relations,

$$\begin{cases} \boldsymbol{x}_p = \boldsymbol{x}_{p'} + \boldsymbol{L}_p \\ \dot{\boldsymbol{x}}_p = \dot{\boldsymbol{x}}_{p'} + \dot{\boldsymbol{L}}_p \end{cases} \tag{3.18}$$

where $\boldsymbol{x}_p$ is arbitrary point on the prescribed path and $\boldsymbol{x}_{p'}$ the corresponding point on body's sectional line, where $\boldsymbol{x}_p$ and $\boldsymbol{x}_{p'}$ is coincident once the prescribed path is translated back towards $-\boldsymbol{L}_p$. Note that if there is no yaw motion, $\dot{\boldsymbol{L}}_p = 0$, otherwise $\boldsymbol{L}_p$ would also rotate about z axis. Fig. 3.6 illustrates this mapping between p and p'.

Once solving above mentioned problem, the subsequent problem is how to determine the new position of a fluid marker moving along a curve which is also in motion. Under this circumstance, two constraint conditions should be imposed on the motion of fluid marker; (a) velocity of the marker $\boldsymbol{V}_p$ should parallel with tangential vector of the path, see Fig. 3.6; (b) $\boldsymbol{V}_p$ should also subject to kinematic boundary condition of free surface. According to condition (a), $\boldsymbol{V}_p$ can be expressed as follows:

$$\boldsymbol{V}_p = \chi \boldsymbol{l} + \boldsymbol{V} \tag{3.19}$$

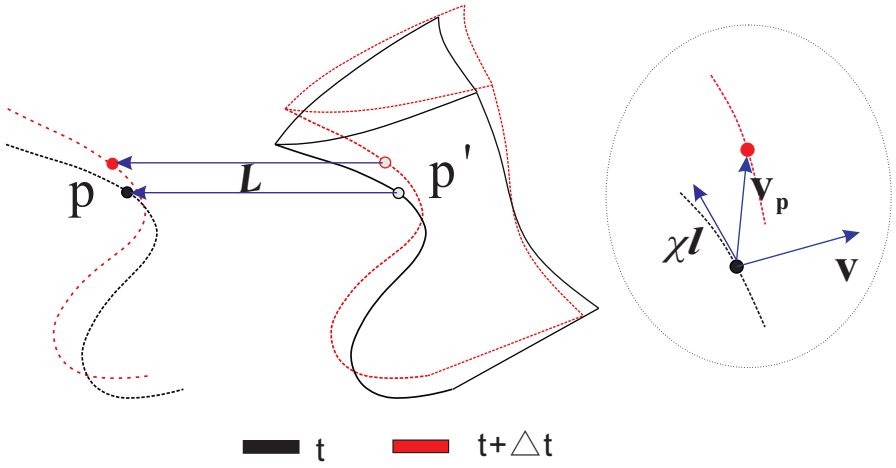

FIGURE 3.6: The mapping between prescribed path and body's sectional line.

where $\boldsymbol{l}$ is tangential vector of prescribed path at point P, χ a scalar and $\boldsymbol{V}$ the velocity at point P due to motion of path itself. Note that the path is approximated by Cubic-Spline and $\boldsymbol{l}$ can be evaluated numerically for arbitrary body geometry.

Substitution of Eq. (3.19) into the kinematic boundary condition of the free surface and rather lengthy transformation yields,

$$\chi = \frac{\nabla\phi \cdot \nabla(z-\eta) - \boldsymbol{V} \cdot \nabla(z-\eta) - \mu\eta}{\nabla(z-\eta) \cdot \boldsymbol{l}} \tag{3.20}$$

Note that the derivation procedure is similar with the cases that the body is fixed.

Substituting Eqs. (3.19) and (3.20) into the dynamic free-surface condition, we have

$$\frac{\delta\phi}{\delta t} = -g\eta - \frac{1}{2}(\nabla\phi)^2 + \boldsymbol{V}_p \cdot \nabla\phi - \mu\phi \tag{3.21}$$

where $\dfrac{\delta}{\delta t} = \dfrac{\partial}{\partial t} + \boldsymbol{V_p} \cdot \nabla$ denotes the material derivative, following a marker on a moving path.

Equations (3.19), (3.20) and (3.21) provide the ALE-type free-surface conditions and can be further used for time stepping. Compared to MEL and SL scheme, these free-surface conditions contain terms of $\boldsymbol{V}$ and $\boldsymbol{l}$, which indicates both body's motion and geometry of body are taken into account in the proposed ALE scheme.

As an optimized compromise between MEL and SL, the advantages of this ALE approach are highlighted here. Firstly, the curved path which fits closely with body's local geometry enables self-awareness of fluid marker on geometry above waterline. And the motion of the path as a response to body's large-amplitude oscillation enables self-adjustment of the mesh, which is crucial for long-time simulation. Secondly, once the path of fluid marker is determined at the pre-processing, the trajectory of the marker can be computed during the entire computation. In

other words, the mesh on the free surface needs to be generated only once at the beginning, and the mesh can be generated *automatically* in subsequent time without relocation of the fluid markers. In addition, this approach is very efficient in implementation, since we need only to restore N 3D curves represented by the cubic spline for general cases that a body has complex geometry, where N is the number of nodes along the waterline.

As mentioned before, Zhang [12] also developed a modified SL (MSL) scheme when studying sloshing in a non-wall-sided tank. However, the basis for deriving both schemes is different. In MSL scheme a coordinate transform is adopted and such that the new z' axis is set to be paralleled with the inclined wall, and thus the fluid marker only moves '*vertically*' in z' direction as the original SL scheme. In the present derivation, a material derivative is used with very clear physical meaning. What's more, because the prescribed path is represented by a parametric curve in the present research, the intersection can be updated exactly with very complex body geometry. However, it seems that the MSL scheme is only applicable to very simple cases, where the flare is inclined, i.e. the tangential vector of the flare is constant.

3.2 Evaluation of ϕ_t

In order to obtain hydrodynamic forces (moments) $\boldsymbol{F}$ exerting on the body, one need firstly consider solution of $\partial\phi/\partial t$ appearing in Bernoulli's equation. Although, an exact BVP of ϕ_t is established in Eq.(2.21), for convenience, Eq.(2.21) is repeated here

$$\begin{cases} \nabla^2\phi_t = 0 \\ \dfrac{\partial\phi}{\partial t} = -\dfrac{1}{2}(\nabla\phi)^2 - gz \quad \boldsymbol{x} \in S_f \\ \dfrac{\partial\phi_t}{\partial n} = (\dot{\boldsymbol{U}} + \dot{\boldsymbol{\Omega}}^b \times \boldsymbol{r}^b)\cdot\boldsymbol{n} - \boldsymbol{U}\cdot\dfrac{\partial\nabla\phi}{\partial n} + \boldsymbol{\Omega}^b\cdot\dfrac{\partial}{\partial n}[\boldsymbol{r}^b \times (\boldsymbol{U} - \boldsymbol{\nabla\phi})] \quad \boldsymbol{x} \in S_b \end{cases} \tag{3.22}$$

There are still problems to evaluate ϕ_t in solving this BVP. On one hand, ϕ_t is fully coupled with body's accelerations, that is to evaluate ϕ_t, we need information of body's accelerations, while to evaluate body's accelerations we need first to calculate ϕ_t. On the other hand, as we can see, there are second derivative terms e.g. $\boldsymbol{U}\cdot\partial\nabla\phi/\partial n$ appearing in the body boundary condition. Directly evaluating this term requires much effort in a 3D problem, see Berkvens[19] and Shirakura and Tanizawa[20].

In order to decouple the problem, the component of hydrodynamic force, which is proportional to body's acceleration, is extracted from the total force. And thus ϕ_t is decomposed into two parts

$$\phi_t = \psi_{acc} + \psi_{oth} \tag{3.23}$$

where ψ_{acc} is the induced potential due to acceleration and ψ_{oth} is the other remaining part. Those two are subject to the following BVPs, respectively,

$$\begin{cases} \nabla^2 \psi_{acc} = 0 \\ \psi_{acc} = 0 \quad S_f \\ \dfrac{\partial \psi_{acc}}{\partial n} = (\dot{\boldsymbol{U}} + \dot{\boldsymbol{\Omega}}^b \times \boldsymbol{r}^b) \cdot \boldsymbol{n} \quad S_b \end{cases} \tag{3.24}$$

$$\begin{cases} \nabla^2 \psi_{oth} = 0 \\ \psi_{oth} = -\dfrac{1}{2}(\nabla\phi)^2 - gz \quad S_f \\ \dfrac{\partial \psi_{oth}}{\partial n} = -\boldsymbol{U} \cdot \dfrac{\partial \nabla\phi}{\partial n} + \boldsymbol{\Omega}^b \cdot \dfrac{\partial}{\partial n}[\boldsymbol{r}^b \times (\boldsymbol{U} - \nabla\phi)] \quad S_b \end{cases} \tag{3.25}$$

Suppose ψ_{acc} is linearly dependent on body's acceleration,

$$\begin{aligned} \psi_{acc} =& \dot{U}_1\varphi_1 + \dot{U}_2\varphi_2 + \dot{U}_3\varphi_3 \\ &+ \dot{U}_4\varphi_4 + \dot{U}_5\varphi_5 + \dot{U}_6\varphi_6 \end{aligned} \tag{3.26}$$

where $(U_1, U_2, U_3) = \boldsymbol{U}$ and $(U_4, U_5, U_6) = \boldsymbol{\Omega^b}$. Substituting this expression into Eq.(3.24) yields

$$\begin{cases} \nabla^2 \varphi_i = 0 \\ \varphi_i = 0 \quad \textit{on free surface} \\ \dfrac{\partial \varphi_i}{\partial n} = n_i \quad \textit{on body surface} \end{cases} \tag{3.27}$$

where $(n_1, n_2, n_3) = \boldsymbol{n}$ and $(n_4, n_5, n_6) = \boldsymbol{r}^b \times \boldsymbol{n}$. And thus the hydrodynamic force proportional to body's acceleration can be written as follows

$$F_i^{acc} = -\rho \dot{U}_i \iint \varphi_i n_i ds \tag{3.28}$$

and therefore $a_i = -\rho \iint \varphi_i n_i ds$ serves as added mass and can be evaluated simultaneously. After the derivation, one may suspect why Eq.(3.24), Eq.(3.26), Eq.(3.27) and Eq.(3.28) governs force related to body's acceleration. In appendix, an alternative method is proposed, where an identical expression is derived from a physical point of view.

In terms of ψ_{oth}, to avoid evaluating second derivatives, an auxiliary function is introduced as follows,

$$\psi'_{oth} = \psi_{oth} + \boldsymbol{U} \cdot \nabla\phi - \boldsymbol{\Omega}^b \cdot [\boldsymbol{r}^b \times (\boldsymbol{U} - \nabla\phi)] \tag{3.29}$$

Rewriting Eq.(3.25) yields

$$\begin{cases} \nabla^2 \psi'_{oth} = 0 \\ \psi'_{oth} = -\frac{1}{2}(\nabla\phi)^2 - gz + \boldsymbol{U}\cdot\nabla\phi - \boldsymbol{\Omega}^b \cdot [\boldsymbol{r}^b \times (\boldsymbol{U} - \nabla\phi)] \quad S_f \\ \frac{\partial \psi'_{oth}}{\partial n} = 0 \quad S_b \end{cases} \tag{3.30}$$

In comparison to Eq(3.25), there is no need to evaluate second derivative in Eq(3.30). And thus the corresponding force can be written as follows

$$F_i^{oth} = -\rho \iint (\psi'_{oth} - \boldsymbol{U}\cdot\nabla\phi + \boldsymbol{\Omega}^b \cdot [\boldsymbol{r}^b \times (\boldsymbol{U} - \nabla\phi)]) n_i ds \tag{3.31}$$

According to Bernoulli's equation, the force exerting on the body can be expressed as follows

$$F_i = F_i^{acc} + F_i^{oth} - \rho \iint (\frac{1}{2}(\nabla\phi)^2 + gz) n_i ds \tag{3.32}$$

To achieve above derivations, Wu's work [21] is followed and it is extended in the present research to 6-DOF motion. Zhang [12] also use the similar procedure to calculate hydrodynamic force in sloshing problem.

3.2.1 Other methods for evaluating ϕ_t

In some cases, where the hydrodynamic forces and body motions are decoupled, for instance, in radiation problem the body is under a prescribed motion, ϕ_t can be approximated by using a finite difference scheme after time series of ϕ is obtained (post-processing method). This method can be used as a comparison to validate other methods.

Specifically, by denoting the velocity potential of the collocation point i on the body surface (see Fig.3.7) at time t as $\phi_i(t)$ and the velocity of point i as $\boldsymbol{v_i}$, $d\phi_i/dt$ can be written as

$$\frac{d\phi_i(t)}{dt} = \frac{\partial \phi_i(t)}{\partial t} + \boldsymbol{v_i}\cdot\nabla\phi_i(t) \tag{3.33}$$

In this post-processing method, $d\phi_i/dt|_{t=t_0}$ could be evaluated by a central finite difference in terms of the information at $t = t_0 + n\Delta t$ and $t = t_0 - n\Delta t$. In the thesis, $d\phi_i/dt|_{t=t_0}$ is evaluated by the three-point central difference scheme, and thus

$$\frac{\partial \phi_i(t)}{\partial t}|_{t=t_0} = \frac{\phi_i(t_0 + \Delta t) - \phi_i(t_0 - \Delta t)}{2\Delta t} - \boldsymbol{v_i}(t_0)\cdot\nabla\phi_i(t_0) \tag{3.34}$$

Note that $\boldsymbol{v_i}$ equals neither the body velocity nor $\nabla\phi$, because of mesh movement. However, it can be evaluated in a similar manner to that for $d\phi_i/dt$, since the trajectory of node i is known as shown in Fig. 3.7.

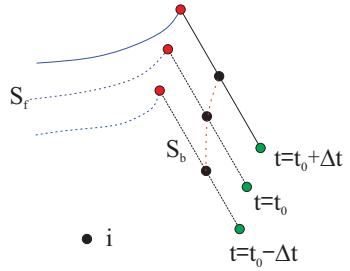

FIGURE 3.7: Evolution of free surface and wetted body surface.

It should be noted here that the central difference scheme is only applicable to the case that body is in forced motion. Once the body is under a free motion, ϕ_t can only be approximated by a backward finite difference method with lower accuracy compared to the central difference approximation.

In contrast to the above-mentioned methods that ϕ_t is explicitly determined, in the following method, the hydrodynamic forces are evaluated without explicitly solving ϕ_t. For a vector field $\boldsymbol{q}$, the time derivative of flux can be expressed as

$$\frac{d}{dt}\iint_{s(t)} \boldsymbol{q}\cdot\boldsymbol{n}ds = \iint_{s(t)} [\frac{\partial \boldsymbol{q}}{\partial t} + \boldsymbol{v}(\nabla\cdot\boldsymbol{q}) + \nabla\times(\boldsymbol{q}\times\boldsymbol{V})]\cdot\boldsymbol{n}ds \tag{3.35}$$

where $\boldsymbol{v}$ is the velocity of surface $s(t)$ and $s(t)$ is not necessarily enclosed. Applying Stokes theorem to Eq.(3.35), yields

$$\frac{d}{dt}\iint_{s(t)} \boldsymbol{q}\cdot\boldsymbol{n}ds = \iint_{s(t)} [\frac{\partial \boldsymbol{q}}{\partial t} + \boldsymbol{v}(\nabla\cdot\boldsymbol{q})]\boldsymbol{n}ds + \oint_c (\boldsymbol{v}\times\boldsymbol{l})\cdot\boldsymbol{q}dl \tag{3.36}$$

where $\boldsymbol{l}$ denotes tangential vector on the edge of $s(t)$. Let $\boldsymbol{v} = \nabla\phi$, $\boldsymbol{q} = \phi\boldsymbol{i}$ and $s(t) = S_b$, we have the following relation

$$\frac{d}{dt}\iint_{S_b} \phi n_1 ds = \iint_{S_b} [\frac{\partial\phi}{\partial t} + (\frac{\partial\phi}{\partial x})^2]n_1 ds + \oint_c \phi(\phi_x l_z - \phi_z l_y)dl \tag{3.37}$$

where c is time-dependent waterline with tangential vector $\boldsymbol{l}$. A step further,

$$\iint_{S_b} \frac{\partial\phi}{\partial t} n_1 ds = \frac{dI_1}{dt} - \iint_{S_b} (\frac{\partial\phi}{\partial x})^2 n_1 ds - \oint_c \phi(\phi_x l_z - \phi_z l_y)dl \tag{3.38}$$

here $I_1 = \iint_{S_b} \phi n_1 ds$. We denote this method as impulse method. Following this way, the hydrodynamic force in x direction can be written as follows

$$F_1 = -\rho \frac{dI_1}{dt} + \rho \iint_{S_b} \frac{1}{2}(\frac{\partial \phi}{\partial x})^2 n_1 ds - \rho \iint_{S_b} gz n_1 ds + \rho \oint_c \phi(\phi_x l_z - \phi_z l_y) dl \tag{3.39}$$

3.3 Higher-order boundary element method (HOBEM)

In solving nonlinear wave-body interaction problems in the time domain, one challenge is to seek for the boundary-value solution accurately. As illustrated in Fig.3.1, the computation starts or restarts from a status that the velocity potential ϕ is known on free surface and ϕ_n is known on body surface. And therefore, the key objective in solving this BVP is to determine ϕ_n on free surface and ϕ on body surface. Specifically, the BVP can be written as follows

$$\begin{cases} \nabla^2 \phi = 0 \\ \phi = \phi_0 \quad S_f \\ \phi_n = V_n \quad S_b \end{cases} \tag{3.40}$$

Based on Green's third identity, the Laplace equation is transformed into boundary integral equation (BIE) over the entire surface S (Newman [47]),

$$c(p)\phi(p) = \iint_S \phi_n(q) G(p;\boldsymbol{q}) ds - \iint_S \phi(q) G_n(p;q) ds \tag{3.41}$$

where p is field point and q is source field; $G(p;q) \equiv 1/|p-q|$ is the Rankine source Green function. $c(p)$ is the solid angle at point p.

Eq.(3.41) can be interpreted that for given point p, the velocity potential ϕ can be determined by source distribution with strength ϕ_n and dipole distribution of strength ϕ on the entire boundary surface S. If the surface is discreted by piece-wise element with $N_b + N_f$ collocation points in total, where N_f is the amount of points on free surface and N_b on body surface, respectively, $N_b + N_f$ linear equations can be established according to Eq.(3.41). As a consequence, N_f unknowns of ϕ_n on free surface and N_b unknowns of ϕ on body surface can be determined by solving the linear system of equations. This is the central idea of boundary element method (BEM).

When dealing with Eq.(3.41) numerically, the constant panel method (CPM) is the most commonly used BIE solver because of its simplicity in implementation, where the boundary S is approximated by small flat patches (elements) ignoring the local curvature with an assumption that the strength of source/diople is a constant over each patch. However, it is apparent that CPM possesses several fundamental shortcomings which limit its applications to the wave-body

interactions problems. First of all, a relatively large number of panels are required to achieve accurate representations of the geometry and physical quantities because of the low convergence rate of CPM. Secondly, CPM does not converge for those BVPs with non-smoothly connected boundaries due to numerical discontinuous approximations along the intersection lines. Thirdly, the spatial derivatives of the velocity potential such as velocity and acceleration cannot be evaluated accurately and robustly, especially near the intersections, edges, and corners[6].

As an improvement compared to CPM, the higher-order boundary element method (HOBEM) is capable of avoiding the shortcomings of CPM and is relatively effective and accurate in dealing with various BVPs. HOBEM assumes each boundary element to be curvilinear quadrilateral where nine collocation points are located. A quadratic isoparametric interpolation is used to represent the geometry as well as all variables on each element. Following this procedure, the boundary is firstly discreted by NT quadratic isoparametric elements and Eq.(3.41) can be written as follows

$$c(p)\phi(p) + \sum_{i=1}^{NT} \iint_{S_i} \phi(q) G_n(p;q) ds = \sum_{i=1}^{NT} \iint_{S_i} \phi_n(q) G(p;q) ds \tag{3.42}$$

To carried out the integration over S_i, the nine-node element is then mapped into a parametric space $\varsigma - \tau$, with $\varsigma \in [-1, 1]$ and $\tau \in [-1, 1]$ as shown in Fig.3.8. Let Ψ represent one of

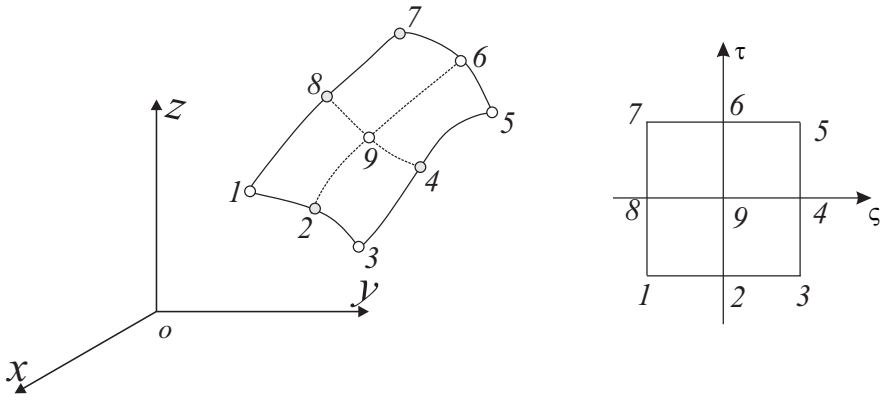

FIGURE 3.8: Mapping between physical space and parametric space.

the parameter (x, y, z, ϕ, ϕ_n). According to the quadratic isoparametric interpolation, within one element, Ψ can be appreciated by the following approximation

$$\Psi(\varsigma, \tau) = \sum_{m=1}^{9} L_m(\varsigma, \tau) \Psi_m \tag{3.43}$$

where $L_m(\varsigma,\tau)$ is the Lagrangian interpolation function or shape function with the form written as follows[6]

$$\begin{cases} L_m(\varsigma,\tau) = \dfrac{1}{4}\varsigma(\varsigma+\varsigma_m)\tau(\tau+\tau_m), & m = 1,3,5,7 \\ L_m(\varsigma,\tau) = \dfrac{1}{2}(1-\tau_m^2\varsigma^2-\varsigma_m^2\tau^2)[\tau_m\tau(1+\tau_m\tau)+\varsigma_m\varsigma(1+\varsigma_m\varsigma)], & m = 2,4,6,8 \\ L_9(\varsigma,\tau) = (1-\varsigma^2)(1-\tau^2) \end{cases} \tag{3.44}$$

where ς_m and τ_m represent coordinates of the m-th point in parametric space.

Following Eq.(3.43) and Eq.(3.44), the integration in Eq.(3.42) can be rewritten as follows

$$\begin{cases} \iint_{S_i} \phi(q)G_n(p;q)ds = \sum_{m=1}^{9} \phi_m(q) \iint_{S_i} L_m(\varsigma,\tau)G_n(\varsigma,\tau)J(\varsigma,\tau)ds \\ \iint_{S_i} \phi_n(q)G(p;q)ds = \sum_{m=1}^{9} \phi_{n_m}(q) \iint_{S_i} L_m(\varsigma,\tau)G(\varsigma,\tau)J(\varsigma,\tau)ds \end{cases} \tag{3.45}$$

where $J(\varsigma,\tau)$ is the Jacobian associated with the transformation between physical space and parametric space. A step further, Eq.(3.45) can be evaluated by Gaussian quadrature. Substituting Eq.(3.45) into Eq.(3.42) yields

$$\begin{aligned} &c(p)\phi(p) + \sum_{i=1}^{NT}\sum_{m=1}^{9} \phi_m(q) \iint_{S_i} L_m(\varsigma,\tau)G_n(\varsigma,\tau)J(\varsigma,\tau)ds = \\ &\sum_{i=1}^{NT}\sum_{m=1}^{9} \phi_{n_m}(q) \iint_{S_i} L_m(\varsigma,\tau)G(\varsigma,\tau)J(\varsigma,\tau)ds \end{aligned} \tag{3.46}$$

The imposition of Eq.(3.46) at Np collocation points on S_f and S_b leads to a system of Np linear equations:

$$[H]\{x\} = \{b\} \tag{3.47}$$

where [H] is a $Np \times Np$ matrix of influence coefficients, $\{x\}$ the vector of Np unknowns consisting of ϕ_n on S_f and ϕ on S_b on the collocation points, and $\{b\}$ the known vector.

In the procedure of impedimentary the HOBEM, there are still lots of detail worthy of mention, although some of them is well-known. For completeness, here we only highlight a fast solution on these issues and list references which are referred to in the research.

3.3.1 Treatment on singular and weakly singular integration

As we can see in Eq.(3.45) when p approaches q the integration is weakly nonlinear, while when p is coincident with q there is singularity in the integration. In CPM there is analytical method

to evaluate this integration [48], while in HOBEM all integration (singular and non-singular) must be evaluated numerically.

In terms of weakly-singular integration, a sub-division scheme is used, where once the minimum distance dl between field point p and the element E_i is comparable with the characteristic length ds of the element, E_i is then divided into several sub-elements. The sub-division continues until $dl \gg ds$. The procedure is illustrated in Fig.3.9 and more details can be found in Mania [25].

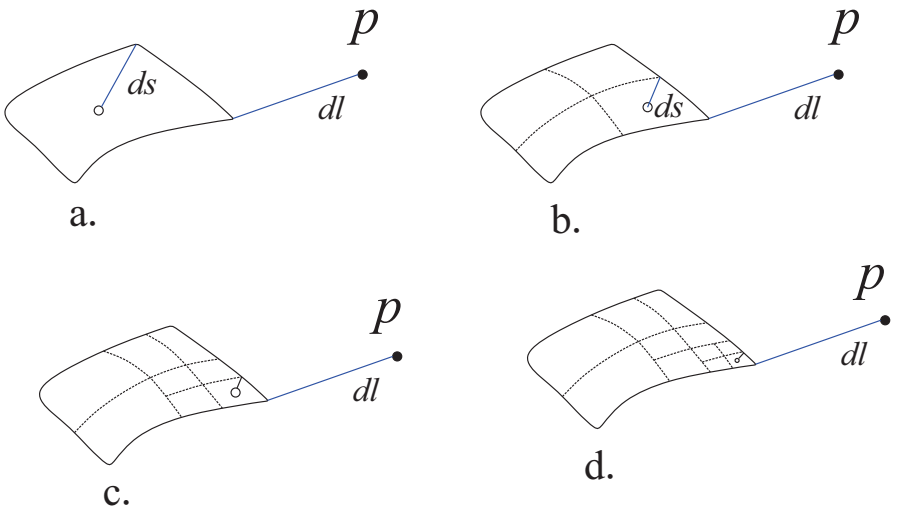

FIGURE 3.9: Sun-division scheme for weakly-singular integration.

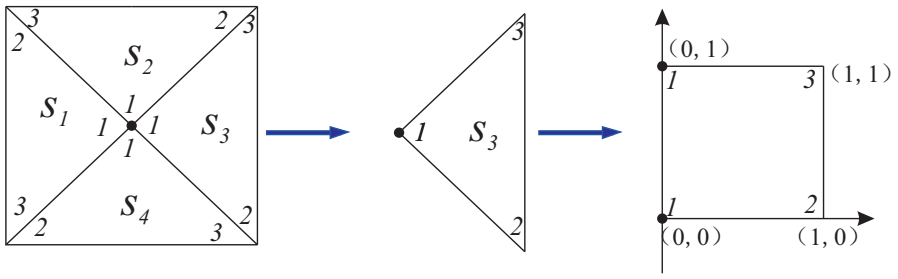

FIGURE 3.10: Coordinate transformation to calculate the singular integration when $\boldsymbol{p}$ is inside of E_i.

As far as the singular integration is concerned, where p is inside of element E_i see Fig.3.10, the element in $\varsigma - \tau$ space is firstly divided into several triangle elements with the singular point as the shared vertex. And then the triangle polar co-ordinates are used to reduce the order of singularity of the boundary integrals by one degree. And the integration is carried out over mapping of the boundary elements onto plane square. By doing so, a Jacobin is introduced, whose value approaches zero as integration point approaches the singular point. As a consequence, the integration is smooth everywhere and a typical Gaussian quadrature can be applied. The procedure is illustrated in Fig.3.10 and more details can be found in Li [49].

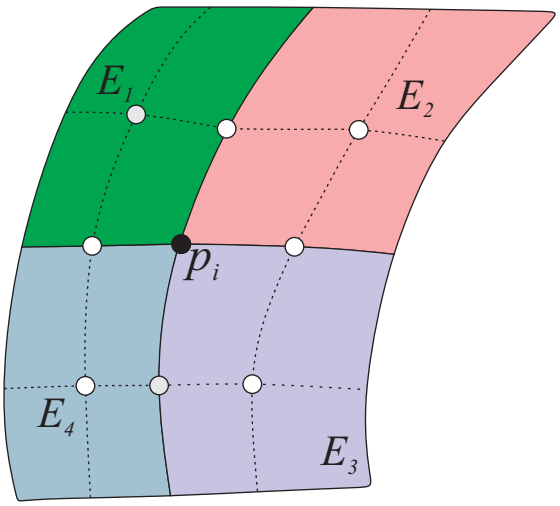

FIGURE 3.11: Connectivity of the element.

3.3.2 Evaluation of special derivative

In the HOBEM method, both geometry and field values (e.g. ϕ and ϕ_n) are approximated by local quadratic polynomial, where the first special derivative is continuous and the second special derivative is a constant within the element. However, at some collocation point where the point may be shared by two or four elements, see Fig.3.14, there is only C^0 continuity, which indicates neither the first derivative nor the second derivative is continuous due to property of the local approximation. Actually, when evaluating the special derivative in a post-processing procedure, in most cases (except the central points), this problem occurs, which in turn affects the accuracy of normal vector and velocity field.

To solve this problem, the collocation point e.g. p_i which is shared by 4 elements is considered as central point of a new isoparametric element (see the figure), where the surrounding neighbouring points can be determined at the beginning of computation. By doing so, almost all the collocation points are placed at the center of the isoparametric elements, except some point at corner, and thus a continuous and accurate special derivative can be evaluated for most cases. For the corner point, some special scheme is used which would be described later.

We take the evaluation of velocity at central point of a element as an example to illustrate this scheme. According to chain rule in elementary Calculus, the velocity can be written as follows,

$$\begin{bmatrix} \phi_x \\ \phi_y \\ \phi_z \end{bmatrix} = \begin{bmatrix} x_\varsigma & y_\varsigma & z_\varsigma \\ x_\tau & y_\tau & z_\tau \\ n_x & n_y & n_z \end{bmatrix}^{-1} \begin{bmatrix} \phi_\varsigma \\ \phi_\tau \\ \phi_n \end{bmatrix} \tag{3.48}$$

where Ψ_ς or Ψ_τ can be determined by the following expression, where Ψ represents one of parameter from the set (x, y, z, ϕ).

$$\begin{cases} \Psi_\varsigma = \sum_{m=1}^{9} \Psi_m \dfrac{\partial L_m}{\partial \varsigma} \\ \Psi_\tau = \sum_{m=1}^{9} \Psi_m \dfrac{\partial L_m}{\partial \tau} \end{cases} \tag{3.49}$$

Note that Kim and Kim [50] also derived a similar scheme for evaluating the second special derivative. Other useful reference can be found in Banerjee and Butterfield[51].

3.3.3 Evaluation of solid angle

In physics, the solid angle is defined by ratio of the spherical surface in the fluid domain to the whole spherical surface as shown in Fig.3.12. And thus its expression can be written as follows

$$C(o) = S_\varepsilon / 4\pi\varepsilon^2 \tag{3.50}$$

where ε is the radius of a sphere with origin at o.

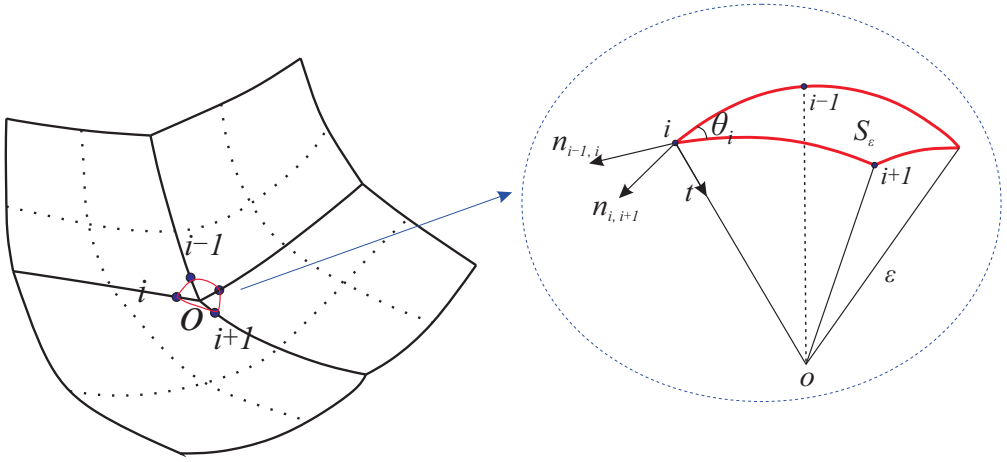

FIGURE 3.12: Sketch of the solid angle.

Following the definition, one straightforward method to evaluate the solid angle is to calculate S_ε. According to spherical geometry [52][53] [54], the following relation holds

$$S_\varepsilon = \varepsilon^2 (\sum_{i=1}^{Ne} \theta_i - (Ne - 2)\pi) \tag{3.51}$$

where Ne denotes the total number of element shared point o and θ_i the angle contained by the two neighbouring elements and the interpolated spherical surface, see Fig.3.52. And θ_i can be

further commutated by following expression[55]

$$\theta_i = \pi + sgn[(\boldsymbol{n}_{i-1,i} \times \boldsymbol{n}_{i,i+1}) \cdot \boldsymbol{t}_i] \arccos(\boldsymbol{n}_{i-1,i} \cdot \boldsymbol{n}_{i,i+1}) \tag{3.52}$$

where *sgn* is the signum function, $\boldsymbol{n}_{i,i+1}$ the unit normal vector (outward), and $\boldsymbol{t}_i$ the unit tangential vector on the intersecting edges between two elements.

Apparently, the above-mentioned method is a direct method to evaluate the solid angle. Another method referred to as indirect method can be expressed as follows

$$C(p) = \lim_{p \to q} \iint_s \frac{\partial G(p;q)}{\partial n} ds = -\iint_s \frac{\partial G(p;q)}{\partial n} ds \tag{3.53}$$

where s must be a closed surface.

Comparatively speaking, the direct method is more efficient to implement than the indirect method, since in the indirect method the whole enclosed boundary must be meshed and this mesh is also involved in the procedure of setting up matrix of coefficient, which would increase computational burden. On the other hand, the direct method is dependent on local geometry and thus it's accuracy is easily affected by local error (e.g. the saw-tooth instability), while the indirect method is a global approximation and is not sensitive to local error. In this thesis, both methods are used to evaluate the solid angle, where the indirect method is used near the waterline and the direct method is applied to the remaining region.

3.3.4 Double-node technique

At corners, maximum error tends to occur because of abrupt change of normal vector at intersection. In double nodes technique, the coordinates and ϕ of both nodes are the same but the

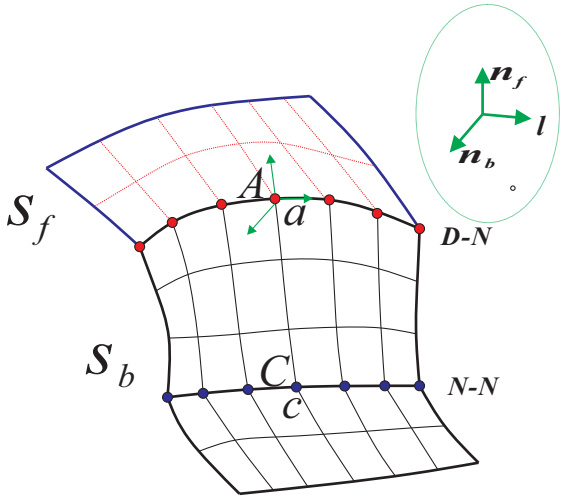

FIGURE 3.13: Illustration of Dirichlet-Neumann type and Neumann-Neumann type double node.

normal vector differ, and therefore $\partial\phi/\partial n$ is different. To avoid overdetermination of the problem (because additional node is added into the system), the final influence matrix need proper modification.

- ***Dirichlet-Neumann*** type double node.

  At waterline, double node A belongs to free surface with given ϕ_A and unknown $\partial\phi/\partial n_f$, where $\boldsymbol{n_f}$ is normal vector on S_f. While at node a on body surface ϕ_a is unknown and $\partial\phi/\partial n_b$ is given. However, because of continuity of ϕ i.e. $\phi_a = \phi_A$, no unknown is left at node a. Without modification the final matrix is over-determined (singular). The corresponding modification on influence matrix $[H]$ and right-hand side vector $\{b\}$ is written below

$$\begin{aligned} H_{ai} &= 0 \quad \forall i \neq a \quad H_{aa} = max \\ b_a &= max\phi_A \end{aligned} \tag{3.54}$$

  where max is the maximum diagonal element in $[H]$ and it ensures good condition number of the linear system.

- ***Neumann-Neumann*** type double node.

  At double node C and c on body surface, two equations are obtained for C and c in the algebraic system, each of them for the same unknown potential at the corner. Hence, the system matrix is singular. To make it solvable, one of the equations, say at node c, is modified on a way similar to above,

$$\begin{aligned} H_{ci} &= 0 \quad \forall i \neq c, C \quad H_{cc} = max \\ H_{cC} &= -max \quad b_c = 0 \end{aligned} \tag{3.55}$$

- ***Dirichlet-Dirichlet*** type double node.

  At this type corner, the initial problem itself seems singular, because we require two unknowns at one point (one equation). Even by double node technique, it provides two same equation in the final matrix and thus useless. This type of corner is encountered on far-field radiation boundary if we impose ϕ on this surface. Fortunately, we would use artificial damping at far field and no such corner would arise.

After solving the BVP, taking waterline as example, at each node we have ϕ, ϕ_{nf} and ϕ_{nb}, and $\nabla\phi$ can be obtained by following expression

$$\begin{bmatrix} n_{bx} & n_{by} & n_{bz} \\ n_{fx} & n_{fy} & n_{fz} \\ l_x & l_y & l_z \end{bmatrix} \begin{bmatrix} \phi_x \\ \phi_y \\ \phi_z \end{bmatrix} = \begin{bmatrix} \phi_{nb} \\ \phi_{nf} \\ \phi_l \end{bmatrix} \tag{3.56}$$

where $\boldsymbol{l} = (l_x, l_y, l_z)$ is tangential vector along water line and $\boldsymbol{n}_b$ normal vector on body. In current research, ϕ_l and $\boldsymbol{l}$ is approximated by 3^{rd}-order spline.

3.3.5 A simple case to validate HOBEM

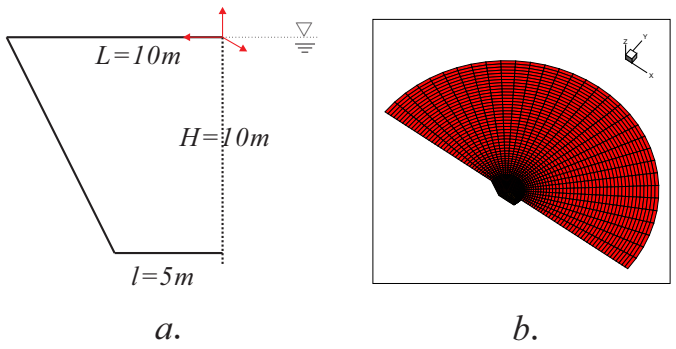

FIGURE 3.14: Sketch of the computational domain. a. the body is formed by rotation of a trapezoid; b. Mesh of the domain, 528 quadratic elements are used, with 208 elements on body surface and 320 on free surface.

For validation capacity of the HOBEM, an isolate source is put at $(0, 0, 10)$ with strength σ. Thus the resulting ϕ at point (x,y,z) is

$$\phi(x, y, z) = \frac{x\sigma}{R^3} \quad R = \sqrt{x^2 + y^2 + (z - 10)^2} \tag{3.57}$$

We impose a Dirichlet condition on free surface and a Neumann condition on body surface according to Eq.(3.57). The computational domain is illustrated in Fig.3.14. Because of symmetry of the domain, only half domain is used.

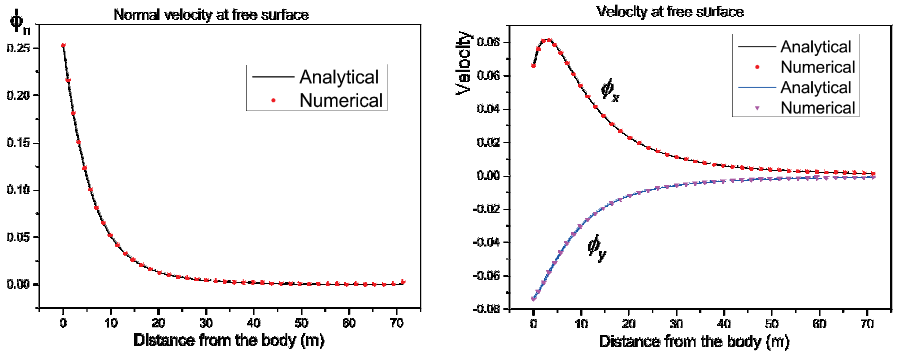

FIGURE 3.15: Normal and horizontal velocity on free surface along a radial direction.

Fig.3.15 illustrates velocity on free surface along a radial direction. As we can see, the accuracy of the first spatial derivatives of velocity potential is good. Since the velocity is evaluated by a numerical interpolation based on ϕ and ϕ_n, the result also indicates the basic solutions evaluated

by HOBEM is accurate. Note that, in the present research, there is only first special derivatives appearing in ALE-type free surface conditions and the second spatial derivatives appearing in body conditions of ϕ_t are transformed to first order. And thus, there is no need to evaluate the second spatial derivative in the present research.

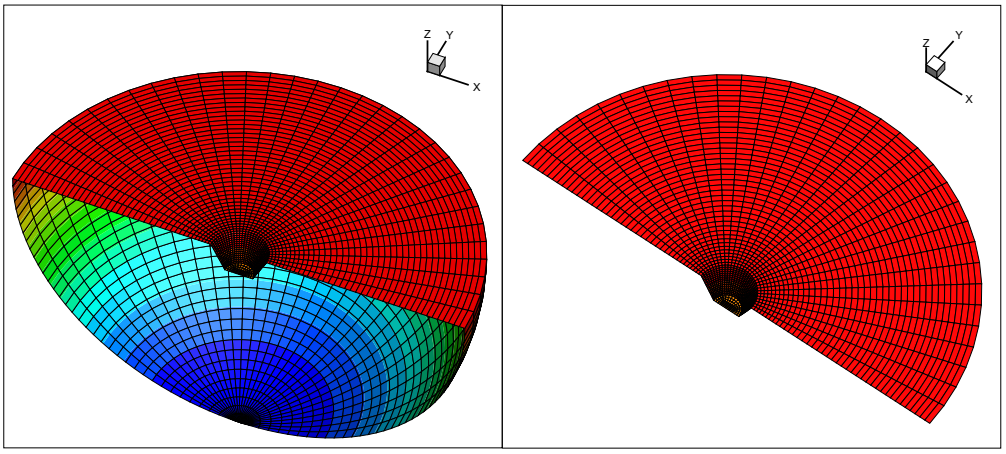

FIGURE 3.16: Mesh used for evaluation solid angle, for *indirect* method and *direct* method.

TABLE 3.1: The value of solid angle at waterline and intersection line on bottom of the body.

	Waterline			Corners at bottom		
Num	Indirect	Direct	Ana.	Indirect	Direct	Ana.
1	0.3238	0.3238	0.3238	0.6762	0.6762	0.6762
2	0.3334	0.3334	0.3234	0.6743	0.6742	0.6762
3	0.3427	0.3427	0.3427	0.6824	0.6823	0.6823
4	0.3471	0.3471	0.3471	0.6879	0.6879	0.6879
5	0.3489	0.3488	0.3488	0.6916	0.6916	0.6916

Tab.(3.1) illustrates solid angle calculated by these two approaches at five successive points, where the first point locates at right edge of the body. As we can see, at this case both approaches give almost identical results.

Tab.(3.2) illustrates $\nabla\phi$ at nodal points from number 1 to number 17 on waterline, where number 1 is at body's left corner. As we can see, the overall accuracy is good compared to the analytical solution, which indicates the schemes involved in the computation e.g. double-node technique and spline approximation to evaluate tangential vector and velocity on waterline is validated.

TABLE 3.2: $\nabla\phi$ at nodes on waterline

	ϕ_x			ϕ_y			ϕ_z		
N	Ana.	Num.	%	Ana.	Num.	%	Ana.	Nume.	%
1	0.0884	0.0885	0.208	-0.0000	-0.0000	-	0.265	0.2647	0.138
2	0.0858	0.0860	0.217	-0.0258	-0.0258	-0.042	0.2638	0.2635	0.122
3	0.0782	0.0784	0.197	-0.0507	-0.0507	-0.068	0.2600	0.2598	0.092
4	0.0660	0.0662	0.323	-0.0736	-0.0737	-0.085	0.2537	0.2534	0.125
5	0.0495	0.0498	0.528	-0.0937	-0.0938	-0.116	0.2449	0.2445	0.161
6	0.0294	0.0296	0.625	-0.1102	-0.1103	-0.089	0.2338	0.2335	0.124
7	0.0065	0.0067	2.491	-0.1224	-0.1225	-0.088	0.2204	0.2202	0.125
8	-0.0183	-0.0182	-0.612	-0.1300	-0.1301	-0.070	0.2049	0.2047	0.100
9	-0.0441	-0.0440	-0.223	-0.1325	-0.1326	-0.074	0.1875	0.1873	0.106
10	-0.0700	-0.0700	-0.082	-0.1300	-0.1301	-0.054	0.1682	0.1680	0.077
11	-0.0949	-0.0949	-0.027	-0.1224	-0.1225	-0.031	0.1473	0.1472	0.044
12	-0.1178	-0.1178	-0.015	-0.1102	-0.1102	-0.030	0.1249	0.1249	0.043
13	-0.1379	-0.1379	-0.010	-0.0937	-0.0937	-0.036	0.1014	0.1015	0.052
14	0.1544	-0.1544	-0.001	-0.0736	-0.0736	-0.013	0.0769	0.0769	0.019
15	-0.1666	-0.1666	-0.005	-0.0507	-0.0507	-0.095	0.0517	0.0516	0.148
16	-0.1742	-0.1741	-0.019	-0.0258	-0.0262	-1.312	0.0259	0.0253	2.307
17	-0.1767	-0.1767	-0.000	0.0000	-0.0000	-	0.000	-0.0000	-

Chapter 4

Study on nonlinear wave diffraction by a non-wall-sided structure

In industry of ocean engineering, flared geometry may arise in design of fixed offshore structures. An example is the Draugen oil production platform which was installed in the Haltenbanken area of the Norwegian Sea in 1993 (Wang, Wu and Drake[56]). The platform has a prestressed concrete monotower substructure with a flare above the mean sea level to provide efficient support for the integrated topside facilities. Simulations that take into account the geometry of non-wall-sided bodies in steep waves are important in these cases.

4.1 Problem definition

In the framework of potential flow theory, the total velocity potential (including incident wave and diffracted wave component) is subject to the following BVP,

$$\begin{cases} \nabla^2\phi = 0 \\ \dfrac{\partial\eta}{\partial t} = \dfrac{\partial\phi}{\partial z} - \nabla\phi\cdot\nabla\eta \quad \boldsymbol{x}\in S_f \\ \dfrac{\partial\phi}{\partial t} = -g\eta - \dfrac{1}{2}\nabla\phi\cdot\nabla\phi \quad \boldsymbol{x}\in S_f \\ \dfrac{\partial\phi}{\partial n} = 0 \quad \boldsymbol{x}\in S_b \end{cases} \tag{4.1}$$

Note that at far field on the truncated surface, an appropriate radiation condition should also be imposed avoid unwanted wave reflection.

Instead of using a wave maker to generate nonlinear incident wave, in the present study, the fifth-order Stokes[57] wave model is used as incident wave. Since the incident wave is explicitly

defined, the total velocity potential ϕ can therefor be decomposed as, $\phi = \phi^I + \phi^D$, where ϕ^I denotes velocity potential of incident wave and ϕ^D governs the remaining disturbed wave field i.e. diffracted wave field. Substituting this decomposition into Eq.(4.1) yields[58]

$$\begin{cases} \nabla^2\phi^D = 0 \\ \dfrac{\partial\eta}{\partial t} = \dfrac{\partial(\phi^I + \phi^D)}{\partial z} - \nabla(\phi^I + \phi^D)\cdot\nabla\eta \quad \boldsymbol{x} \in S_f \\ \dfrac{\partial\phi^D}{\partial t} = -\dfrac{1}{2}\nabla(\phi^I + \phi^D)\cdot\nabla(\phi^I + \phi^D) - g\eta - \dfrac{\partial\phi^I}{\partial t} \quad \boldsymbol{x} \in S_f \\ \dfrac{\partial\phi^D}{\partial n} = -\dfrac{\partial\phi^I}{\partial n} \quad \boldsymbol{x} \in S_b \end{cases} \tag{4.2}$$

Since ϕ^D decays rapidly at far field, smaller computational domain can be used, compared to the original problem, Eq.(4.1). Under the same reason, wave absorption at far field is more easy to implement than the original problem. What's more, this decomposition enables application of a variety of well-developed wave models as incident wave. A systematic validation on this method can be found in Ducrozet et al [59].

Taking into account the above mentioned decomposition and rewriting the free surface conditions in ALE form, yields

$$\begin{cases} \nabla^2\phi^D = 0 \\ \dfrac{\delta\boldsymbol{x}}{\delta t} = \dfrac{\phi_n^I + \phi_n^D}{l_n}\boldsymbol{l} \\ \dfrac{\delta\phi^D}{\delta t} = -\dfrac{1}{2}\nabla(\phi^D + \phi^I)\cdot\nabla(\phi^D + \phi^I) - g\eta - \dfrac{\partial\phi^I}{\partial t} + \dfrac{\delta\boldsymbol{x}}{\delta t}\cdot\nabla\phi^D \\ \dfrac{\partial\phi^D}{\partial n} = -\dfrac{\partial\phi^I}{\partial n} \quad \boldsymbol{x} \in S_b \end{cases} \tag{4.3}$$

It should be pointed out that both kinematic and dynamic free surface conditions are imposed on $z = \eta$ (not η^D). And at every time step we can get a new free surface position η and ϕ^D by time integration of above expressions.

It is worth noting that Eq.(4.3) does not include damping terms which are used for absorbing disturbed wave energy in far field. And introducing these terms into Eq.(4.3) is not as straightforward as putting these terms into right-hand side of free surface conditions in ALE form, which is true in general case. The reason is that additional terms in second and third equation of Eq.(4.3) would destroy our initial objective that fluid markers are always stay on a prescribed path and would further introduce numerical error.

To introduce damping terms, we should come back to the beginning of our derivation in ALE scheme. Suppose the free surface conditions with damping terms can be written as

$$\begin{cases} \dfrac{\partial \eta}{\partial t} = \dfrac{\partial \phi}{\partial z} - \nabla\phi \cdot \nabla\eta - \mu(r)\eta \\ \dfrac{\partial \phi}{\partial t} = -g\eta - \dfrac{1}{2}\nabla\phi \cdot \nabla\phi - \mu(r)\phi \end{cases} \tag{4.4}$$

where $\mu(r)$ is numerical damping coefficient and has a nonzero value inside the damping zone. And it can be given as follows,

$$\mu(r) = \begin{cases} \alpha\omega \dfrac{(r - R_0)^2}{(\beta\lambda)^2}, & R_0 \le r \le R_D \\ 0, & r < R_0 \end{cases} \tag{4.5}$$

where ω is circular frequency of incident wave, R_0 starting point of damping zone, R_D radius of outer boundary, and α, β are coefficients to control strength and length of the damping zone. In current study, α and β are set to 1.

Eq.(4.4) is the new free surface conditions taking into account numerical damping terms. Recalling the two constraint conditions that a fluid marker moves along prescribed path on free surface and following the similar procedure as described above, the ALE type free surface conditions with numerical damping can be given as follows,

$$\begin{cases} \dfrac{\delta \boldsymbol{x}}{\delta t} = \dfrac{\phi_n^I + \phi_n^D}{l_n}\boldsymbol{l} - \mu(r)\dfrac{\eta - \eta^I}{\boldsymbol{l} \cdot \nabla(z - \eta)}\boldsymbol{l} \\ \dfrac{\delta \phi^D}{\delta t} = -\dfrac{1}{2}\nabla(\phi^D + \phi^I) \cdot \nabla(\phi^D + \phi^I) - g\eta - \dfrac{\partial \phi^I}{\partial t} + \dfrac{\delta \boldsymbol{x}}{\delta t} \cdot \nabla\phi^D - \mu(r)\phi^D \end{cases} \tag{4.6}$$

Eq.(4.6) is the final form of ALE type free surface conditions. Although the expressions seem complicated compared with MEL and semi-lagrangian approach, the terms such as, ϕ^D, ϕ_n^D and their gradients, can be properly evaluated by HOBEM, which has been validated in previous chapter.

4.2 Noteworthy numerical techniques applied to current computation

In fully nonlinear computation, the wetted body surface is time-dependent and thus a robust remeshing scheme is required, especially for body with complex geometry. In current study, we firstly mesh the whole surface of the body (including geometry above still waterline). And then the sectional line (red line in Fig.4.1) is parameterized by cubic spline, which is the prescribed

path for intersection point. Following above-mentioned ALE procedure, the position of intersection point can be obtained at every instant, namely, waterline can be determined. Subsequently, the wetted portion of the curve represented by spline can be split into serval segments with same arc-length. And thus the mesh under waterline can be determined. This procedure for remeshing is illustrated in Fig.4.1.

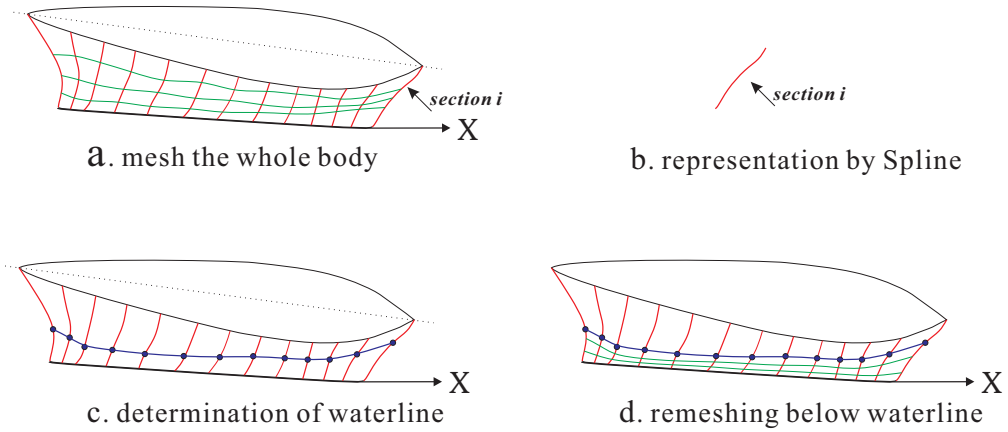

FIGURE 4.1: Sketch of remeshing procedure.

In Eq.(4.6), there is term containing $\nabla\eta$ and in general it can be evaluated by interpolation. However, $\nabla\eta$ is relevant to normal vector of free surface and can be obtained directly once unit normal vector of free surface is known. Recalling the definition of unit normal vector on free surface

$$(n_1, n_2, n_3) = \frac{(-\eta_x, -\eta_y, 1)}{\sqrt{(1 + \eta_x^2 + \eta_y^2)}} \tag{4.7}$$

and after simple manipulation $\nabla\eta$ can be expressed as

$$\eta_x = -\frac{n_1}{n_3}; \eta_y = -\frac{n_2}{n_3} \tag{4.8}$$

In order to avoid an abrupt start and allow a gradual development of the solutions, the amplitude of incident wave is modulated by following function:

$$M(t) = \begin{cases} \frac{1}{2}(1 - cos(\frac{\pi t}{T_m})), & t \leq T_m \\ 1, & t > T_m \end{cases} \tag{4.9}$$

where T_m is modulation period and chosen as $2T$ in present computation.

In addition, to suppress the so-called *saw-tooth* instability, a smoothing scheme introduced by Koo and Kim[2] is used, which is applied every 5 time steps when wave steepness exceeds $1/20$

and every 10 time steps for general cases. In the present computation, the 4^{th}-order Runge-Kutta method is used for time integration and GMRES[60] algorithm is used for solving the linear system equations.

4.3 Numerical results and discussions

4.3.1 Comparison with experiments and other simulations

In this subsection, we compute nonlinear wave diffraction by three kinds of geometry, circular cylinder, axisymmetrical body with flare and Bulk Carrier. And we compare the numerical results (wave elevation at specific point and wave exciting force exerting on body surface) with experiments and other simulations.

4.3.1.1 Case 1, wave diffraction by a circular cylinder

In case 1, the radius of the cylinder is taken as r = 8.0 m (D=16m) and the draft is 24.0 m. A brief review of the experiment setup relevant to present simulation will be given here and more details can be found in Sun and Zang [61]. A top view of selected wave probe locations is shown in Fig.4.2. Wave probes were installed in a radial pattern around the column, with a distance from the column wall of 0.2063 m (inner circle) and 8 m (outer circle). In the present computation, all wave parameters are listed in Tab.4.1. Here H is wave height and A is wave amplitude with

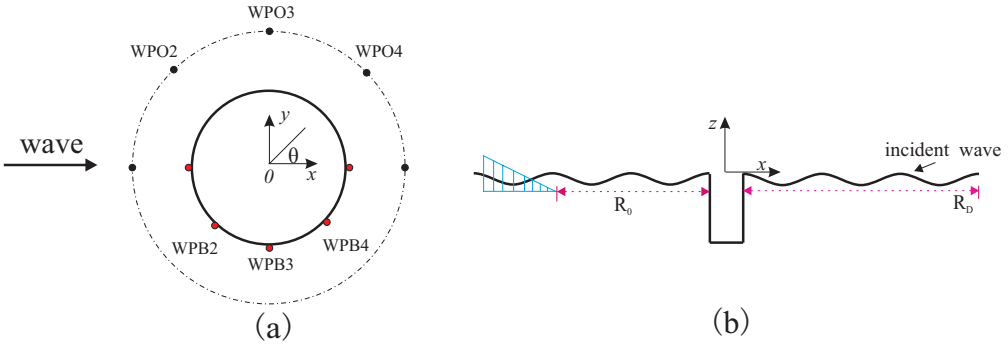

FIGURE 4.2: (a) layout of wave probes (top view). (b) sketch of computational domain (side view).

TABLE 4.1: Wave parameters in current computation.

H/λ	λ (m)	A (m)	T (s)	KC	water depth
1/16	126.36	3.949	9	1.5508	infinity

$H = 2A$. λ is wave length and T is wave period. The Keulegan-Carpenter number is 1.5508 and $2r/\lambda < 0.2$, which implies the flow lies within the drag-inertia regime.

In present computation, the radius of whole computational domain $R_D = 14D$ and the starting point of damping layer is located at R_0 with $R_0 = 2/3R_D$. The mesh of the computational domain at $t = T$ is illustrated in Fig.4.3. Since in current case, the nonlinear effect is distinct ($H/\lambda = 1/16$), we use a relatively small time step, $\delta t = T/100$.

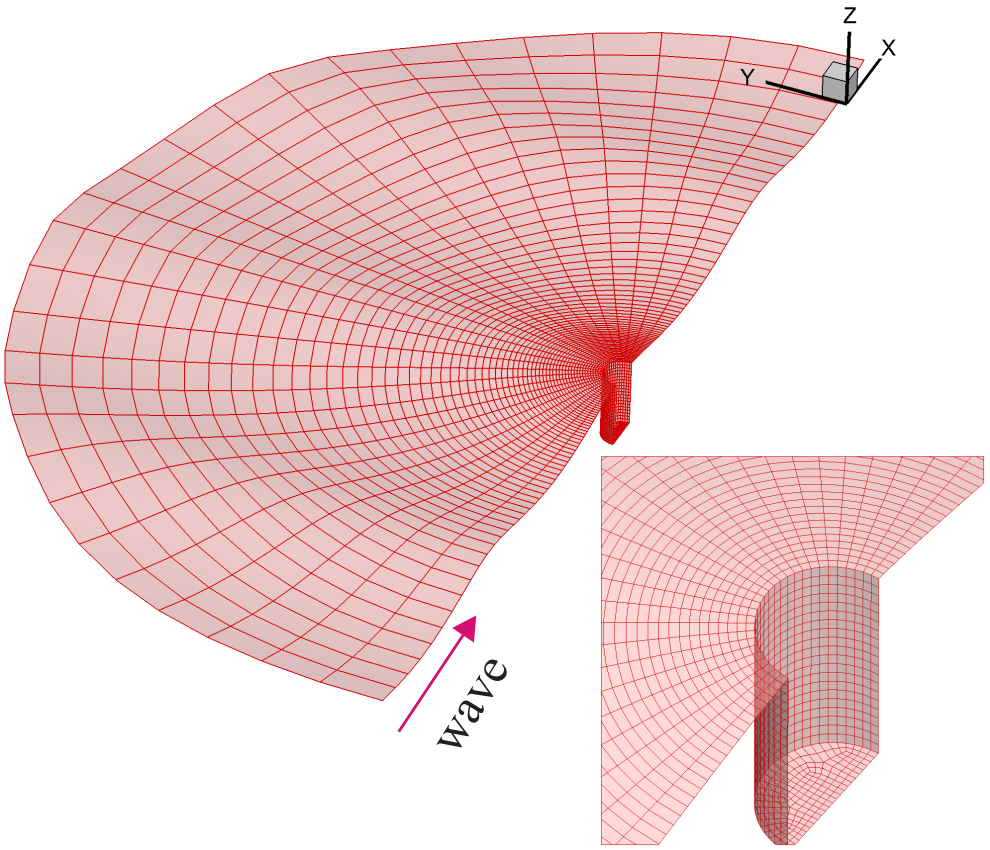

FIGURE 4.3: A sketch of the computational mesh.

Fig.4.4 illustrates time history of wave elevation at specific wave probe. Except red line in Fig.4.4, all other results come from Sun and Zang[61]. The results obtained by present potential flow based method agree well with experimental results and OpenFOAM. And the results obtained by 2^{nd}-order method seems over-predicted at some points. Fig.4.5 illustrates time history of force and a good agreement is observed.

4.3.1.2 Case 2, wave diffraction by a axisymmetrical body with flare

In order to study the flare effect, two axisymmetric bodies generated by rotation of the shape around z axis as illustrated in Fig.4.6 are evaluated in current subsection. In body1 case, $\theta = 85^\circ$ and $\theta = 75^\circ$ are studied with $B_1 = 3r_d = 15m$. And the wave amplitude is $A = 0.75m$ with wave steepness $1/13$. The wave run-ups on the front and the backside of the body are shown in

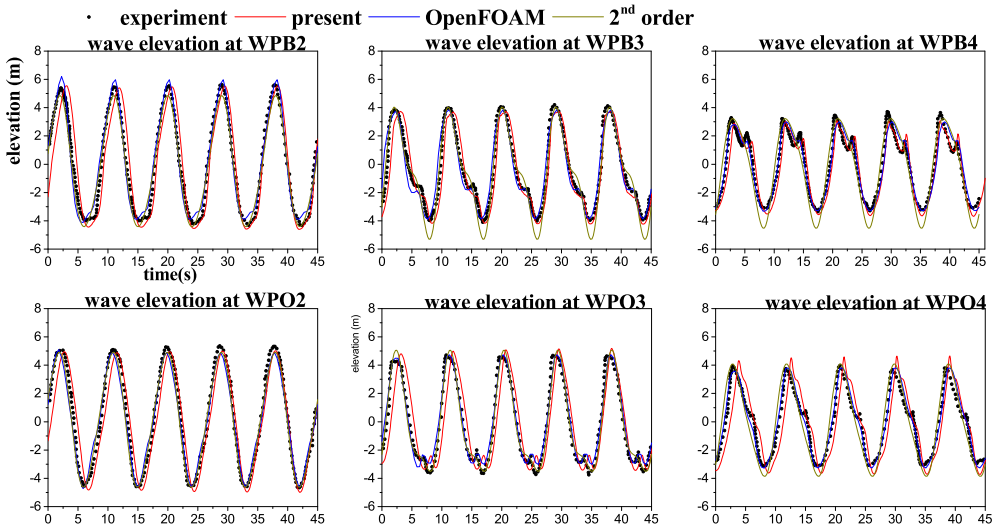

FIGURE 4.4: Time history of wave elevation at points.

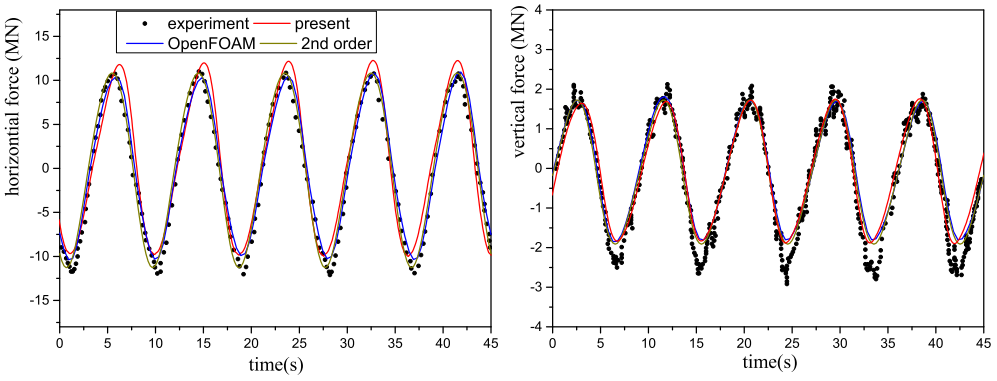

FIGURE 4.5: Time history of forces.

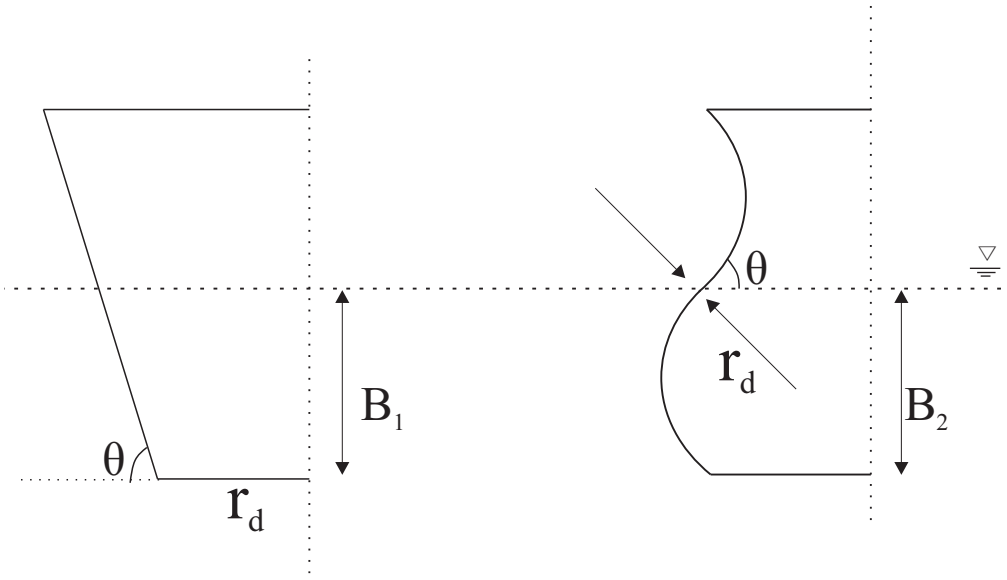

FIGURE 4.6: Sketch of truncated bodies formed by rotation of a plane shape, body1 and body2.

Fig.4.7, and the corresponding forces in Fig.4.8. The results are compared against Zhou's[62] results. As we can see, there are slight difference between these results. One possible reason is that in this case, we do not use modulation function (different initial value). And the other reason is that we use different incident wave model. It can be seen from Fig.4.7 that the wave run-up on the front side of the body is similar at these two angles, while it is smaller at $\theta = 85°$ on the back side of the body. Fig.4.9 illustrates snapshots of wave profile within one period

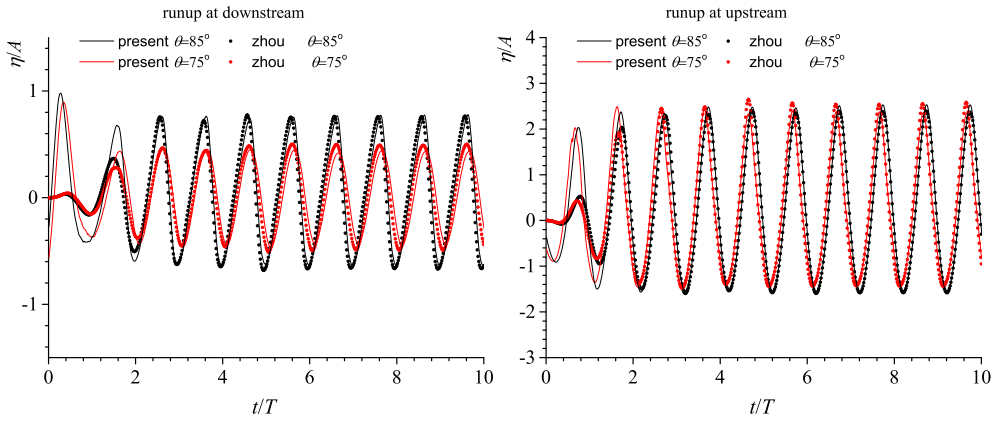

FIGURE 4.7: Wave runup of body1 at downstream and upstream with two kinds of flare angle.

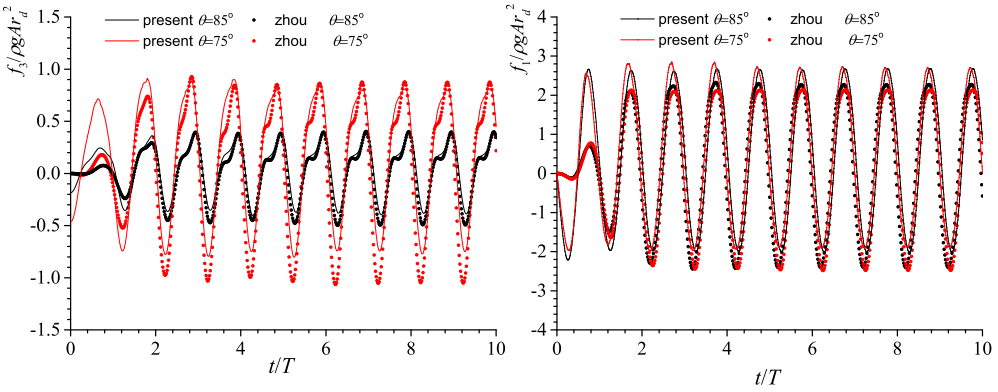

FIGURE 4.8: Wave exciting forces of body1 with two kinds of flare angle.

with $kA = 0.2512$. In this case, the wetted body surface is varied apparently, which affects wave run-ups as well as hydrodynamics.

In case of body2, The wave diffraction by geometry $\theta = 60°$ is studied with $B_2 = r_d = 5m$. And the wave amplitude is $A = 0.5m$ with wave steepness $1/20$. The wave run-up and wave exciting forces are illustrated in Fig.4.10. Note that geometry of body2 is very relevant to ship geometry near bulbous bow. From the results, distinct nonlinearity due to the flare in time history of wave run-ups on the backside is observed. And because of variation of wetted body surface, the nonlinearity of force in heave mode is very apparent.

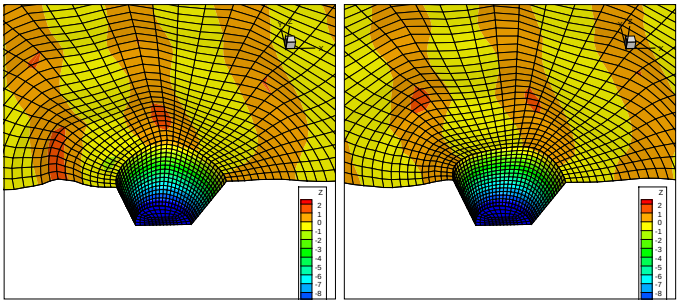

(a) t=5T (b) t=5.25T

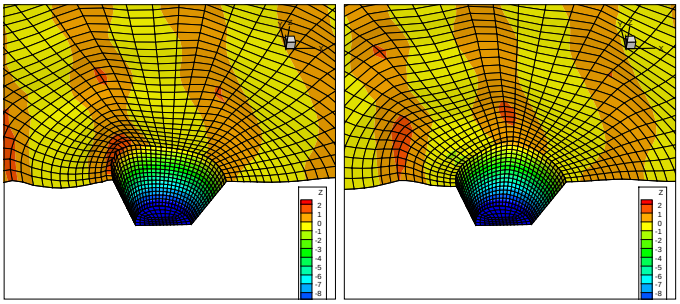

(c) t=5.5T (d) t=6T

FIGURE 4.9: Snapshots of wave profile within one period. $kA = 0.2512$

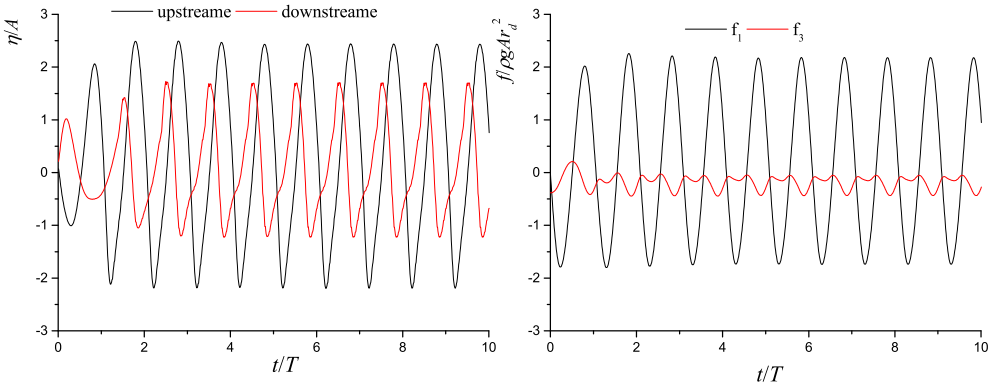

FIGURE 4.10: Wave run-up and exciting forces of body2.

4.3.1.3 Case 3, wave diffraction by a Bulk Carrier.

The ship model used in the computation and experiment is RIOS Bulk Carrier and it's principal dimensions are illustrated in Tab.4.2. Three wave probes are instilled with a distance from ship hull of 0.2m, see Fig.4.11. And in the present experiment, only waves near fore part of the ship is measured, where the exact locations of wave probes are instilled in Tab.4.3. In Tab.4.4, we list the selected wave conditions. In the table, H denotes wave height and ζ_a stands for incident wave amplitude with $H = 2\zeta_a$. T stands for period of incident wave, λ for wave length and k for wave number. Note that the values of wave parameters used here are derived from linear wave theory. It should be pointed out that in Tab.4.4 the incident wave amplitude, ζ_a is obtained

by measurement of incident wave in the towing tank, which is hereafter used in the numerical computation.

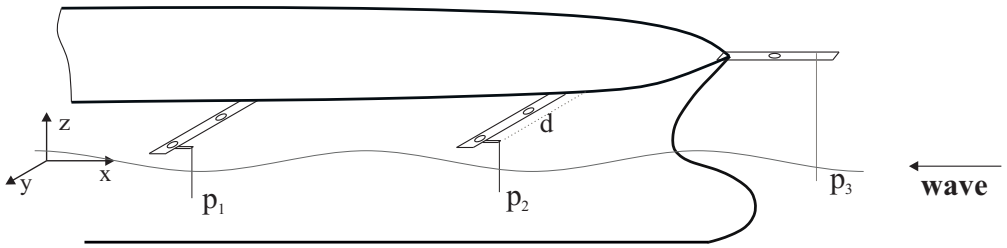

FIGURE 4.11: Configuration of wave probes.

TABLE 4.2: Principle dimensions

Length: L [m]	2.4
Breadth: B [m]	0.3846
Draft: d[m]	0.138
Displacement: $\nabla[m^3]$	0.0813
Center of gravity : x_G[m]	-0.0555
Center of gravity : z_G[m]	0.0136

TABLE 4.3: Position of wave probes

wave probe	$x(m)$	$y(m)$
P_1	0.3	0.4
P_2	0.9	0.361
P_3	1.4	0.0

TABLE 4.4: Selected wave conditions in the experiment

	T=0.877 s				T=1.132 s				T=1.240 s			
H/λ	λ/L	$\lambda(m)$	k	$\zeta_a(m)$	λ/L	$\lambda(m)$	k	$\zeta_a(m)$	λ/L	$\lambda(m)$	k	$\zeta_a(m)$
1/50				-				0.0183				0.025
1/30	0.5	1.2	5.236	0.02	0.83	2.0	3.142	0.0261	1.0	2.4	2.618	0.035
1/15				0.033				0.0517				0.0772

Fig.4.12, Fig.4.13 and Fig.4.14 illustrate time histories of wave elevation and corresponding amplitude spectra at P_1, P_2 and P_3. In these three figures, the wave steepness keeps same i.e $H/\lambda = 1/30$ and wave length is varied from $\lambda/L = 0.5$ to $\lambda/L = 1.0$. From the figures, we can see the nonlinearity is not apparent because of small wave steepness. However, compared with P_1 and P_2, nonlinearity at point P_3 is distinguishable. That is because near ship's bow diffracted wave is distinct. Fig.4.15 illustrates time histories of wave elevation and amplitude spectra at these three points in the condition that $\lambda/L = 0.5$, $H/\lambda = 1/15$. Distinct nonlinearity is observed in the amplitude spectra, see wave amplitude with $2\omega_0$ in the spectra.

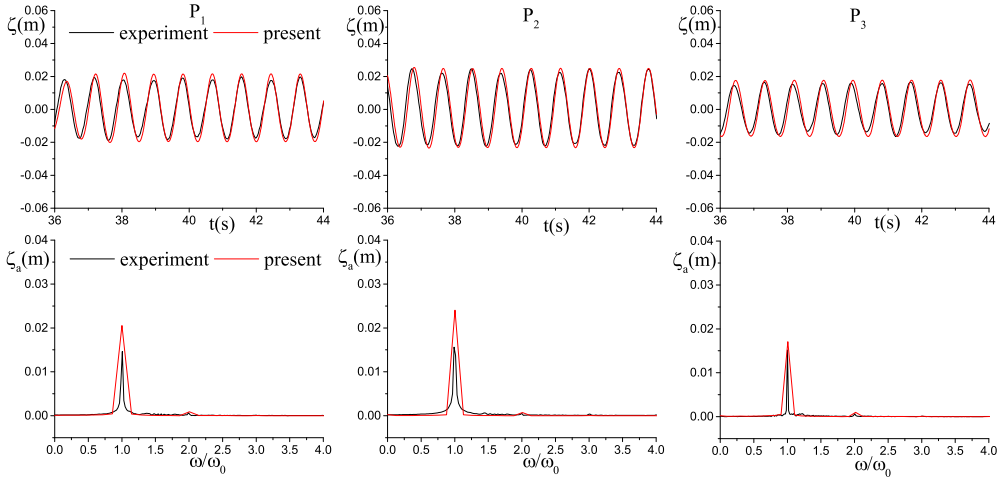

FIGURE 4.12: Time histories and amplitude spectra of wave elevation at three points, $\lambda/L = 0.5$, $H/\lambda = 1/30$.

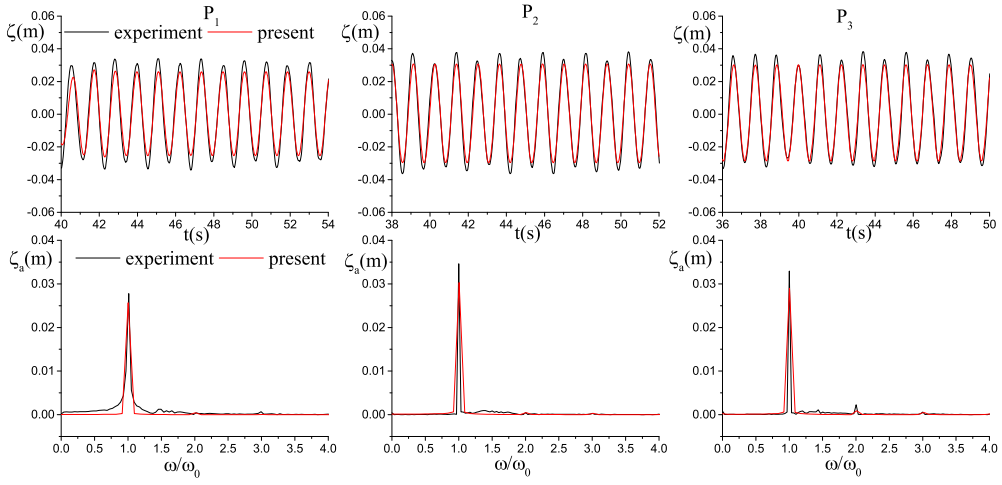

FIGURE 4.13: Time histories and amplitude spectra of wave elevation at three points, $\lambda/L = 0.833$, $H/\lambda = 1/30$.

4.4 Conclusions

In the present chapter, ALE-HOBEM is applied to nonlinear wave diffraction by a non-wall-sided structure. By introducing a prescribed path for each fluid marker on free surface, the trajectory of fluid marker (including intersection on waterline) is determined during the whole computation. In other words, the mesh can be generated automatically in subsequent time. Because the prescribed path is well organized in space, good mesh quality is ensured even though the body has complex geometry. In order to validate the proposed ALE scheme, nonlinear wave diffraction due to three kinds of geometries has been investigated. By comparison, good agreement is observed. Wave diffraction due to circular cylinders with different flares are studied and

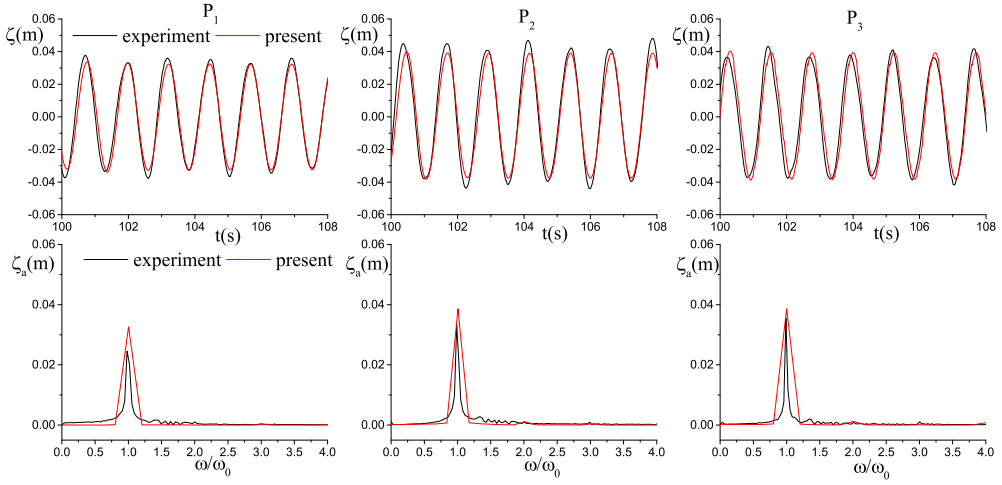

FIGURE 4.14: Time histories and amplitude spectra of wave elevation at three points, $\lambda/L = 1.0$, $H/\lambda = 1/30$.

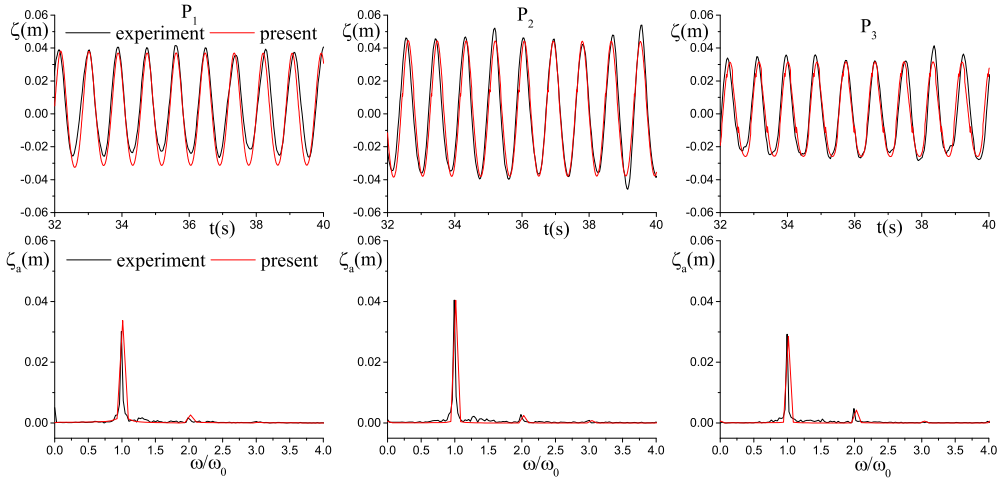

FIGURE 4.15: Time histories and amplitude spectra of wave elevation at three points, $\lambda/L = 0.5$, $H/\lambda = 1/15$.

featured phenomena are observed which are distinct from those in wall-sided cylinders. In the real ship diffraction problem, the diffracted wave is well predicted at region near ship's bow.

Chapter 5

Study on nonlinear wave radiation by a non-wall-sided structure

In the context of fully nonlinear potential flow theory, the existence of flare poses challenge in the computation. Compared to a structure with wall-sided geometry near the waterline, the flare could cause rapid variation in the fluid velocity and pressure and thus good mesh quality is required near the body throughout the computation. In addition, without taking account of the body geometry above the still waterline may lead to a spurious intersection after one time step in the computation, for instance, the intersection may pierce the body surface, which has been described in the diffraction problem. In general, once the body moves with rotational motion, even the body without flare encounters the same problem as described above. What's more, those problems become more apparent when body oscillates with large amplitude, where mesh may be compressed or stretched to a large extent. As a consequence, the mesh near the body with low-quality would affect accuracy and stability of the computation. In this chapter, the wave radiation problem is solved with focus on solving some featured problems when an oscillating body is involved.

5.1 Problem definition

The velocity potential due to a forced oscillation of body is subject to the following BVP,

$$\begin{cases} \nabla^2\phi = 0 \\ \dfrac{\partial \eta}{\partial t} = \dfrac{\partial \phi}{\partial z} - \nabla\phi \cdot \nabla\eta \quad \boldsymbol{x} \in S_f \\ \dfrac{\partial \phi}{\partial t} = -g\eta - \dfrac{1}{2}\nabla\phi \cdot \nabla\phi \quad \boldsymbol{x} \in S_f \\ \dfrac{\partial \phi}{\partial n} = \boldsymbol{V} \cdot \boldsymbol{n} \quad \boldsymbol{x} \in S_b \end{cases} \tag{5.1}$$

where $\boldsymbol{V}$ is the velocity of a point on the body. An appropriate boundary condition is also necessary on a control surface S_C far from the body to avoid unwanted wave reflection. In the present study, an artificial damping layer is used to absorb the wave energy of radiated wave, which is similar with what we used in the diffraction problem.

5.2 Pressure and hydrodynamic forces

In this section, the proposed method for evaluating ϕ_t as introduced in Chapter 3 is applied to study the radiation problem. When a body has only the translational motion, ϕ_t is subject to the following BVP [45]

$$\begin{cases} \nabla^2\phi_t = 0 \\ \dfrac{\partial\phi}{\partial t} = -\dfrac{1}{2}(\nabla\phi)^2 - gz \quad \text{on } S_F \\ \dfrac{\partial\phi_t}{\partial n} = \dot{\boldsymbol{U}}\cdot\boldsymbol{n} - \boldsymbol{U}\cdot\dfrac{\partial\nabla\phi}{\partial n} \quad \text{on } S_B \end{cases} \tag{5.2}$$

As we can see, there is a second derivative term $\partial\nabla\phi/\partial n$ appearing in the body boundary condition. Directly evaluating this term requires much effort in a 3D problem, see Berkvens [19] and Shirakura and Tanizawa [20]. In order to circumvent this difficulty, following Wu and Hu [21] and Zhang [12], we introduce an auxiliary function, $\psi = \phi_t + \boldsymbol{U}\cdot\nabla\phi$. The BVP for ψ can be rewritten as follows:

$$\begin{cases} \nabla^2\psi = 0 \\ \psi = -\dfrac{1}{2}(\nabla\phi)^2 - gz - \boldsymbol{U}\cdot\nabla\phi \quad \text{on } S_F \\ \dfrac{\partial\psi}{\partial n} = \dot{\boldsymbol{U}}\cdot\boldsymbol{n} \quad \text{on } S_B \end{cases} \tag{5.3}$$

Once ψ is obtained, the pressure and resulting hydrodynamic forces and moments can be computed directly from Bernoulli's pressure equation.

5.3 Numerical results and discussions

We consider the radiation problem for a non-wall-sided cylinder shown in Fig.5.1, forcibly oscillating the body in open sea with infinite water depth. Note that the geometry of *case b* in Fig.5.1 is very relevant to practical application e.g. ship's geometry near bulbous bow and to handle this kind of geometry is tricky in the computation as we will see later. In the simulations below, the initial draught of the cylinder is set to $d = 1.5r$ in *case a*. The cylinder is subject to

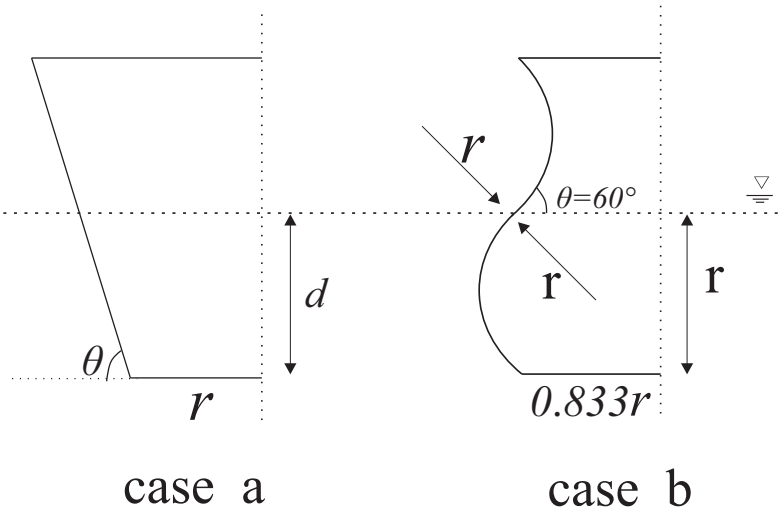

FIGURE 5.1: Dimension of the axisymmetric body with flare; a. body with inclined flare and b. body with curved flare.

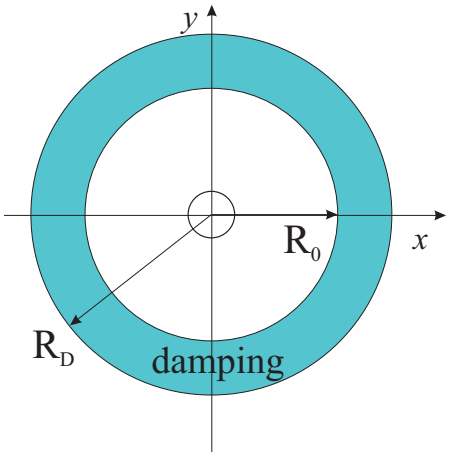

FIGURE 5.2: Sketch of damping layer.

the following harmonic motion in the vertical or horizontal direction.

$$Z = A\sin(\omega t) \quad \text{or} \quad X = A\sin(\omega t) \tag{5.4}$$

The computational domain is truncated by a vertical circular cylinder with radius $R_D = 3\lambda$, where λ is the wave length computed by the linear theory. The length of damping zone is set equal to λ as shown in Fig.5.2.

5.3.1 Convergence study

In the convergence tests, wave radiation around a circular cylinder with $\theta = 80^\circ$ (*case a*) under prescribed heave motion is considered. The wave number is taken as $kr = 2.42$ and the amplitude

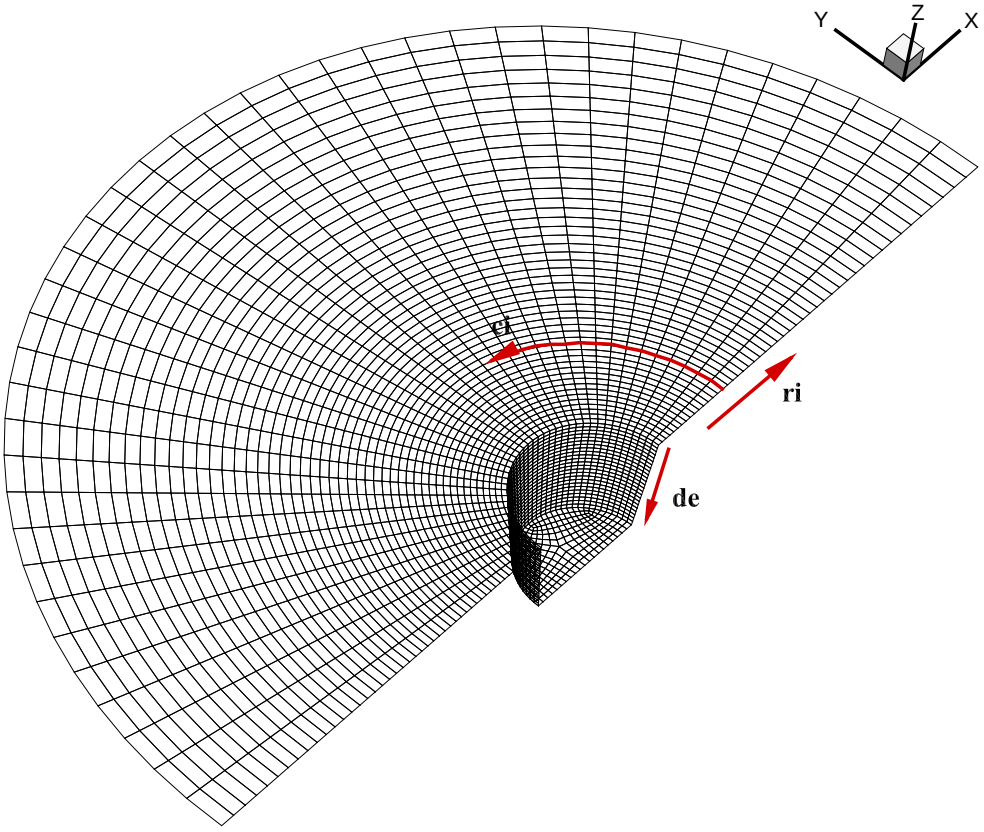

FIGURE 5.3: Sketch of mesh1 used for convergence test. *ri* denotes direction along radius; *ci* direction along the circle and *de* direction along draft. On bottom, unstructured mesh is used.

of motion $A/r = 0.4$. Three different meshes are chosen, as shown in Tab.5.1 and mesh1 is illustrated in Fig.5.3 for reference. On free surface, along radius direction (*ri*) 17 nodes, 20 nodes and 24 nodes per wave length is used in mesh1, mesh2 and mesh3, correspondingly. From Fig.5.4, we can see the results are sensitive to the mesh, especially the force, which is true as expected since higher-order force components is easily affected by mesh. However, the results obtained from mesh2 and mesh3 are identical, which indicates the present computation is convergent in terms of mesh discretization.

Fig.5.5 illustrates results of convergence study from perspective of time step. As we can see, even larger time step is used e.g. $\Delta t = T/60$, there is no noticeable discrepancy on the results,

TABLE 5.1: Details of different meshes, nodes on direction1 × nodes on direction2, or total nodes.

Item	free surface (ri×ci)	side surface (de×ci)	bottom
mesh1	52× 40	18× 40	214
mesh2	60× 56	20× 56	476
mesh3	72× 60	24× 60	827

which proves the present computation is convergent in terms of time discretization. In the following computation, the free surface is discretized by 20 nodes per wave length if not specified and discretization in other direction can be approximated by keeping a proper aspect ratio of the mesh, and $\Delta t = T/80$ is used. Since in the present paper many different geometries are involved, for brevity other results on convergence study are not provided here.

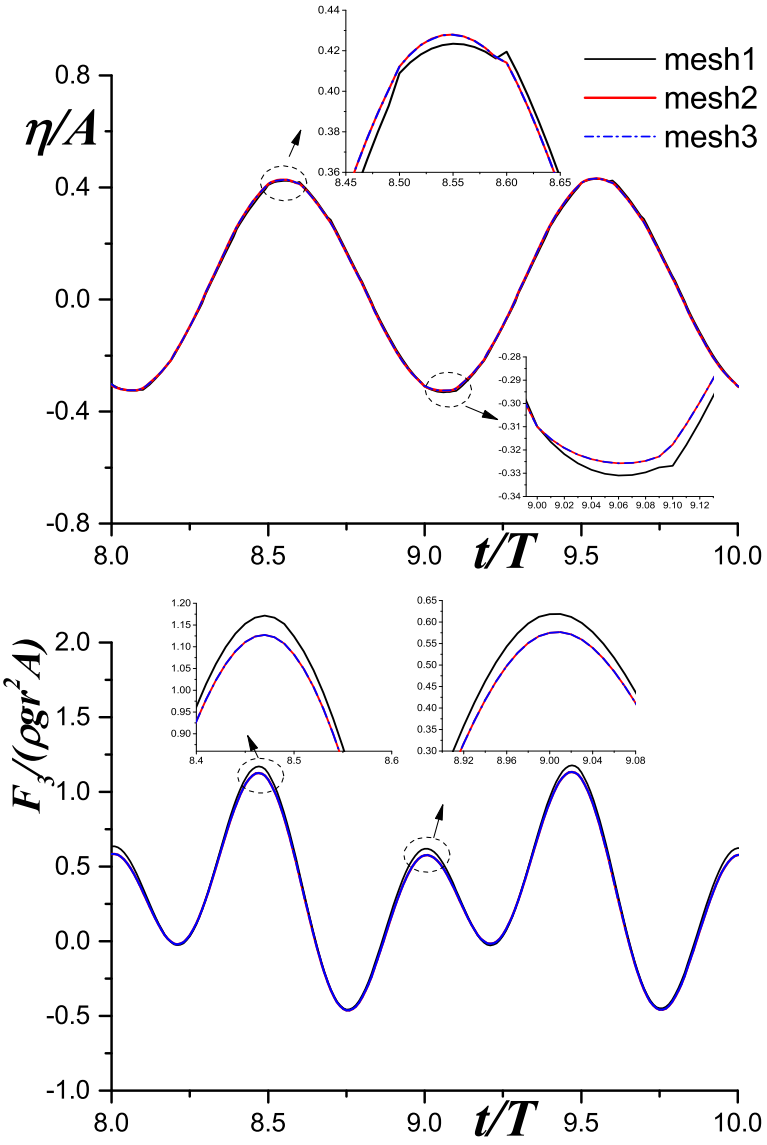

FIGURE 5.4: Study on mesh-dependency of wave runup and vertical force, with $\Delta t = T/100$.

5.3.2 Wave radiation due to heaving oscillation, case a

We first consider a cylinder (*case a*) with flare angle of $\theta = 80°$, which is in heave motion with amplitude of $A = 0.1r$ and $A = 0.4r$ and non-dimensional wave number of $kr = 0.64$ and $kr = 1.95$. The wave runup and the vertical force are calculated and the results are shown in

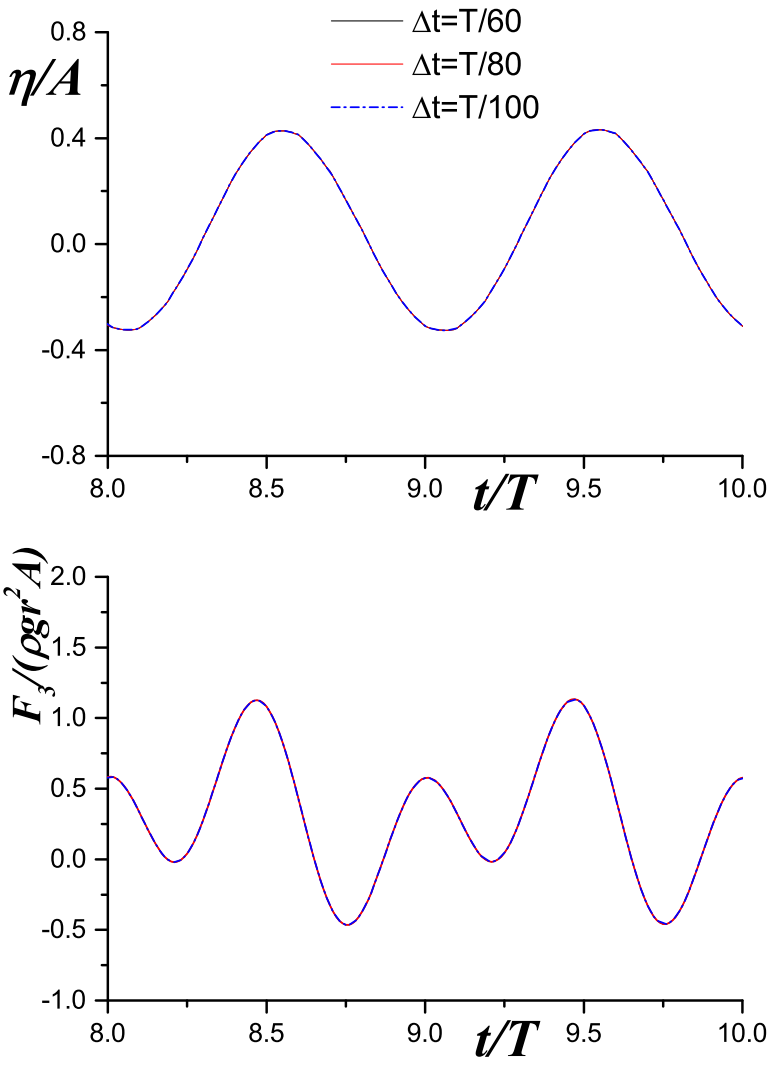

FIGURE 5.5: Study on time-step-dependency of wave runup and vertical force. mesh2 is used in the computation.

Fig.5.6 for $kr = 0.64$ and Fig.5.7 for $kr = 1.95$. In computed results of the vertical force, *BVP* indicates that ϕ_t is evaluated by solving a BVP while *Diff* indicates that ϕ_t is approximated by the three-point central finite difference. We can see that both methods give identical results, which shows validity of solving ϕ_t by the proposed scheme. From the aspect of efficiency, evaluation of ϕ_t by solving a BVP would not increase the computation time, since the coefficient matrix for ϕ_t is exactly the same as that for ϕ. In the present paper, since the validity of the method for computing ϕ_t has been confirmed through comparison of the results by two different methods, hereafter we will show only the results of the hydrodynamic force calculated by solving Eq.(5.3).

We can see also from Fig.5.7 at higher frequency that both wave run-up and hydrodynamic force exhibit nonlinearity with the increasing oscillation amplitude.

In order to validate computed results more, a comparison is made with the results by Wang and

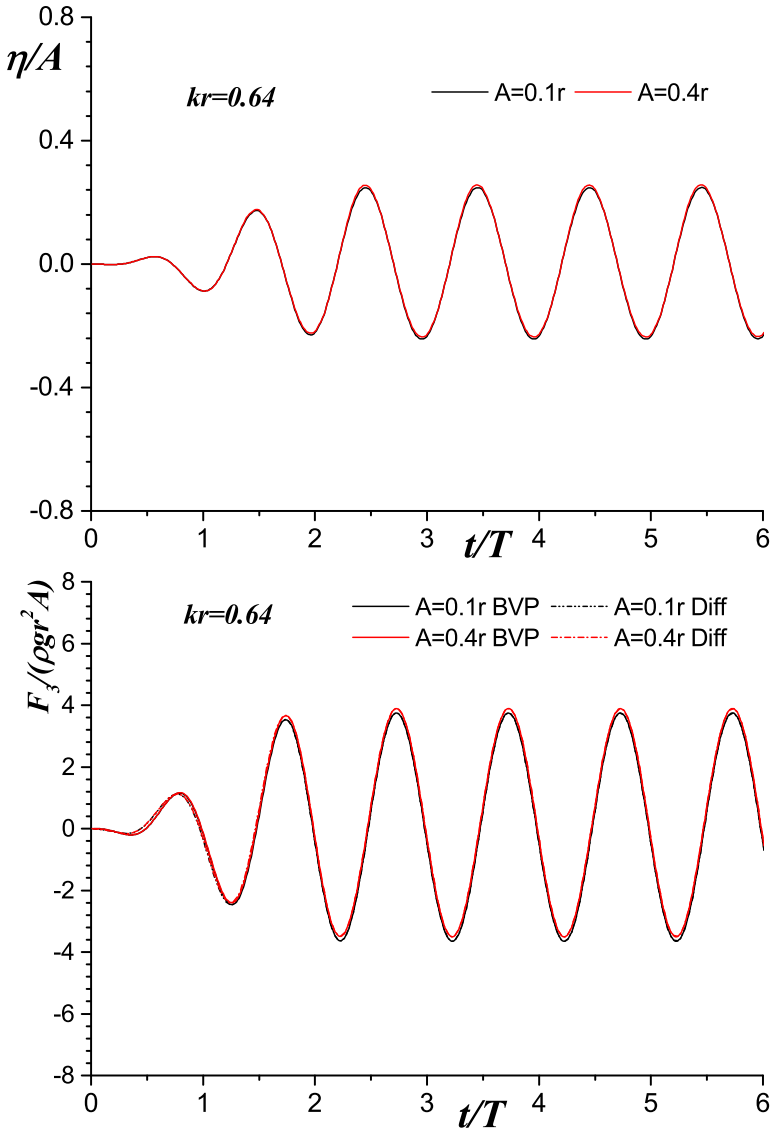

FIGURE 5.6: Time histories of wave runup and vertical force by forced heave oscillation at $Kr = 0.64$.

Wu [56] for the wave elevation on the free surface at $R = 2r$. Computed results are shown for two cases: (1) $kr = 1$ and $A/r = 0.6$ and (2) $kr = 2$ and $A/r = 0.3$. As we can see from Fig.5.8, the present results agree well with those by Wang and Wu [56]. This may indicate that the velocity field is properly solved.

According to Bernoulli's pressure equation, the hydrodynamic force consists of three components, i.e. the component computed from ϕ_t, the component due to the velocity squared, and the static force. In order to validate the present results for the force calculation, comparison is again made with the results by Wang and Wu [56] for each of the component. As we can see from Fig.5.9, the agreement in all three components is good. By looking at the order of each component in the force and the total force, we can see that different force components may cancel out

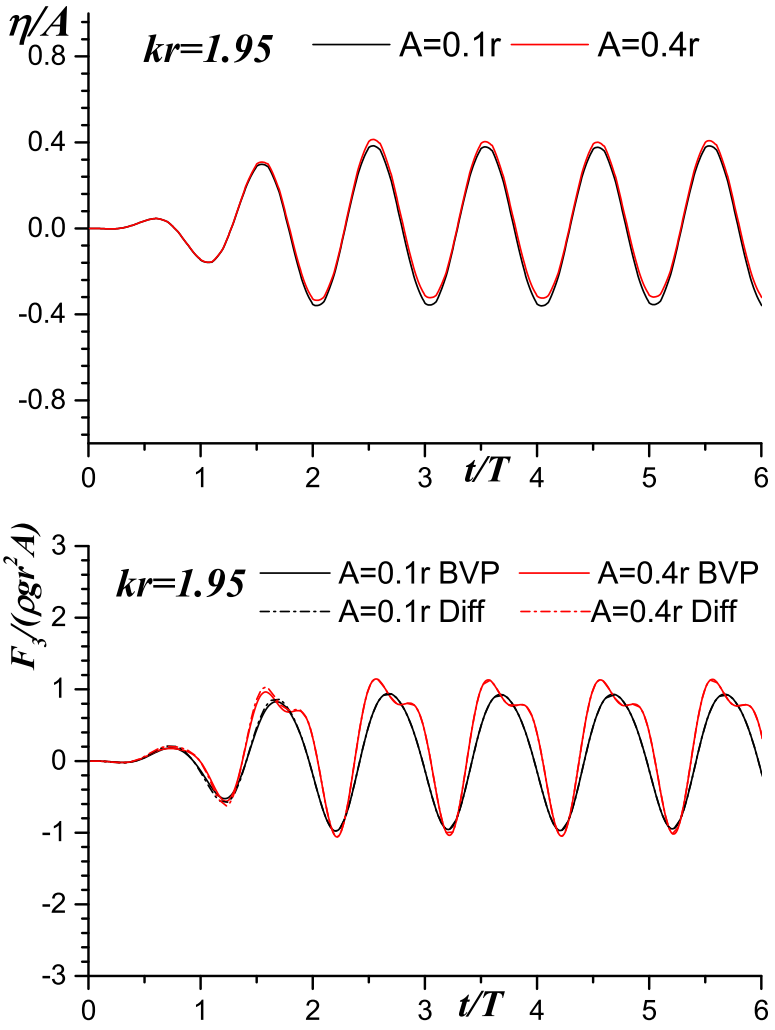

FIGURE 5.7: Time histories of wave runup and vertical force by forced heave oscillation at $Kr = 1.95$.

and as a consequence the total force does not exhibit apparent nonlinearity.

The Fourier analysis on the time history of hydrodynamic forces is carried out. The hydrodynamic force acting in the i-th direction, F_i, was represented by the following Fourier series:

$$\begin{aligned} F_i &= -\rho \iint \left\{ \frac{\partial \phi}{\partial t} + \frac{1}{2}(\nabla\phi)^2 \right\} n_i \, dS \\ &= F_i^{(0)} + \sum_{n=1}^{5} \left\{ a^{(n)} \sin(n\omega t) + b^{(n)} \cos(n\omega t) \right\} \end{aligned} \tag{5.5}$$

The first-order force is expressed in terms of the added mass and the damping coefficient and nondimensionalized as follows:

$$\begin{cases} A_{33} = a^{(1)}/(-A\omega^2)/(\rho r^3) \\ B_{33} = b^{(1)}/(A\omega)/(\rho r^2 \sqrt{gr}) \end{cases} \tag{5.6}$$

The remaining n-th-harmonic components are nondimensionalized in the following form [63]

$$F_i^{(0)} = F_i^{(0)}/(\rho g r^3 (A/r)^2), \quad F_i^{(n)} = F_i^{(n)}/(\rho g r^3 (A/r)^n) \tag{5.7}$$

where $F_i^{(n)} = \sqrt{a^{(n)2} + b^{(n)2}}$ is the amplitude and the phase can be computed from $\delta^{(n)} = \arctan(b^{(n)}/a^{(n)})$.

Fig.5.10 illustrates the added mass and the damping coefficient of a heaving flared body at three different oscillation amplitudes. From comparison with linear results computed by HydroSTAR, the present results agree well with the linear results and no amplitude-dependency is found. This indicates that the first-order hydrodynamic forces are little influenced by the variation of wetted body surface and the nonlinear free-surface condition as far as the heave motion of the present body is concerned.

Fig.5.11 and 5.12 show the 2nd-order and 3rd-order hydrodynamic forces, respectively. Looking at the 2nd-order forces, both amplitude and phase of the harmonic component at two different oscillation amplitudes are the same in the nondimensional value divided by the oscillation amplitude squared. On the other hand, slight difference can be seen in the 2nd-order steady-force component at higher frequencies.

On the other hand, in the 3rd-order hydrodynamic forces, obvious differences depending on the oscillation amplitude can be observed. Particularly the phase is different even in the low frequency range. We should note that the amplitude of the 3rd-order hydrodynamic force for the present body is small as compared to the 2nd-order force and thus the small difference in the amplitude tends to be shown exaggeratedly.

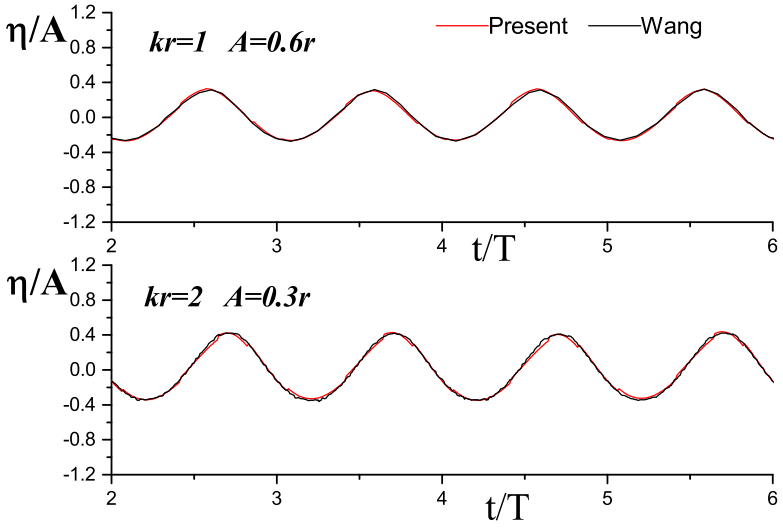

FIGURE 5.8: Time histories of wave elevation at $R = 2r$ on free surface at $kr = 1$, $A = 0.6r$ and $kr = 2$, $A = 0.3r$.

The influence of the flare on wave runups and hydrodynamic forces is studied by changing the angle of the flare at $\theta = 85°$, $\theta = 80°$ and $\theta = 75°$. The computed results are given in Fig.5.13 and Fig.5.14 for $kr = 1$ and $kr = 2$, respectively, but with the same amplitude $A = 0.6r$. These computed results clearly indicate that the larger flare, the larger wave runup and vertical force. Furthermore from comparison between Fig.5.13 and Fig.5.14, we can see that nonlinearity in the vertical force becomes prominent at higher frequencies. However, the time variation in the wave runup looks sinusoidal and the increase in the amplitude seems to be proportional to the increase in the flare angle. Existence of a flare makes the body more *blunt* and thus at the same oscillation amplitude, a body with larger flare could generate waves with larger amplitude. The computed results presented here are consistent with the computation shown by others[56].

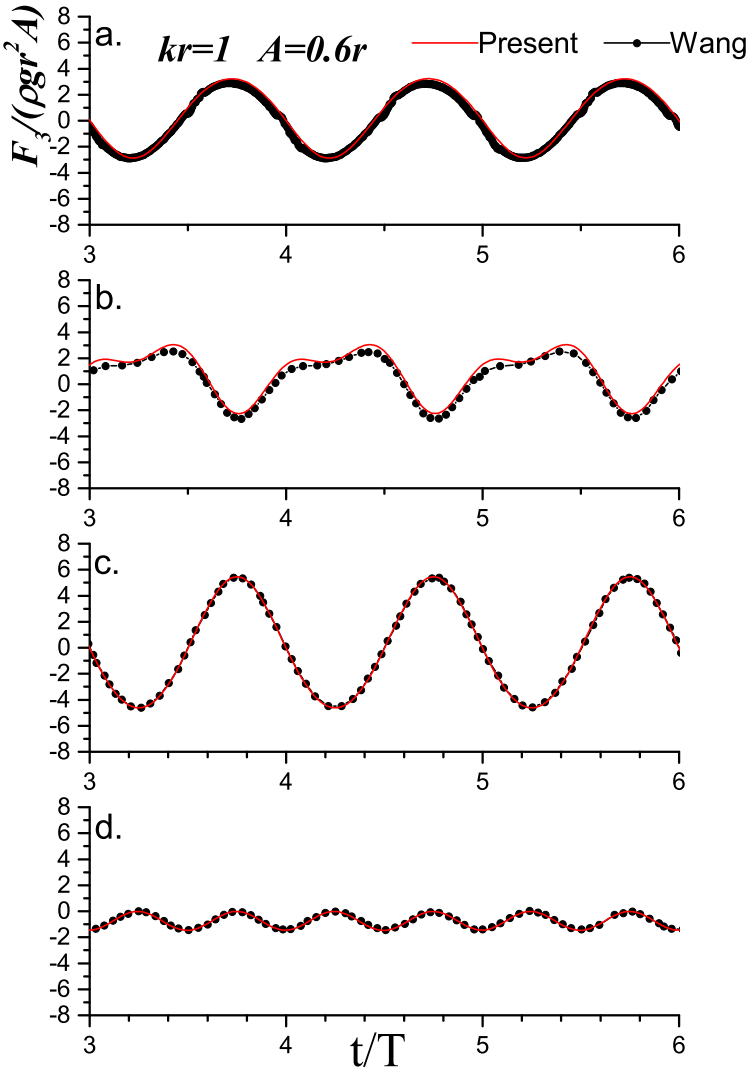

FIGURE 5.9: Time history of non-dimensional force at $kr = 1$ and $A = 0.6r$; a. vertical force in total; b. force component due to ϕ_t; c. force component due to gz; d. force component due to $1/2(\nabla\phi)^2$.

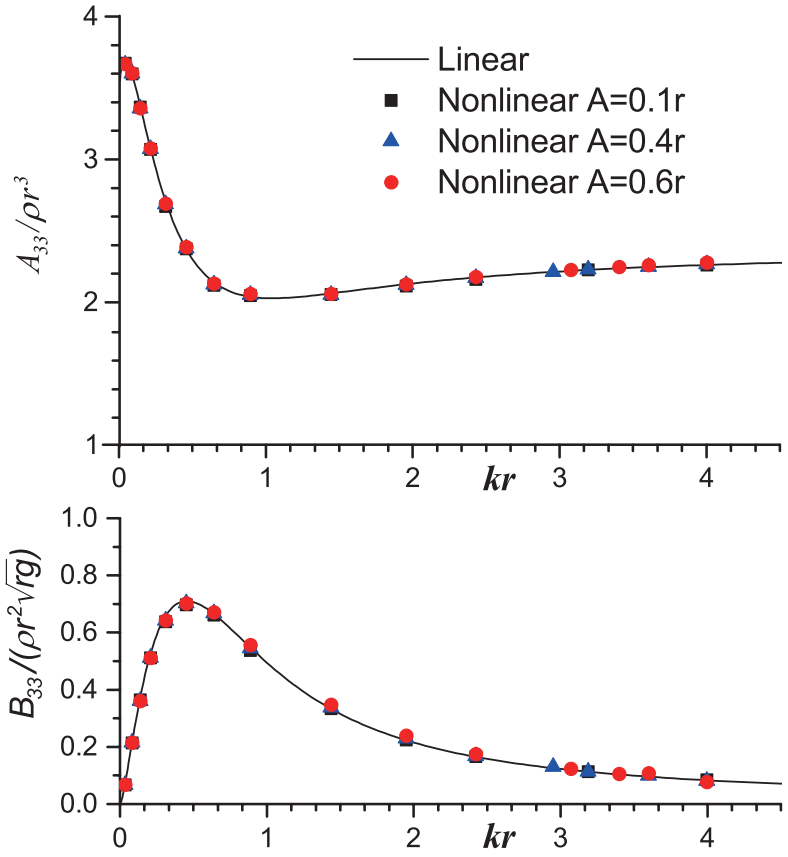

FIGURE 5.10: Added mass and damping coefficient of a heaving cylinder with flare in different amplitudes.

In order to investigate the performance of artificial damping layer, the wave profile along the radial direction of the domain is given in Fig.5.15. As we can see, the wave profile at $t = 11T$ looks identical to that at $t = 10T$, which implies that no wave reflection from the truncated outer boundary is observed. This result also indicates that a smoothing scheme adopted in this paper extracts very little energy from the wave. On the other hand, these spatial wave profiles also exhibit apparent nonlinearity especially near the body surface. Fig.5.16 gives a snapshot of the body-generated wave at $t = 11.45T$ for $kr = 3.6$ and $A = 0.6r$.

5.3.3 Wave radiation due to heaving oscillation, case b

In order to test capacity of the proposed ALE scheme, the radiated wave generated by an axisymmetric body, see *case b* in Fig.5.1, is studied. As we can see, this body near waterline has rapid geometry variation, which indicates fine mesh and smaller time step should be used in the computation, in order to capture small scale wave phenomena as well as rapid variation of velocity field and pressure field. In the present case, the time step is set as $\Delta = T/100$ and smoothing scheme is applied every five steps.

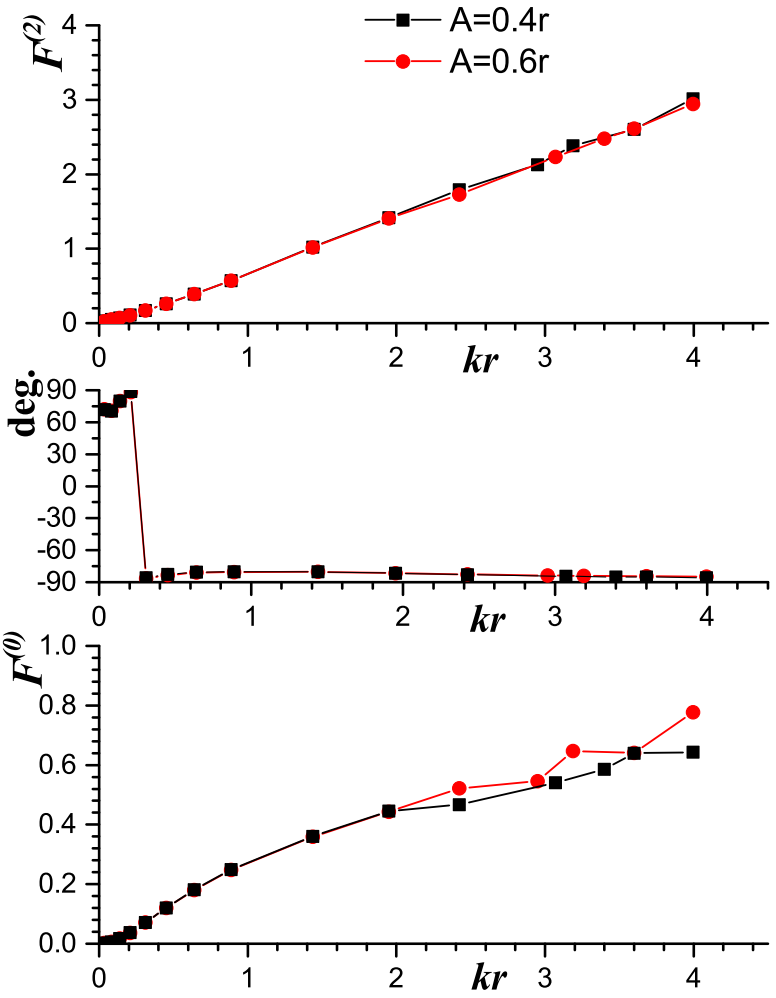

FIGURE 5.11: Non-dimensional amplitude of 2nd-harmonic force as well as phase with $A = 0.4r$ and $A = 0.6r$.

The computed results including time history of wave run up and vertical force are provided with $kr = 1.147$ and $kr = 2.294$. Under wave condition $kr = 1.147$, results are provided with three heaving amplitude i.e. $A/r = 0.1$, $A/r = 0.2$ and $A/r = 0.3$, for comparison. However, since the wave near waterline is very violent in $kr = 2.294$, only two amplitudes are used, i.e. $A/r = 0.1$ and $A/r = 0.2$.

From Fig.5.17 and Fig.5.18, we can see, when increasing amplitude, there is high-frequency oscillation appearing in time series of wave run up, which is due partly to physical cause that the flare serves as a orbit for the intersection and therefore the curved orbit with motion together with effect of nonlinear local wave do contribute to fluctuation in wave run up; and is due partly to numerical error e.g. the so-called *sawtooth* wave. However, the time history of force is smooth with apparent nonlinearity, which indicates the very local nonlinearity affects a little on global force calculation.

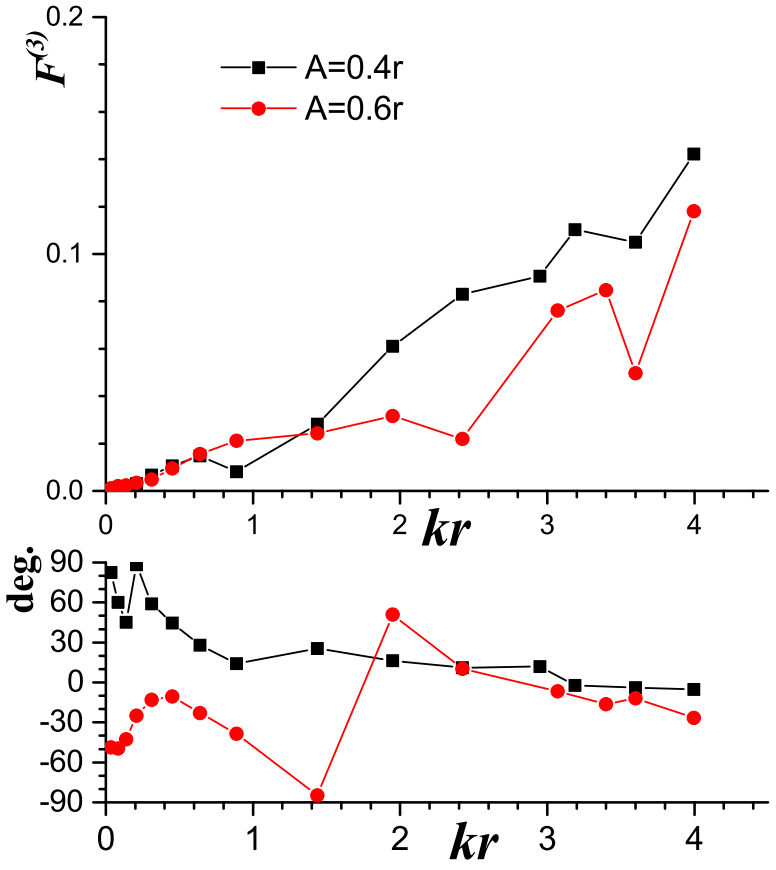

FIGURE 5.12: Non-dimensional amplitude of 3rd-harmonic force as well as phase with $A = 0.4r$ and and $A = 0.6r$.

In order to further investigate the source of nonlinearity in the computed force, according to Bernoulli's equation different force components are separated as shown in Fig. 5.19. From comparison, we can see hydrodynamic force is dominant in the case $kr = 2.294$ while static force plays the leading role in the case $kr = 1.47$, which is consistent with well-known wave-body interaction theory. And also the force component due to ϕ_t is opposite to static force in phase, which is because the leading order of force component due to ϕ_t is proportional to acceleration of the body, see Eq.(5.3) and the static force is proportional to displacement of the body.

5.3.4 Wave radiation due to a surge motion, case a and case b

In this subsection, some of the numerical results in the forced surge motion of a body with flare are shown and the discussion on their features is made. In the computation, two kinds of geometry i.e. *case a* and *case b* as shown in Fig.5.1 are used. Note that in *case a* the flare is defined with $\theta = 75^\circ$.

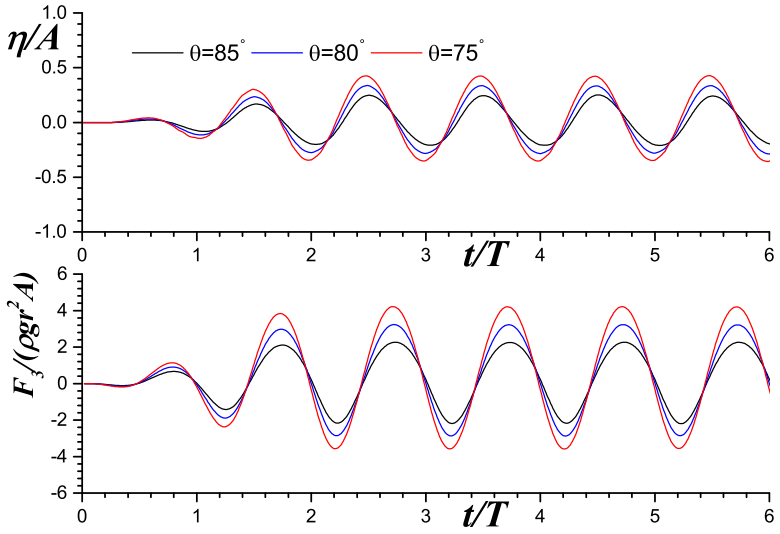

FIGURE 5.13: Flare effect on wave runup and vertical force with $A = 0.6r$ and $kr = 1$.

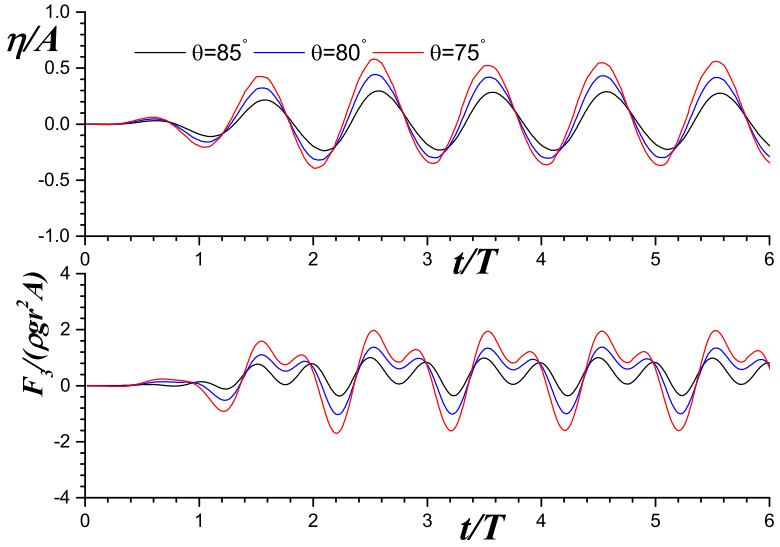

FIGURE 5.14: Flare effect on wave runup and vertical force with $A = 0.6r$ and $kr = 2$.

Fig.5.20 and Fig.5.21 illustrate results of wave run up on frontside and backside and forces in horizontal and vertical direction, which is calculated by *case a* with $kr = 1$ and $kr = 2.42$, respectively. Looking at the wave runup, we can see that the phase in the time variation is almost opposite between front side and back side. In general, because of sinusoidal motion and symmetry of the body, a relation of $f(-x, y, z, t + T/2) = f(x, y, z, t)$ holds, where f can be the pressure or the wave elevation. Substituting this relation into the Fourier-series expansion of the vertical force F_3, one can understand that only $2n\omega$ component exists [64]. From Fig.5.20 and Fig.5.21, it can be seen that the present result for the heave force in the z direction is consistent with this observation.

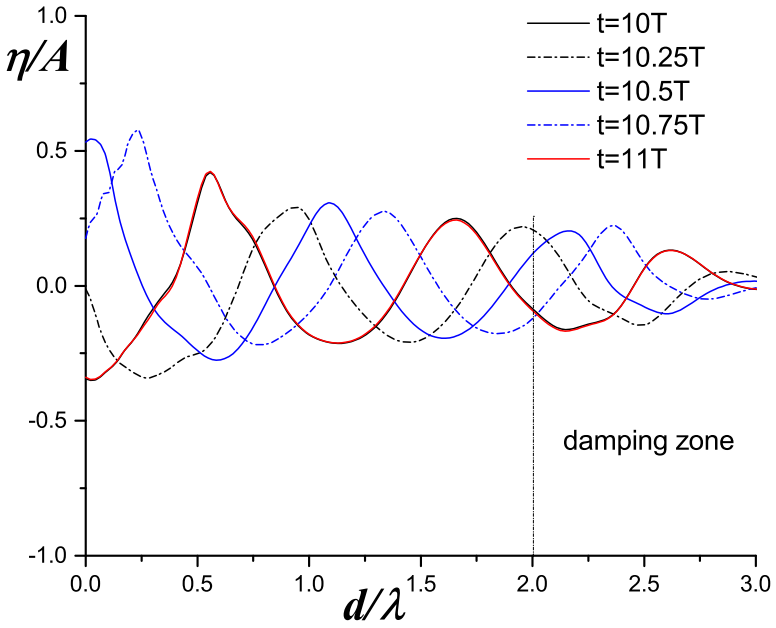

FIGURE 5.15: Wave profile along radial direction of the computational domain (d is distance from body) with $A = 0.6r$, $kr = 2$, and $\theta = 75°$.

Note that since the hydrodynamic force in heave mode is a second-order value and thus it's variation is proportional to A^2 with increasing of amplitude of surging oscillation, which would be clear if we non- dimensionalized this value by Eq.(5.7). Fig.5.22 illustrates the results computed from *case b*.

In the present computation, because of features of ALE scheme, all the nodes as well as the prescribed pathes on free surface move uniformly following the body's surge motion. This strategy enables us to simulate motions with large horizontal displacement by limited computational domain and mesh, for instance, ship's maneuvering test.

5.4 Conclusions

The radiation problem of a 3D non-wall-sided floating body has been studied based on the fully nonlinear potential flow theory, and nonlinearity in the body-generated waves and the hydrodynamic forces on the body has been discussed. In order to solve a nonlinear free-surface problem associated with the flare of a body, ALE-HOBEM is used in the present computation. It is featured in the capability of tracking the exact intersection between the body and the water surface. Furthermore, the mesh on the free surface can be self-adapted to conform to the body motion, which is important when the body oscillates with large amplitude. In the calculation of hydrodynamic forces, a boundary-value problem for an auxiliary function related to the temporal derivative of the velocity potential ϕ_t was solved, and the accuracy and efficiency of the method

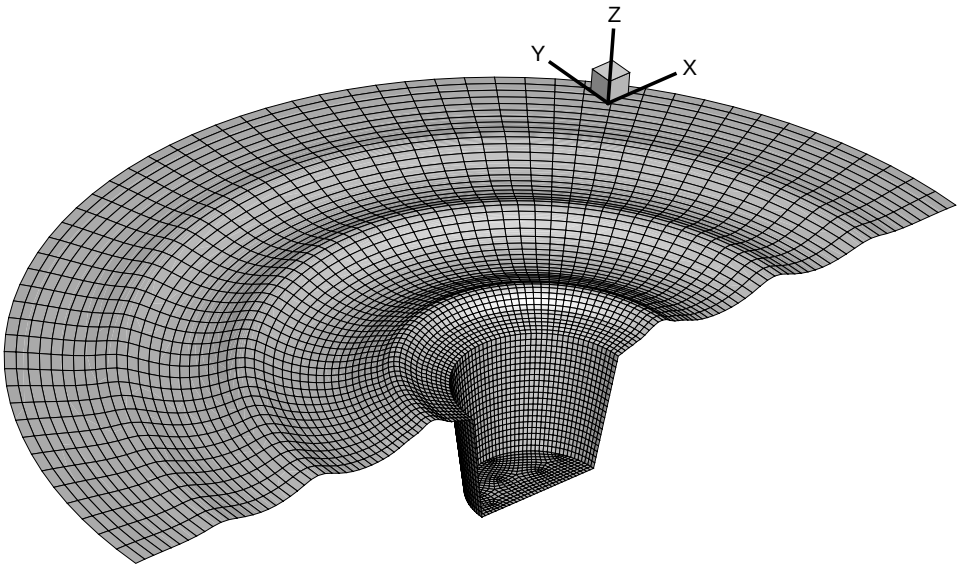

FIGURE 5.16: Sketch of wave radiation by a heaving cylinder with flare, at $t = 11.45T$ with $kr = 3.6$ and $A = 0.6r$.

have been demonstrated. From computed results, we confirmed that the flare of a body could increase the degree of nonlinearity in the hydrodynamic force and the wave runup. Through various validation and confirmation for the waves and hydrodynamic forces induced by the forced oscillation of flared bodies, the calculation method presented in this thesis was found to be accurate enough and flexible and hence may be applicable to more complicated problems, e.g. interaction of nonlinear waves with a freely floating body.

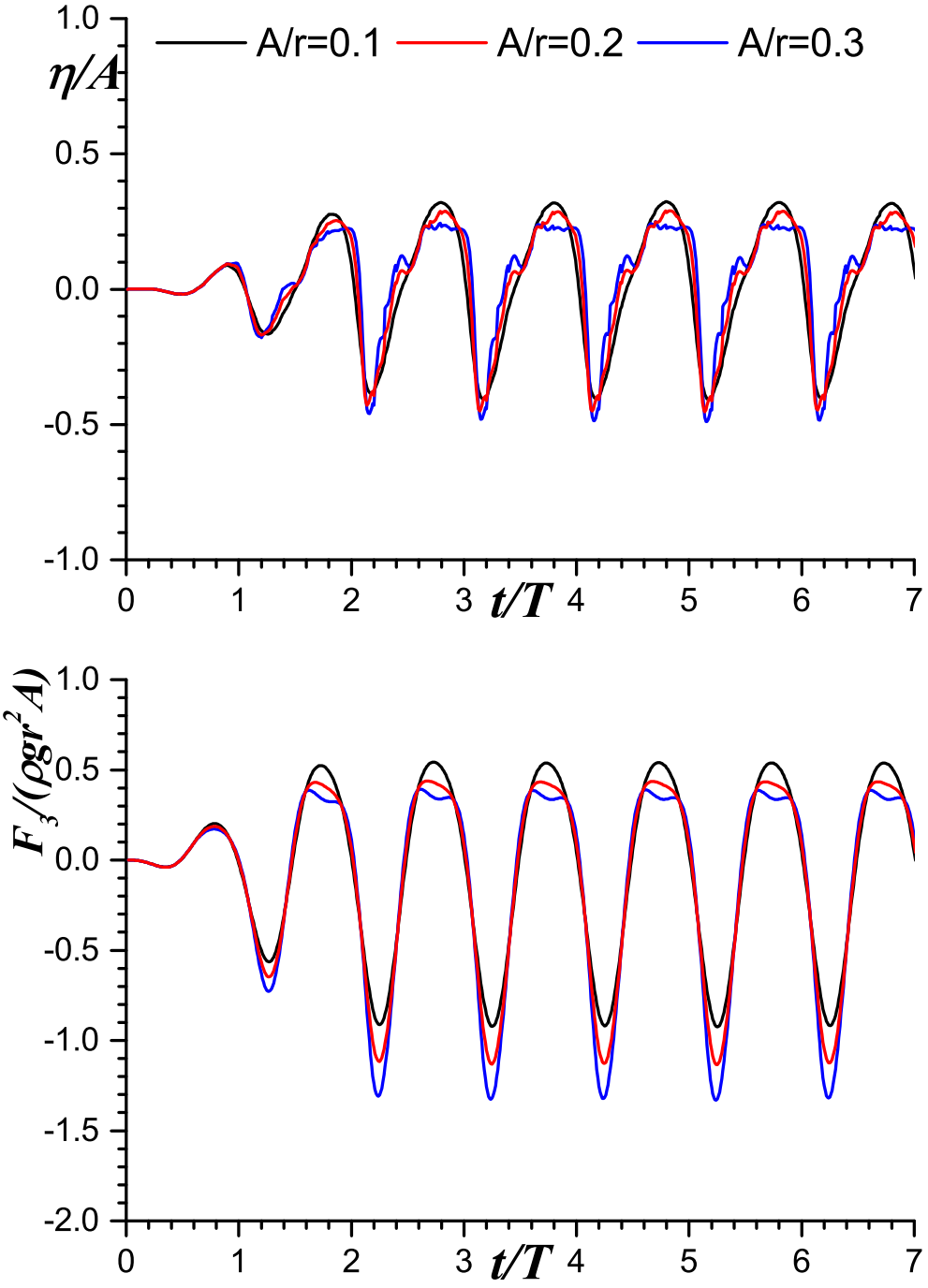

FIGURE 5.17: Time history of wave run up and vertical force with kr = 1.147.

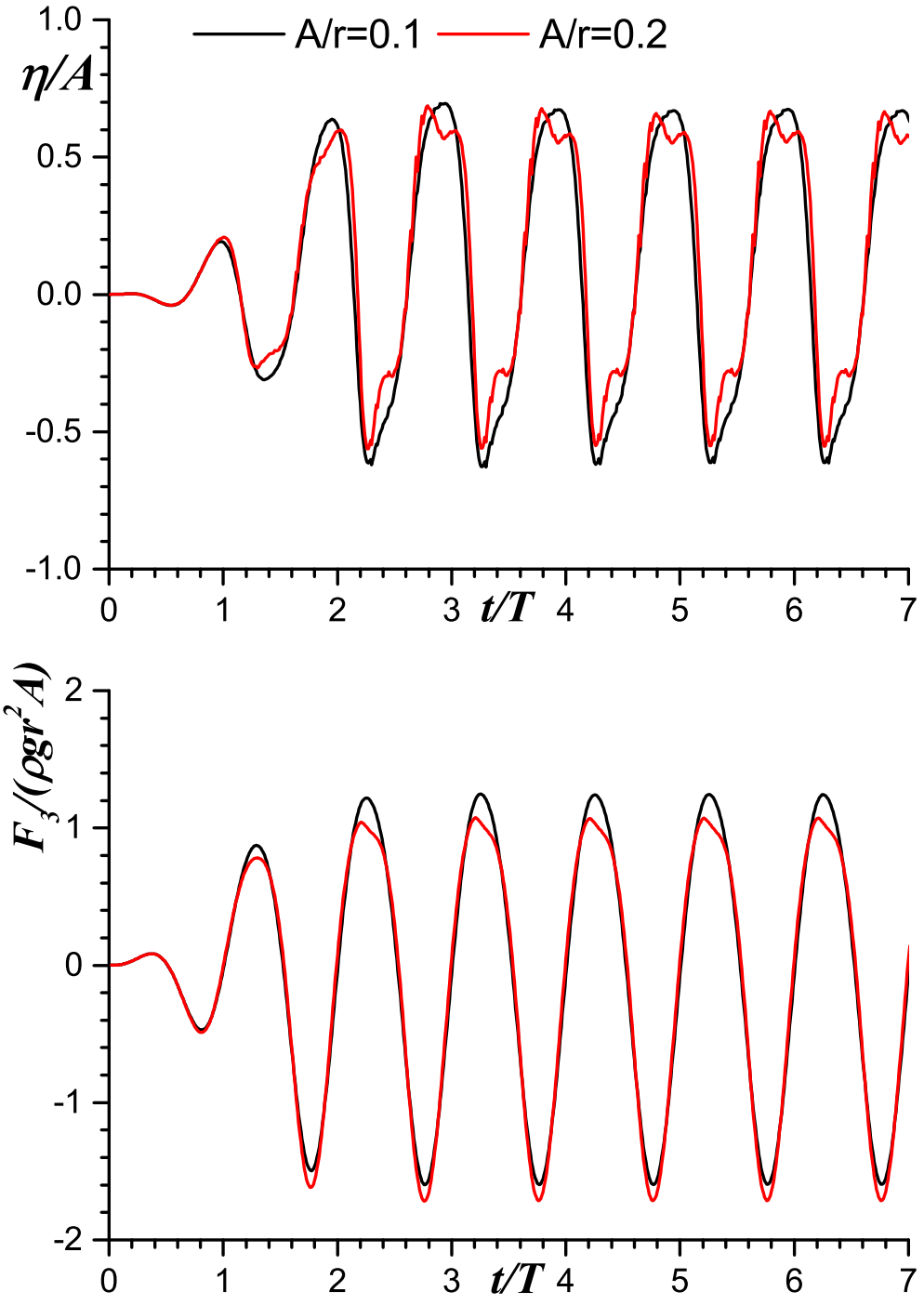

FIGURE 5.18: Time history of wave run up and vertical force with $kr = 2.294$.

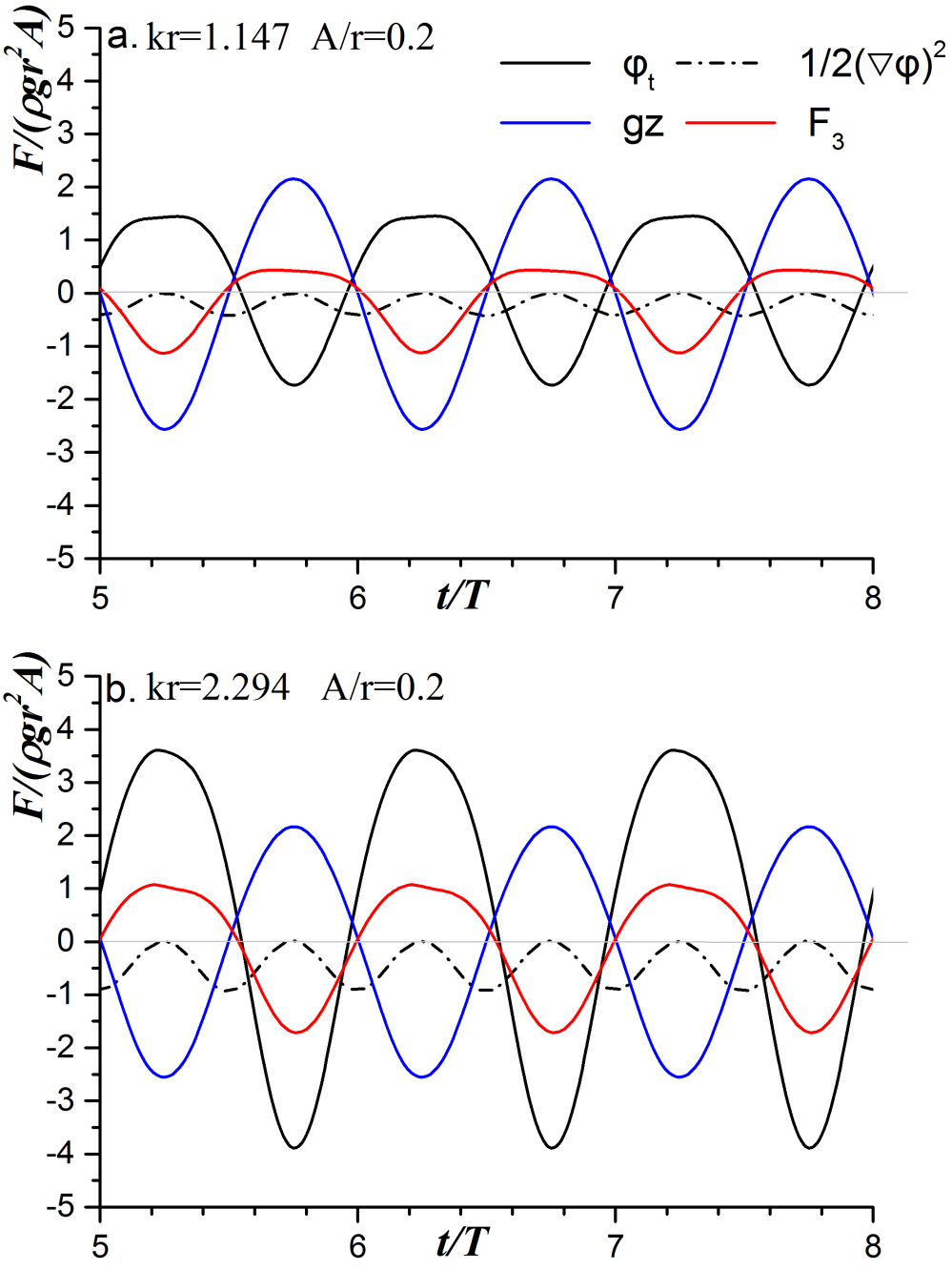

FIGURE 5.19: Comparison of different force components; a. kr = 1.47 and b. kr = 2.294.

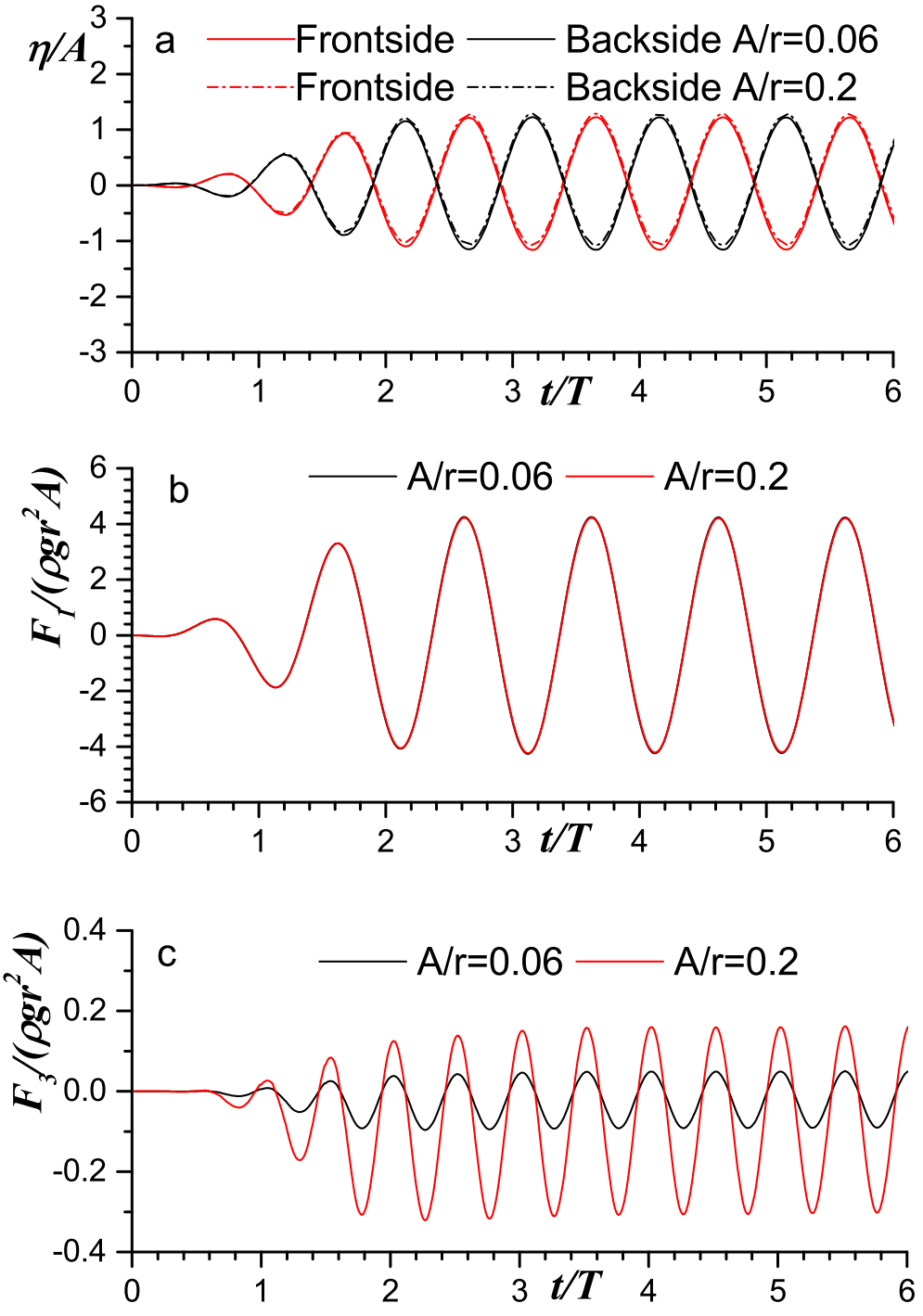

FIGURE 5.20: Time history of wave elevations and forces on a surging body (case a) with $\theta = 75°$ and $kr = 1$. a. wave runup; b. horizontal force; c. vertical force.

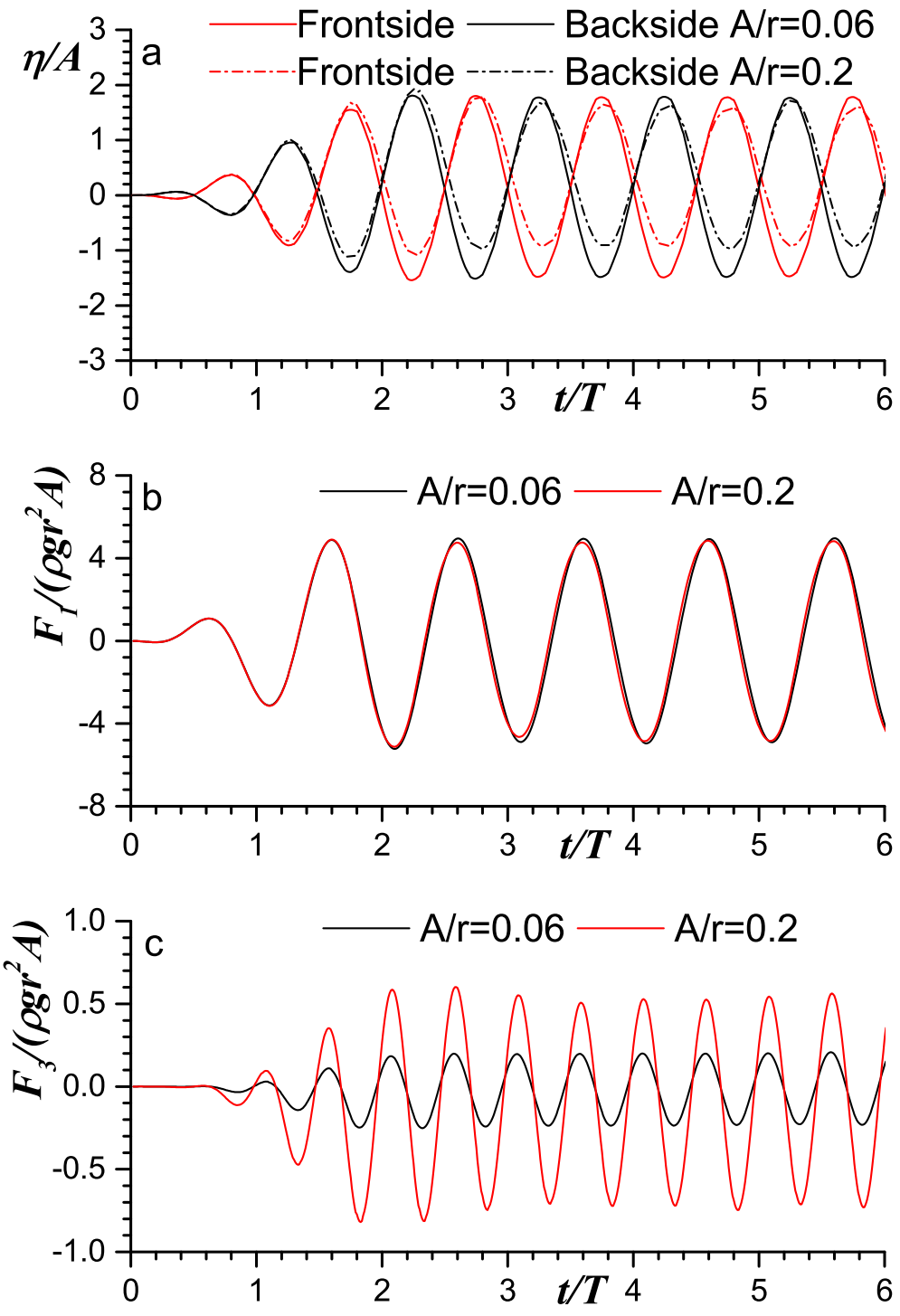

FIGURE 5.21: Time history of wave elevations and forces on a surging body (case a) with $\theta = 75°$ and $kr = 2.42$. a. wave runup; b. horizontal force; c. vertical force.

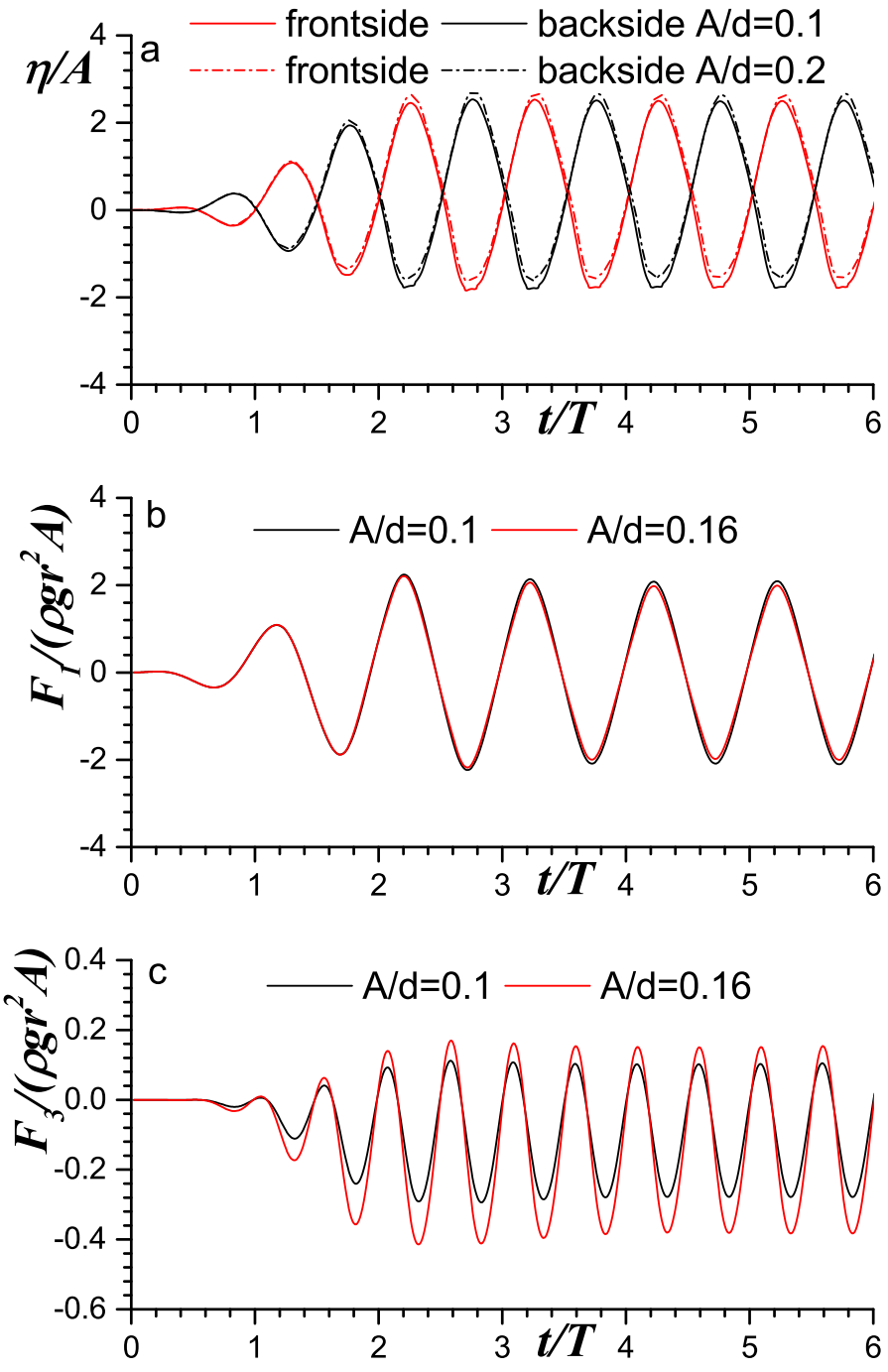

FIGURE 5.22: Time history of wave elevations and forces on a surging body (case b) with kr = 2.04. a. wave run up; b. horizontal force; c. vertical force.

Chapter 6

Wave interaction with a freely floating body

This chapter introduces an attempt to apply ALE-HOBEM to study nonlinear waves interaction with a freely floating body. At present (when the author is writing the dissertation), there is some problem in the code. And thus only preliminary results are provided here, which includes motion response in heave mode, the second-order and third-order motion resonance of heave motion.

6.1 Problem definition

In the framework of potential flow theory, a velocity potential ϕ can therefore be introduced, which satisfies the Laplace equation in the fluid domain and proper boundary conditions on free surface (S_f), body surface (S_b) and truncated surface (S_c) at far field.

$$\begin{cases} \nabla^2\phi = 0 \\ \dfrac{\partial\phi}{\partial n} = \boldsymbol{V}\cdot\boldsymbol{n} \quad \boldsymbol{x}\in S_b \\ \dfrac{\partial\eta}{\partial t} + \nabla\phi\cdot\nabla\eta = \dfrac{\partial\phi}{\partial z} \quad \boldsymbol{x}\in S_f \\ \dfrac{\partial\phi}{\partial t} + \dfrac{1}{2}\nabla\phi\cdot\nabla\phi + g\eta = 0 \quad \boldsymbol{x}\in S_f \end{cases} \tag{6.1}$$

where $\boldsymbol{n} = (n_1, n_2, n_3)$ is the unit normal vector (out of the fluid) and $\boldsymbol{V} = \boldsymbol{U} + \boldsymbol{\omega}\times\boldsymbol{r}^b$ is the velocity of a point on body surface relative to the $Oxyz$ frame with $\boldsymbol{U}$ being translational velocity and $\boldsymbol{\omega}$ rotational velocity. η is free surface elevation. On control surface S_c an proper absorbing boundary is imposed.

6.2 Decomposition of velocity potential

As used in the diffraction problem, the velocity potential decomposition scheme is adopted in the present research. Since the incident wave is explicitly represented by fifth-order Stokes wave [57], the total velocity potential ϕ can therefore be decomposed as, $\phi = \phi^I + \phi^D$, where ϕ^I denotes velocity potential of incident wave and ϕ^D governs the remaining disturbed wave field i.e. diffracted and radiated wave fields. Substituting this decomposition into Eq.(6.1) yields

$$\begin{cases} \nabla^2\phi^D = 0 \\ \dfrac{\partial\phi^D}{\partial n} = \boldsymbol{V}\cdot\boldsymbol{n} - \dfrac{\partial\phi^I}{\partial n} \quad \boldsymbol{x}\in S_b \\ \dfrac{\partial\eta}{\partial t} = \dfrac{\partial(\phi^I+\phi^D)}{\partial z} - \nabla(\phi^I+\phi^D)\cdot\nabla\eta \quad \boldsymbol{x}\in S_f \\ \dfrac{\partial\phi^D}{\partial t} = -\dfrac{1}{2}\nabla(\phi^I+\phi^D)\cdot\nabla(\phi^I+\phi^D) - g\eta - \dfrac{\partial\phi^I}{\partial t} \quad \boldsymbol{x}\in S_f \end{cases} \tag{6.2}$$

Note that in the present fully nonlinear computation, the diffracted wave and radiated wave governed by ϕ^D can not be further explicitly split as what is usually done in linear theory. Writing the free surface conditions into ALE type, yields

$$\begin{cases} \nabla^2\phi^D = 0 \\ \dfrac{\delta\boldsymbol{x}}{\delta t} = \dfrac{\phi_n - V(\boldsymbol{x}')_n}{l_n}\boldsymbol{l} + \boldsymbol{V}(\boldsymbol{x}') \\ \dfrac{\delta\phi^D}{\delta t} = -\dfrac{1}{2}\nabla(\phi)\cdot\nabla(\phi) - g\eta - \dfrac{\partial\phi^I}{\partial t} + \dfrac{\delta\boldsymbol{x}}{\delta t}\cdot\nabla\phi^D - \mu\phi^D \\ \dfrac{\partial\phi^D}{\partial n} = \boldsymbol{V}\cdot\boldsymbol{n} - \dfrac{\partial\phi^I}{\partial n} \end{cases} \tag{6.3}$$

where $\boldsymbol{x}$ and $\boldsymbol{x}'$ satisfy a relation described by Eq.(3.18).

6.3 Hydrodynamic forces and motion equations

Note that, here we only consider hydrodynamic force and motion equation in heave mode to highlight some features of nonlinear wave interaction with a freely floating structure. In order to obtain hydrodynamic force exerting on the body, one need firstly to consider solution of $\partial\phi/\partial t$ appearing in Bernoulli's equation, which is subject to the following BVP as described in Chapter 3.

$$\begin{cases} \nabla^2\phi_t = 0 \\ \dfrac{\partial\phi}{\partial t} = -\dfrac{1}{2}(\nabla\phi)^2 - gz \quad \text{on } S_F \\ \dfrac{\partial\phi_t}{\partial n} = \dot{\boldsymbol{U}}\cdot\boldsymbol{n} - \boldsymbol{U}\cdot\dfrac{\partial\nabla\phi}{\partial n} \quad \text{on } S_B \end{cases} \tag{6.4}$$

where in Eq.(6.4) the rotational motion is omitted. And note that here ϕ is the total velocity potential including incident wave and disturbed wave.

In order to decouple the problem, the component of hydrodynamic force, which is proportional to body's acceleration, is extracted from the total force. And thus ϕ_t is decomposed into two parts

$$\phi_t = \psi_{acc} + \psi_{oth} \tag{6.5}$$

where ψ_{acc} is the induced potential due to acceleration and ψ_{oth} is the other remaining part. Those two are subject to the following BVPs, respectively,

$$\begin{cases} \nabla^2 \psi_{acc} = 0 \\ \psi_{acc} = 0 \quad S_f \\ \dfrac{\partial \psi_{acc}}{\partial n} = \dot{\boldsymbol{U}} \cdot \boldsymbol{n} \quad S_b \end{cases} \tag{6.6}$$

$$\begin{cases} \nabla^2 \psi_{oth} = 0 \\ \psi_{oth} = -\dfrac{1}{2}(\nabla \phi)^2 - gz \quad S_f \\ \dfrac{\partial \psi_{oth}}{\partial n} = -\boldsymbol{U} \cdot \dfrac{\partial \nabla \phi}{\partial n} \quad S_b \end{cases} \tag{6.7}$$

Suppose ψ_{acc} is linearly dependent on body's acceleration,

$$\psi_{acc} = \dot{U}_1 \varphi_1 + \dot{U}_2 \varphi_2 + \dot{U}_3 \varphi_3 \tag{6.8}$$

where $(U_1, U_2, U_3) = \boldsymbol{U}$. Substituting this expression into Eq.(6.6) yields

$$\begin{cases} \nabla^2 \varphi_i = 0 \\ \varphi_i = 0 \quad \textit{on free surface} \\ \dfrac{\partial \varphi_i}{\partial n} = n_i \quad \textit{on body surface} \end{cases} \tag{6.9}$$

where $(n_1, n_2, n_3) = \boldsymbol{n}$. And thus the hydrodynamic force proportional to body's acceleration can be written as follows

$$F_{ij}^{acc} = -\rho \dot{U}_i \iint \varphi_i n_j ds \tag{6.10}$$

and therefore $a_{ij} = -\rho \iint \varphi_i n_j ds$ serves as added mass and can be evaluated simultaneously. After the derivation, one may suspect why Eq.(6.6), Eq.(6.8), Eq.(6.9) and Eq.(6.10) governs force related to body's acceleration.

In terms of ψ_{oth}, to avoid evaluating second derivatives, an auxiliary function is introduced as follows,

$$\psi'_{oth} = \psi_{oth} + \boldsymbol{U} \cdot \nabla\phi \tag{6.11}$$

Rewriting Eq(6.7) yields

$$\begin{cases} \nabla^2\psi'_{oth} = 0 \\ \psi'_{oth} = -\frac{1}{2}(\nabla\phi)^2 - gz + \boldsymbol{U} \cdot \nabla\phi \quad S_f \\ \frac{\partial\psi'_{oth}}{\partial n} = 0 \quad S_b \end{cases} \tag{6.12}$$

In comparison to Eq(6.7), there is no need to evaluate second derivative in Eq(6.12). And thus the corresponding force can be written as follows

$$F_i^{oth} = -\rho \iint (\psi'_{oth} - \boldsymbol{U} \cdot \nabla\phi) n_i ds \tag{6.13}$$

According to Bernoulli's equation, the force exerting on the body can be expressed as follows

$$F_i = \sum_{j=1}^{3} F_{ji}^{acc} + F_i^{oth} - \rho \iint (\frac{1}{2}(\nabla\phi)^2 + gz) n_i ds \tag{6.14}$$

Following Newton's second law, the motion equation in heave mode can be expressed as follows

$$m\frac{dU_3}{dt} = F_3 - mg \tag{6.15}$$

Substituting Eq.(6.14) into Eq.(6.15) and moving the added mass into left-hand side, yields

$$(m + a_{33})\frac{dU_3}{dt} = F_3^{oth} - mg - \rho \iint (\frac{1}{2}(\nabla\phi)^2 + gz) n_3 ds \tag{6.16}$$

Eq.(6.16) shows that nonlinear dependence of fluid body motion is decoupled, since the right-hand force = F_3^{oth} is only related to velocity field of the fluid, see Eq.(6.12) and the added mass on left-hand side is only related to geometry of the enclosed surface of the domain, see Eq.(6.9). In addition, this method can also give pressure distribution due to a directly evaluation of hydrodynamic force.

6.4 Numerical results and discussions

In the computation, an axisymmetric body as shown in Fig.6.1 are used with $\theta = 75°$. The incident wave is represented by the fifth-order Stokes wave as mentioned above, in witch A

denotes wave amplitude, λ wave length and k wave number.

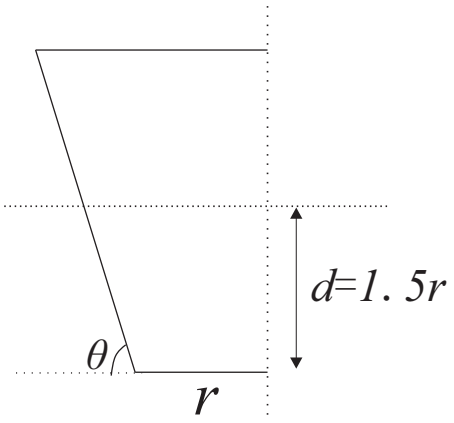

FIGURE 6.1: Dimension of the floating cylinder with flare.

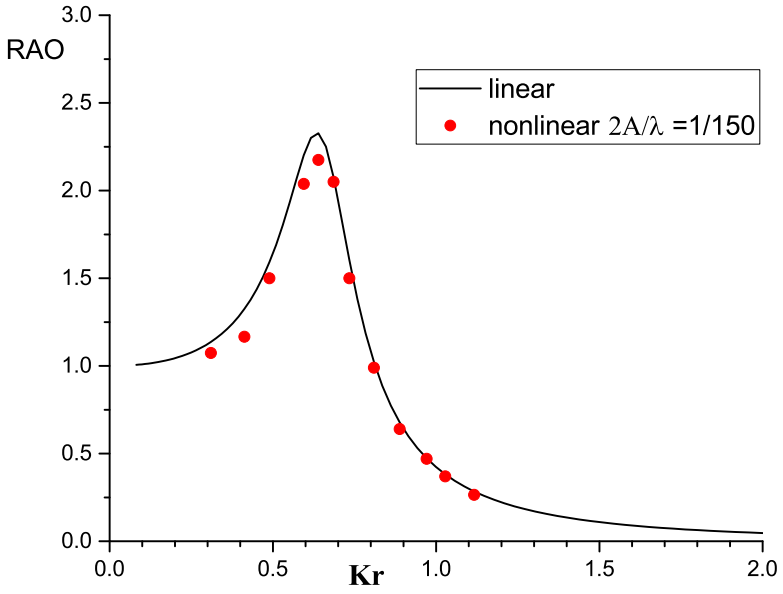

FIGURE 6.2: Response Amplitude Operator (RAO) in heave mode.

Fig.6.2 illustrates RAO of motion response evaluated by HydroSTAR and the present fully non-linear computation. In the most linear case ($2A/\lambda = 1/150$), ALE-HOBEM should provide with identical results to the linear solver HydroSTAR. Since in reality 3DOF motion equations (heave-pitch-surge) are solved, the incorrect motion response in pitch mode would affect heave motion to some extent by means of coupling effect. This may explain the discrepancy in the peak of motion response.

In order to study non-linear effect, the induced wave loads and motion are calculated with increasing wave steepness at $kr = 0.888$. From Fig.6.3 and Fig.6.4, the high-order harmonic components are observed both in force and motion. In addition, there is also noticeable discrepancy in first-harmonic component with a increasing wave steepness.

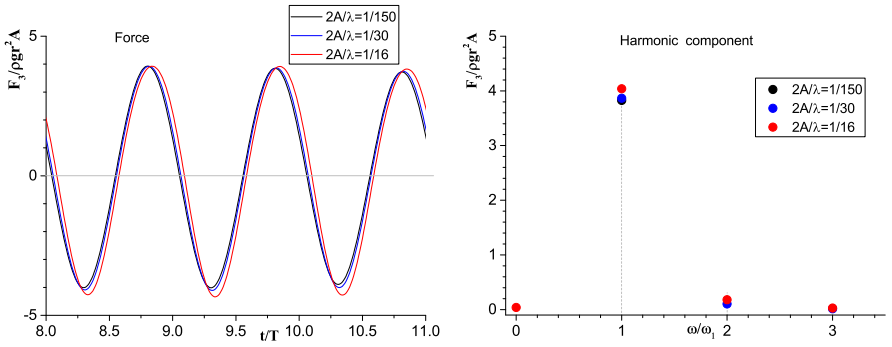

FIGURE 6.3: Time history of non-dimensional vertical force as well as harmonic components of the force with $kr = 0.888$.

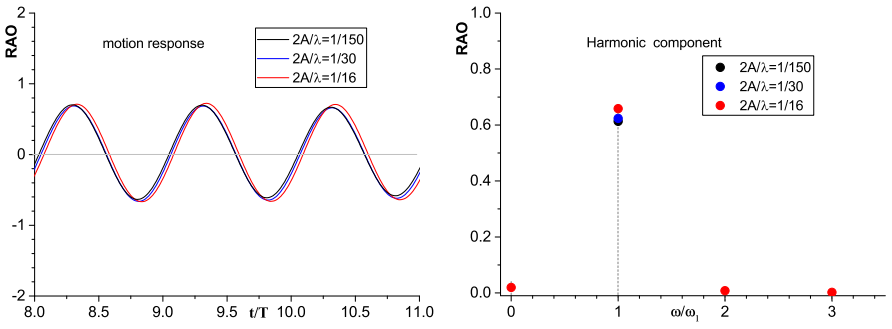

FIGURE 6.4: Time history of non-dimensional heave motion as well as its harmonic components with $kr = 0.888$.

Comparatively speaking, the magnitude of high-order harmonic force is small as we can see from Fig.6.3, and one may suspect whether those small values make difference in practical application. Actually, these higher-harmonic forces may cause highly intense nonlinear structural behaviours called *springing* (at double frequency) and *ringing* (at triple), which were first observed in a model test of the Hutton platform which was operated in the UK North Sea from 1984 to 2001 [65]. The second-order excitation at the double frequency dominates for *springing*, while the higher-order (3rd- and 4th-order) frequencies trigger the *ringing* of gravity-based platforms and tension leg platforms, which is a transient elastic response [66][67][68].

In the present research, the *springing* and *ringing* phenomena are simulated. For a given incident wave with circular frequency ω, in order to trigger the *springing* or *ringing* phenomena, the natural frequency of the body ω_n is designed such that $\omega_n = 2\omega$ for the *springing* or $\omega_n = 3\omega$ for the *ringing*. That indicates the body is in resonance with the excitation of force with double or triple frequency. In terms of reconstruction of body's natural frequency, considering the added mass and damping coefficient of the body at ω, ω_n can be redesigned by changing stiffness of the motion equation.

In the research, the incident wave is selected such that $\omega\sqrt{g/r} = 1.4$, and three waves with

different steepness are used for comparison i.e. $2A/\lambda = 1/50$, $2A/\lambda = 1/30$ and $2A/\lambda = 1/16$, respectively. As shown in Fig.6.5 and Fig.6.6, the *springing* and *ringing* are reproduced in the

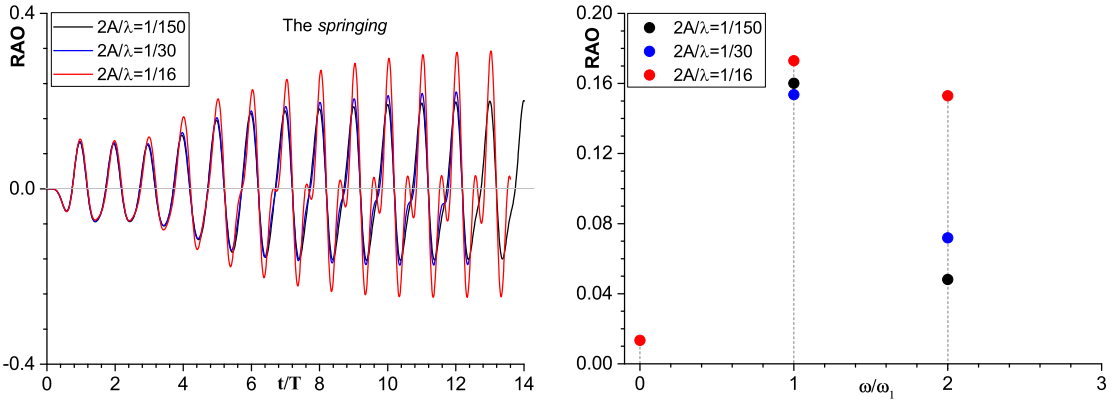

FIGURE 6.5: Time history of non-dimensional heave motion as well as its harmonic components when the *springing* occurs.

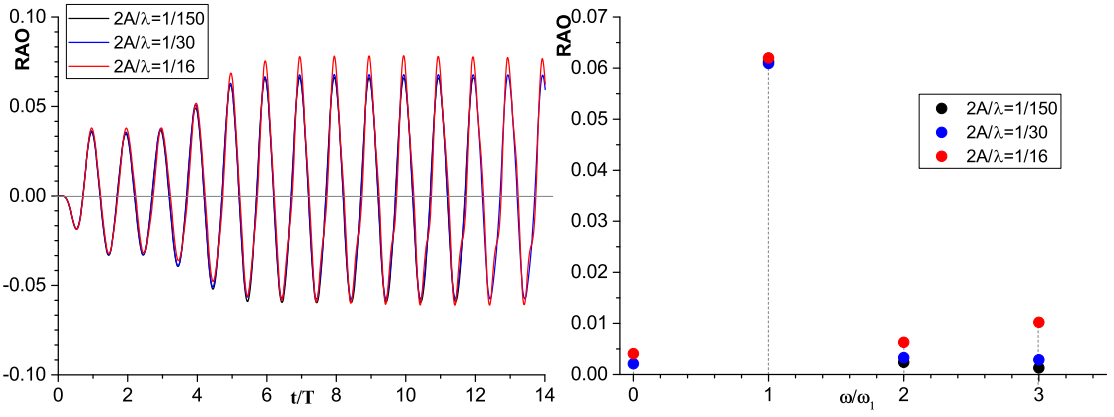

FIGURE 6.6: Time history of non-dimensional heave motion as well as its harmonic components when the *ringing* occurs.

simulation. Since the body is in resonance, even the 2nd-harmonic force or 3rd-harmonic force is a small value at the beginning, the amplitude of motion would increase with time going on. In *springing*, the 2nd-harmonic response is comparable with the the 1st-harmonic, and thus it should be well evaluated in the practical applications.

6.5 Conclusions

As an attempt, ALE-HOBEM is applied to study nonlinear wave interaction with a freely floating body. One DOF heave motion response to steep incident wave is studied. Some preliminary results are provided and validated with available results. The second-order and third-order

motion resonance is studied, which proves that ALE-HOBEM can capture higher-order nonlinearity. Once the high-harmonic force is close to the natural frequency of body, it tends to trigger large-amplitude body motion, even though, the high-harmonic force is a small value at the beginning.

Chapter 7

Conclusions and future work

7.1 Conclusions

A solver named ALE-HOBEM is developed in the present research, which has been applied to study various wave-structure interaction problems. As its name indicates, an ALE-type free surface tracking scheme is adopted in the solver; and a higher-order boundary element method (HOBEM) is used for solving the BVP. In addition, the mutual dependence of fluid body motion is decoupled in an accurate and elegant manner. By means of ALE-HOBEM, we studied nonlinear wave diffraction, wave radiation and wave interaction with a freely floating body (1D-OF). From these applications, we not only test the solver itself but investigate some features of nonlinear wave-structure interaction problem, which are summarized as follows:

a. Taking advantage of ALE scheme, body's geometry above waterline and body's large amplitude motion are taken into account when tracking the free surface deformation. As a consequence, the mesh near waterline can self-adapt to large-amplitude motion and body's complex geometry above waterline. What's more, an exact intersection (waterline) can be captured.

b. The mutual dependence of fluid structure motion is mainly due to hydrodynamic force proportional to body's acceleration. Following the similar idea used for evaluating added mass in infinite domain, the acceleration-related force can be also extracted, which serves as time-dependent added mass and can be put at left-hand side of motion equation. The remaining force is only related to velocity field of fluid and has no coupling effect with body's motion. By means of the proposed method in the dissertation, not only the mutual dependence of fluid structure motion is decoupled but also pressure distribution can be explicitly calculated.

c. As the ALE-type free surface conditions indicate, it requires not only basic solutions of the field, i.e. ϕ and ϕ_n, but first spatial derivative of the solution, i.e. $\nabla\phi$. In the present research, HOBEM is proved to be capable of fulfilling this requirement proposed by ALE scheme. In other words, HOBEM fits well with ALE scheme.

d. Both in diffraction problem and radiation problem, a body with flare around waterline could increase nonlinearity of hydrodynamic performance. The existence of a flare could enhance variation of wetted body surface as well as horizontal projection area of free surface. In addition, the pressure variation around this region is also rapid.

e. In a motion response problem, when incident wave frequency is $1/2$ or $1/3$ of natural frequency of the body. The high-harmonic force would trigger *springing* (double frequency resonance) and *ringing* (triple frequency resonance). Because of the resonance, even a very small high-harmonic force would amplify motion response. In the present research, when the *springing* occurs, the second-harmonic motion is comparable with the fundamental (first-harmonic) motion response.

7.2 Future works

As the title indicates, the present dissertation is trying to solve nonlinear wave-structure interaction by means of numerical computation. Even though the research arrived at the stage of evaluation of wave interaction with a freely floating body, we could only provide very preliminary results. And thus in the near future, an immediate study is to continue the research in Chapter 6 and to extend the present research to more practical applications, which are summarized as follows:

- Nonlinear regular or irregular waves interaction with a floating FPSO in 3DOF.

  This is an immediate extension of the work in Chapter 6. In order to analysis the origin of nonlinear effect, the problem is divided into parts, nonlinear wave diffraction and nonlinear wave radiation. By means of this separation, nonlinear features of exciting force and coupling effect of hydrodynamic coefficient (added mass and damping coefficient) could be studied. With those knowledge in mind, the original problem can be studied and analyzed. In order to carry out in-depth study, the wave field decomposition technique may be used, by which the harmonic free propagation and bounded wave can be separated.

- Study the coupling of sloshing and vessel motion in waves.

  To validate capacity of the ALE-HOBEM, the coupling of sloshing and vessel motion in waves would be studied. This is an extension of above-mentioned work by adding a tank inside of the ship.

- Nonlinear wave interaction with a couple of cylinders.

  This is an extension of work in Chapter 4 to study multi-body interaction (trapping, near-trapping or cloaking).

- Use unstructured mesh on free surface.

- Seek a hybrid scheme to cooperate ALE-HOBEM with other N-S equation based solver.

- Application of ALE-HOBEM to study nonlinear wave-structure interaction taking into account forward-speed effect.

Appendix A

Time-dependent added mass

As mentioned before, ϕ_t is related to acceleration of the body and therefore there is component of total force proportional to acceleration. When designing a numerical scheme, this force component had better extracted and put at left-hand side of motion equation serving as added mass, for the sake of numerical stability. In the following contents, we would introduce an intuitive method to separate inertial force which is proportional to body's acceleration. Note that this method is proposed by Wang (2007) in his master thesis for a 2D problem, and at present we derived this formulation for 3D problem.

The force calculated by Bernoulli's equation is the summation of inertia force, damping force and some other forces. In order to separate the inertia force, we assume the body moves with an infinite acceleration, and as a result the added inertia force play the leading role in the total force. By multiplying a tiny minimum to the total force, other forces approach to zero, and only the inertia force left. Finally, the time-dependent added mass can be obtained.

Suppose at time t_0, the normal velocity on body surface is V_n. A short time later at $t_0 + \delta t$, the normal velocity on body surface is $V_n + \delta V_n$ and the associated normal acceleration can be written as follows,

$$a_n = \lim_{\delta t \longrightarrow 0} \frac{\delta V_n}{\delta t} = \infty \tag{A.1}$$

Taking fully nonlinear 3D wave-body interaction as an example, the velocity potential ϕ is subject to the following BVP

$$\begin{cases} \nabla^2 \phi = 0 \\ \dfrac{\partial \eta}{\partial t} = \dfrac{\partial \phi}{\partial z} - \nabla\phi \cdot \nabla\eta \quad z = \eta \\ \dfrac{\partial \phi}{\partial t} = -g\eta - \dfrac{1}{2}\nabla\phi \cdot \nabla\phi \quad z = \eta \\ \dfrac{\partial \phi}{\partial n} = V_n \quad \boldsymbol{x} \in S_b \end{cases} \tag{A.2}$$

Suppose ϕ_0 is the velocity potential at t_0 and ϕ_1 at $t_0 + \delta t$. At $t_0 + \delta t$, the following BVP holds

$$\begin{cases} \nabla^2 \phi_1 = 0 \\ \eta_1 = (\dfrac{\partial \phi}{\partial z} - \nabla\phi \cdot \nabla\eta)\delta t + \eta_0 \quad z = \eta_1 \\ \phi_1 = (-g\eta - \dfrac{1}{2}\nabla\phi \cdot \nabla\phi)\delta t + \phi_0 \quad z = \eta_1 \\ \dfrac{\partial \phi_1}{\partial n} = \delta V_n + V_n \quad \boldsymbol{x} \in S_b \end{cases} \tag{A.3}$$

where the free-surface conditions are expressed in a finite difference form. Because $\delta t \to 0$, actually $\eta_1 = \eta_0$ and $\phi_1 = \phi_0$ on free surface, namely, the free surface and velocity potential have no change after a infinitesimal time step. And thus, $\delta\phi = \phi_1 - \phi_0$ satisfies the following BVP

$$\begin{cases} \nabla^2 \delta\phi = 0 \\ \delta\phi = 0 \quad z = \eta_0 \\ \dfrac{\partial \delta\phi}{\partial n} = \delta V_n \quad \boldsymbol{x} \in S_b \end{cases} \tag{A.4}$$

$\delta\phi$ and δV_n can be further decomposed by following expression

$$\begin{cases} \delta V_n = \displaystyle\sum_{i=1,6} \delta V_i n_i \\ \delta\phi = \displaystyle\sum_{i=1,6} \delta V_i \delta\phi_i \end{cases} \tag{A.5}$$

where V_i is body velocity at i-th mode. Substituting Eq.(A.4) and Eq.(A.5) into Eq.(A.3) yields

$$\begin{cases} \nabla^2 \delta\phi_i = 0 \\ \delta\phi_i = 0 \quad z = \eta_0 \\ \dfrac{\partial \delta\phi_i}{\partial n} = n_i \quad \boldsymbol{x} \in S_b \end{cases} \tag{A.6}$$

According to Bernoulli's equation, the hydrodynamic force can be written as follows

$$F_i = -\rho \iint (\frac{\partial \phi}{\partial t} + \frac{1}{2}\nabla\phi \cdot \nabla\phi + gz) n_i ds \tag{A.7}$$

Since $a \to \infty$, and thus $F_i \to \infty$. Multiplying δt at both side of Eq.(A.7) yields

$$\delta t F_i = -\rho\delta t \iint \frac{\partial \phi}{\partial t} n_i ds - \rho\delta t \iint (\frac{1}{2}\nabla\phi \cdot \nabla\phi + gz) n_i ds \tag{A.8}$$

The second part of Eq.(A.8) is zero. Eq.(A.8) can be rewritten as follows

$$\delta t f_i = -\rho \lim_{\delta t \longrightarrow 0} \delta t \iint \frac{\partial \phi}{\partial t} n_i ds = -\rho \lim_{\delta t \longrightarrow 0} \iint \delta \phi n_i ds \tag{A.9}$$

where f_i is the associated inertia force.

Substituting Eq.(A.5) into Eq.(A.9) yields

$$\delta t f_i = -\rho \lim_{\delta t \longrightarrow 0} \iint (\sum_{i=1,6} \delta V_i \delta \phi_i) n_i ds \tag{A.10}$$

and divide δt on both sides

$$f_i = -\rho \lim_{\delta t \longrightarrow 0} \sum_{i=1,6} \iint (\frac{\delta V_i}{\delta t} \delta \phi_i) n_i ds \tag{A.11}$$

From Eq.(A.12), it is shown that f_i is proportional to body's acceleration. And the associated time-dependent added mass can be written as follows

$$A_{ij} = -\rho \iint \delta \phi_j n_i ds \tag{A.12}$$

Appendix B

Motion equations

By formulating Newton's second law, i.e., conservation of linear and angular momentum, in a body-fixed coordinate system, the resulting equations of motions could take advantage of ship geometry property. The earth-fixed and body-fixed coordinate systems are illustrated in Fig.B.1.

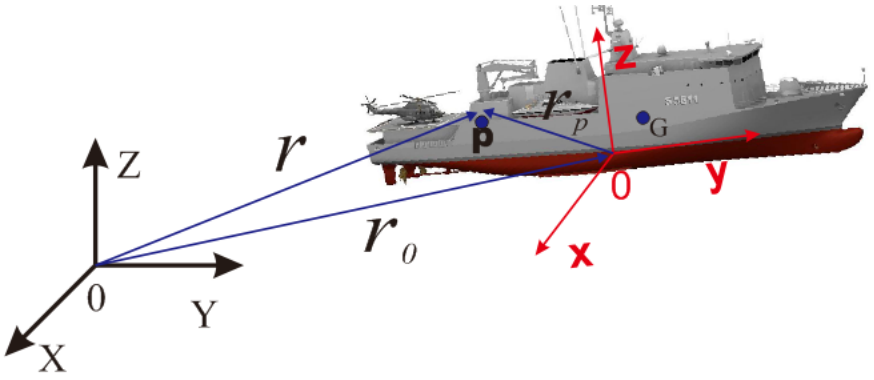

FIGURE B.1: The earth-fixed non-rotating coordinate system XYZ and body-fixed rotating coordinate system xyz and G is center of gravity.

Consider Newton's second law in terms of linear and angular momentum conservation

$$\int_v \frac{d}{dt}(\frac{d\boldsymbol{r}}{dt}\rho)dv = \int_v \rho \boldsymbol{g} dv + \int_s \boldsymbol{f} ds \tag{B.1}$$

$$\int_v \frac{d}{dt}(\boldsymbol{r} \times \frac{d\boldsymbol{r}}{dt}\rho)dv = \int_v \boldsymbol{r} \times (\rho \boldsymbol{g}) dv + \int_s \boldsymbol{r} \times \boldsymbol{f} ds \tag{B.2}$$

where $\boldsymbol{r} = \boldsymbol{r_0} + \boldsymbol{r_p}$ with $\boldsymbol{r_p}$ an arbitrary position vector as defined in Fig.B.1 and ρ is mass density of ship. The forces applied on the ship are divided into volume and surface components denoted with volume integration $\int_v dv$ and surface integration $\int_s ds$, respectively. Time derivative in

both coordinate systems are related by following relation

$$\dot{\boldsymbol{A}} = \acute{\boldsymbol{A}} + \boldsymbol{\omega} \times \boldsymbol{A} \tag{B.3}$$

where $\dot{\boldsymbol{A}}$ is time derivative in earth-fixed coordinate system and $\acute{\boldsymbol{A}}$ is time derivative in body-fixed coordinate system. $\boldsymbol{\omega}$ is the angular velocity vector. Intuitively, suppose $\boldsymbol{r_p}$ is a arbitrary time-independent vector ($\acute{\boldsymbol{r_p}} = 0$) in xyz system, from the point of view of XYZ system, because $\boldsymbol{r_p}$ rotates with xyz system, the time derivative of $\boldsymbol{r_p}$ should be $\boldsymbol{\omega} \times \boldsymbol{r_p}$ i.e., tangent velocity. Note that time derivative of $\boldsymbol{\omega}$ is independent of reference system as indicated below

$$\dot{\boldsymbol{\omega}} = \acute{\boldsymbol{\omega}} + \boldsymbol{\omega} \times \boldsymbol{\omega} = \acute{\boldsymbol{\omega}} \tag{B.4}$$

Evaluating the left-hand-side of Eq.(B.1) yields,

$$\int_v \frac{d}{dt}(\frac{d\boldsymbol{r}}{dt}\rho)dv = \int_v \frac{d}{dt}(\frac{d\boldsymbol{r_0} + \boldsymbol{r_p}}{dt}\rho)dv = \int_v (\dot{\boldsymbol{v_0}} + \acute{\boldsymbol{r_p}})\rho dv \tag{B.5}$$

here $\boldsymbol{v_0} = \dfrac{d\boldsymbol{r_0}}{dt}$ and $\acute{\boldsymbol{r_p}} = \dfrac{d^2\boldsymbol{r_p}}{dt^2}$. Note that in real case the ship's translation velocity $\boldsymbol{v_0}$ is easy to get and the relative position $\boldsymbol{r_0}$ is not our concern. The following useful expression holds

$$\begin{cases} \dot{\boldsymbol{r}}_p = \acute{\boldsymbol{r}}_g + \boldsymbol{\omega} \times \boldsymbol{r_p} = \boldsymbol{\omega} \times \boldsymbol{r_p} \\ \ddot{\boldsymbol{r}}_p = \dot{\boldsymbol{\omega}} \times \boldsymbol{r_p} + \boldsymbol{\omega} \times (\boldsymbol{\omega} \times \boldsymbol{r_p}) \\ \dot{\boldsymbol{v}}_0 = \acute{\boldsymbol{v}}_0 + \boldsymbol{\omega} \times \boldsymbol{v_0} \end{cases} \tag{B.6}$$

Substituting Eq.(B.6) into Eq.(B.5) yields

$$\int_v (\acute{\boldsymbol{v}}_0 + \boldsymbol{\omega} \times \boldsymbol{v_0} + \dot{\boldsymbol{\omega}} \times \boldsymbol{r_p} + \boldsymbol{\omega} \times (\boldsymbol{\omega} \times \boldsymbol{r_p}))\rho dv = \int_v \rho \boldsymbol{g} dv + \int_s \boldsymbol{f} ds \tag{B.7}$$

For ship with constant mass m, $\displaystyle\int_v \dot{\boldsymbol{\omega}} \times \boldsymbol{r_p}\rho dv = \dot{\boldsymbol{\omega}} \times \int_v \boldsymbol{r_p}\rho dv = \dot{\boldsymbol{\omega}} \times m\boldsymbol{r_G}$ with $\boldsymbol{r_G}$ location of ship's center of gravity expressed in body-fixed system. Consider this, Eq.(B.7) simplified to

$$m(\acute{\boldsymbol{v}}_0 + \boldsymbol{\omega} \times \boldsymbol{v_0} + \dot{\boldsymbol{\omega}} \times \boldsymbol{r_G} + \boldsymbol{\omega} \times (\boldsymbol{\omega} \times \boldsymbol{r_G})) = \boldsymbol{f} \tag{B.8}$$

Here f denotes all external force. The derivation of angular momentum conservation in xyz reference takes the similar manner. Consider Eq.(B.2),

$$\int_v \rho \frac{d\boldsymbol{r}}{dt} \times \frac{d\boldsymbol{r}}{dt} + (\boldsymbol{r} \times \frac{d^2\boldsymbol{r}}{dt^2}\rho)dv = \int_v (\boldsymbol{r} \times \frac{d^2\boldsymbol{r}}{dt^2}\rho) = \int_v \boldsymbol{r} \times (\rho \boldsymbol{g})dv + \int_s \boldsymbol{r} \times \boldsymbol{f} ds \tag{B.9}$$

For any constant vector $\boldsymbol{c}$, the equations of linear momentum conservation indicates

$$\boldsymbol{c} \times \{\int_v \frac{d}{dt}(\frac{d\boldsymbol{r}}{dt}\rho)dv - \int_v \rho \boldsymbol{g} dv + \int_s \boldsymbol{f} ds\} = 0 \tag{B.10}$$

Substituting Eq.(B.10) and $\boldsymbol{r} = \boldsymbol{r_0} + \boldsymbol{r_p}$ into Eq.(B.9) yields

$$\int_v \boldsymbol{r_p} \times (\ddot{\boldsymbol{r}}_{\boldsymbol{0}} + \ddot{\boldsymbol{r}}_{\boldsymbol{p}})\rho)dv = \int_v \boldsymbol{r_p} \times \rho \boldsymbol{g} dv + \int_s \boldsymbol{r_p} \times \boldsymbol{f} ds\} \tag{B.11}$$

Substituting Eq.(B.6) into above expression, we finally get

$$\int_v \boldsymbol{r_p} \times (\dot{\boldsymbol{v}}_{\boldsymbol{0}} + \boldsymbol{\omega} \times \boldsymbol{v_0} + \dot{\boldsymbol{\omega}} \times \boldsymbol{r_G} + \boldsymbol{\omega} \times (\boldsymbol{\omega} \times \boldsymbol{r_G}))\rho dv = \boldsymbol{M} \tag{B.12}$$

Here M is external moment. Note that the vector triple product expansion i.e.,

$$\boldsymbol{a} \times (\boldsymbol{b} \times \boldsymbol{c}) = \boldsymbol{b}(\boldsymbol{a} \cdot \boldsymbol{c}) - \boldsymbol{c}(\boldsymbol{a} \cdot \boldsymbol{b})$$

could further simplify terms in Eq.(B.12),

$$\int_v \boldsymbol{r_p} \times (\boldsymbol{\omega} \times (\boldsymbol{\omega} \times \boldsymbol{r_G}))\rho dv = \int_v \boldsymbol{r_p} \times \boldsymbol{\omega}(\boldsymbol{\omega} \cdot \boldsymbol{r_p})\rho dv \tag{B.13}$$

In Cartesian coordinate system, we have, $\boldsymbol{r}_p = x_p\boldsymbol{i} + y_p\boldsymbol{j} + z_p\boldsymbol{k}$ and $\boldsymbol{\omega} = \omega_x\boldsymbol{i} + \omega_y\boldsymbol{j} + \omega_z\boldsymbol{k}$. And the expression can be expanded to yield

$$\begin{aligned}
\int_v \boldsymbol{r_p} \times (\dot{\boldsymbol{\omega}} \times \boldsymbol{r_p})\rho dv &= \int_v (\dot{\boldsymbol{\omega}}(\boldsymbol{r_p} \cdot \boldsymbol{r_p}) - \boldsymbol{r_p}(\boldsymbol{r_p} \cdot \dot{\boldsymbol{\omega}}))\rho dv \\
&= \int_v \{((y_p^2 + z_p^2)\omega_x - x_p y_p \omega_y - x_p z_p \omega_z)\boldsymbol{i} \\
&+ \int_v ((x_p^2 + z_p^2)\omega_y - x_p y_p \omega_x - y_p z_p \omega_z)\boldsymbol{j} \\
&+ \int_v ((x_p^2 + y_p^2)\omega_z - x_p z_p \omega_x - y_p z_p \omega_y)\boldsymbol{k}\}\rho dv \\
&= \boldsymbol{I}\dot{\boldsymbol{\omega}}
\end{aligned} \tag{B.14}$$

where $\boldsymbol{I}$ is the inertia tensor calculated with respect to body-fixed coordinate system.

$$\boldsymbol{I} = \begin{bmatrix} I_{xx} & -I_{xy} & -I_{xz} \\ -I_{xy} & I_{yy} & I_{yz} \\ -I_{xz} & I_{yz} & I_{zz} \end{bmatrix} \tag{B.15}$$

here I_{xx},I_{yy},I_{zz} are the moments of inertia about local ox, oy and oz axes, respectively. And I_{xy},I_{xz},I_{yz} are the products of inertia defined as

$$\begin{aligned} I_{xx} &= \int_v (y_p^2 + z_p^2)\rho dv, & I_{xy} = I_{yx} &= \int_v xy\rho dv \\ I_{yy} &= \int_v (x_p^2 + z_p^2)\rho dv, & I_{yz} = I_{zy} &= \int_v yz\rho dv \\ I_{zz} &= \int_v (x_p^2 + y_p^2)\rho dv, & I_{xz} = I_{zx} &= \int_v xz\rho dv \end{aligned} \tag{B.16}$$

Following the similar procedure yields

$$\int_v \boldsymbol{r_p} \times \boldsymbol{\omega}(\boldsymbol{\omega} \cdot \boldsymbol{r_p})\rho dv = \boldsymbol{\omega} \times (\boldsymbol{I}\boldsymbol{\omega}) \tag{B.17}$$

Applying above definitions, the final expression of angular momentum conservation can be written as

$$m\boldsymbol{r_G} \times \boldsymbol{\acute{v}_0} + m\boldsymbol{r_G} \times (\boldsymbol{\omega} \times \boldsymbol{v_0}) + \boldsymbol{I}\dot{\omega} + \boldsymbol{\omega} \times (\boldsymbol{I}\boldsymbol{\omega}) = M \tag{B.18}$$

Eq.(B.8) and Eq.(B.18) is ship's motion equation expressed in body-fixed frame with arbitrary origin. Obviously, choosing the origin of the body frame to coincide with the center of gravity simplifies the equations.

Bibliographies

[1] M. S. Longuet-Higgins and E. Cokelet, "The deformation of steep surface waves on water. i. a numerical method of computation," in *Proceedings of the Royal Society of London A: Mathematical, Physical and Engineering Sciences*, vol. 350, pp. 1–26, The Royal Society, 1976.

[2] W. Koo and M. Kim, "Fully nonlinear wave-body interactions with surface-piercing bodies," *Ocean Engineering*, vol. 34, no. 7, pp. 1000–1012, 2007.

[3] D. Ning and B. Teng, "Numerical simulation of fully nonlinear irregular wave tank in three dimension," *International Journal for numerical methods in fluids*, vol. 53, no. 12, pp. 1847–1862, 2007.

[4] M. Xue, *Three-dimensional fully-nonlinear simulations of waves and wave body interactions*. PhD thesis, Massachusetts Institute of Technology, 1997.

[5] Y. Liu, M. Xue, and D. K. Yue, "Computations of fully nonlinear three-dimensional wave–wave and wave–body interactions. part 2. nonlinear waves and forces on a body," *Journal of Fluid Mechanics*, vol. 438, pp. 41–66, 2001.

[6] H. Yan, *Computations of fully nonlinear three-dimensional wave-body interactions*. PhD thesis, Massachusetts Institute of Technology, 2010.

[7] W. Bai and R. E. Taylor, "Numerical simulation of fully nonlinear regular and focused wave diffraction around a vertical cylinder using domain decomposition," *Applied Ocean Research*, vol. 29, no. 1, pp. 55–71, 2007.

[8] B. Zhou, D. Ning, B. Teng, and W. Bai, "Numerical investigation of wave radiation by a vertical cylinder using a fully nonlinear hobem," *Ocean Engineering*, vol. 70, pp. 1–13, 2013.

[9] Q. Wang, "Unstructured MEL modelling of nonlinear unsteady ship waves," *Journal of Computational Physics*, vol. 210, no. 1, pp. 368–385, 2005.

[10] H. G. Sung *et al.*, "BEM computations of 3-d fully nonlinear free-surface flows caused by advancing surface disturbances," *International Journal of Offshore and Polar Engineering*, vol. 18, no. 04, 2008.

[11] Q. Ma and S. Yan, "Quasi ALE finite element method for nonlinear water waves," *Journal of computational physics*, vol. 212, no. 1, pp. 52–72, 2006.

[12] C. Zhang, "Application of an improved semi-lagrangian procedure to fully-nonlinear simulation of sloshing in non-wall-sided tanks," *Applied Ocean Research*, vol. 51, pp. 74–92, 2015.

[13] E. F. G. van Daalen, "Numerical and theoretical studies of water waves and floating bodies," *University of Twente*, 1993.

[14] K. Tanizawa, "A nonlinear simulation method of 3-d body motions in waves (1st report)," *Journal of the Society of Naval Architects of Japan*, vol. 1995, no. 178, pp. 179–191, 1995.

[15] G. Wu and R. Eatock Taylor, "Transient motion of a floating body in steep water waves," in *Proceedings of the 11th International Workshop on Water Waves and Floating Bodies (IWWWFB)*, 1996.

[16] G. Wu and R. E. Taylor, "The coupled finite element and boundary element analysis of nonlinear interactions between waves and bodies," *Ocean Engineering*, vol. 30, no. 3, pp. 387–400, 2003.

[17] P. J. Bandyk and R. F. Beck, "The acceleration potential in fluid–body interaction problems," *Journal of Engineering Mathematics*, vol. 70, no. 1, pp. 147–163, 2011.

[18] L. Letournel, G. Ducrozet, A. Babarit, and P. Ferrant, "Proof of the equivalence of Tanizawa–Berkvens and Cointe–van Daalen's formulations for the time derivative of the velocity potential for non-linear potential flow solvers," *Applied Ocean Research*, vol. 63, pp. 184–199, 2017.

[19] P. P. J. F. Berkvens, "Floating bodies interacting with water waves: Development of a time-domain panel method," 1998.

[20] Y. Shirakura, K. Tanizawa, S. Naito, *et al.*, "Development of 3-d fully nonlinear numerical wave tank to simulate floating bodies interacting with water waves," in *The Tenth International Offshore and Polar Engineering Conference*, International Society of Offshore and Polar Engineers, 2000.

[21] G. Wu and Z. Hu, "Simulation of nonlinear interactions between waves and floating bodies through a finite-element-based numerical tank," in *Proceedings of the Royal Society of London A: Mathematical, Physical and Engineering Sciences*, vol. 460, pp. 2797–2817, The Royal Society, 2004.

[22] P. D. Sclavounos, "Nonlinear impulse of ocean waves on floating bodies," *Journal of Fluid Mechanics*, vol. 697, pp. 316–335, 2012.

[23] P. D. Sclavounos and S. Lee, "A fluid impulse nonlinear theory of ship motions and sea loads," *International Shipbuilding Progress*, vol. 60, no. 1-4, pp. 555–577, 2013.

[24] J. L. Hess and A. O. Smith, "Calculation of potential flow about arbitrary bodies," *Progress in Aerospace Sciences*, vol. 8, pp. 1–138, 1967.

[25] H. D. Maniar, *A three dimensional higher order panel method based on B-splines*. PhD thesis, Massachusetts Institute of Technology, 1995.

[26] C. Lee, H. Maniar, J. Newman, and X. Zhu, "Computations of wave loads using a b-spline panel method," in *Proc. of 21st Symposium on Naval Hydrodynamics*, pp. 75–92, 1996.

[27] A. Ginnis, K. Kostas, C. Politis, P. Kaklis, K. Belibassakis, T. P. Gerostathis, M. Scott, and T. Hughes, "Isogeometric boundary-element analysis for the wave-resistance problem using t-splines," *Computer Methods in Applied Mechanics and Engineering*, vol. 279, pp. 425–439, 2014.

[28] M. F. Taus, *Isogeometric Analysis for boundary integral equations*. PhD thesis, 2015.

[29] W. Y. Duan, "Taylor expansion boundary element method for floating body hydrodynamics," in *Proceedings of the 27th International Workshop on Water Waves and Floating Bodies. Copenhagen, Denmark*, 2012.

[30] W. Duan, J. Chen, and B. Zhao, "Second-order taylor expansion boundary element method for the second-order wave diffraction problem," *Engineering Analysis with Boundary Elements*, vol. 58, pp. 140–150, 2015.

[31] T. Rudolphi and F. Rizztr, "A general algorithm for the numerical solution of hypersingular boundary integral equations," *Urbana*, vol. 51, p. 61801, 1992.

[32] A. Frangi and M. Guiggiani, "A direct approach for boundary integral equations with high-order singularities," *International Journal for Numerical Methods in Engineering*, vol. 49, no. 7, pp. 871–898, 2000.

[33] X. W. Gao, "An effective method for numerical evaluation of general 2d and 3d high order singular boundary integrals," *Computer methods in applied mechanics and engineering*, vol. 199, no. 45, pp. 2856–2864, 2010.

[34] X.-W. Gao, W.-Z. Feng, K. Yang, and M. Cui, "Projection plane method for evaluation of arbitrary high order singular boundary integrals," *Engineering Analysis with Boundary Elements*, vol. 50, pp. 265–274, 2015.

[35] J. Harris, E. Dombre, M. Benoit, and S. Grilli, "A comparison of methods in fully nonlinear boundary element numerical wave tank development," *14émes Journées de lHydrodynamique*, 2014.

[36] H. Yan and Y. Liu, "An efficient high-order boundary element method for nonlinear wave–wave and wave-body interactions," *Journal of Computational Physics*, vol. 230, no. 2, pp. 402–424, 2011.

[37] Y. Kim *et al.*, "Artificial damping in water wave problems i: constant damping," *International Journal of Offshore and Polar Engineering*, vol. 13, no. 02, 2003.

[38] Y. Kim *et al.*, "Artificial damping in water wave problems ii: application to wave absorption," *International Journal of Offshore and Polar Engineering*, vol. 13, no. 02, 2003.

[39] M. W. Kim, W. Koo, and S. Y. Hong, "Numerical analysis of various artificial damping schemes in a three-dimensional numerical wave tank," *Ocean Engineering*, vol. 75, pp. 165–173, 2014.

[40] A. Clément, "Coupling of two absorbing boundary conditions for 2d time-domain simulations of free surface gravity waves," *Journal of Computational Physics*, vol. 126, no. 1, pp. 139–151, 1996.

[41] G. I. Jennings, S. Karni, and J. Rauch, "Water wave propagation in unbounded domains. part i: nonreflecting boundaries," *Journal of Computational Physics*, vol. 276, pp. 729–739, 2014.

[42] G. Jennings, D. Prigge, S. Carney, S. Karni, J. Rauch, and R. Abgrall, "Water wave propagation in unbounded domains. part ii: Numerical methods for fractional PDEs," *Journal of Computational Physics*, vol. 275, pp. 443–458, 2014.

[43] J. Spinneken, M. Christou, and C. Swan, "Force-controlled absorption in a fully-nonlinear numerical wave tank," *Journal of Computational Physics*, vol. 272, pp. 127–148, 2014.

[44] Q. Ma, *Numerical simulation of nonlinear interaction between structures and steep waves*. PhD thesis, University of London, 1998.

[45] G. Wu, "Hydrodynamic force on a rigid body during impact with liquid," *Journal of Fluids and Structures*, vol. 12, no. 5, pp. 549–559, 1998.

[46] J. Donea, S. Giuliani, and J.-P. Halleux, "An arbitrary lagrangian-eulerian finite element method for transient dynamic fluid-structure interactions," *Computer methods in applied mechanics and engineering*, vol. 33, no. 1-3, pp. 689–723, 1982.

[47] J. N. Newman, *Marine hydrodynamics*. MIT press, 1977.

[48] J. Newman, "Distributions of sources and normal dipoles over a quadrilateral panel," *Journal of Engineering Mathematics*, vol. 20, no. 2, pp. 113–126, 1986.

[49] H. Li, G. Han, and H. A. Mang, "A new method for evaluating singular integrals in stress analysis of solids by the direct boundary element method," *International Journal for Numerical Methods in Engineering*, vol. 21, no. 11, pp. 2071–2098, 1985.

[50] D. Kim, M. Kim, *et al.*, "Wave-current-body interaction by a time-domain high-order boundary element method," in *The Seventh International Offshore and Polar Engineering Conference*, International Society of Offshore and Polar Engineers, 1997.

[51] P. K. Banerjee and R. Butterfield, *Boundary element methods in engineering science*, vol. 17. McGraw-Hill London, 1981.

[52] A. Gigante, "A general algorithm for multidimensional cauchy principal value integrals in the boundary element method," *Journal of Applied Mechanics*, vol. 57, pp. 907–915, 1990.

[53] B. Teng, Y. Gou, and D. Ning, "A higher order BEM for wave-current action on structures-direct computation of free-term coefficient and cpv integrals," *China Ocean Engineering*, vol. 20, no. 3, pp. 395–410, 2006.

[54] D. Ning, B. Teng, H. Zhao, and C. Hao, "A comparison of two methods for calculating solid angle coefficients in a BIEM numerical wave tank," *Engineering analysis with boundary elements*, vol. 34, no. 1, pp. 92–96, 2010.

[55] V. Mantic, "A new formula for the c-matrix in the somigliana identity," *Journal of Elasticity*, vol. 33, no. 3, pp. 191–201, 1993.

[56] C. Wang, G. Wu, and K. Drake, "Interactions between nonlinear water waves and non-wall-sided 3d structures," *Ocean Engineering*, vol. 34, no. 8, pp. 1182–1196, 2007.

[57] J. D. Fenton, "A fifth-order stokes theory for steady waves," *Journal of waterway, port, coastal, and ocean engineering*, vol. 111, no. 2, pp. 216–234, 1985.

[58] P. Ferrant, D. L. Touzé, and K. Pelletier, "Non-linear time-domain models for irregular wave diffraction about offshore structures," *International journal for numerical methods in fluids*, vol. 43, no. 10-11, pp. 1257–1277, 2003.

[59] G. Ducrozet, A. P. Engsig-Karup, H. B. Bingham, and P. Ferrant, "A non-linear wave decomposition model for efficient wave–structure interaction. part a: Formulation, validations and analysis," *Journal of Computational Physics*, vol. 257, pp. 863–883, 2014.

[60] Y. Saad and M. H. Schultz, "Gmres: A generalized minimal residual algorithm for solving nonsymmetric linear systems," *SIAM Journal on scientific and statistical computing*, vol. 7, no. 3, pp. 856–869, 1986.

[61] L. Sun, J. Zang, L. Chen, R. E. Taylor, and P. Taylor, "Regular waves onto a truncated circular column: A comparison of experiments and simulations," *Applied Ocean Research*, vol. 59, pp. 650–662, 2016.

[62] B. Zhou, G. Wu, and B. Teng, "Fully nonlinear wave interaction with freely floating non-wall-sided structures," *Engineering Analysis with Boundary Elements*, vol. 50, pp. 117–132, 2015.

[63] M. Kashiwagi, "Full-nonlinear simulations of hydrodynamic forces on a heaving two-dimensional body," *Journal of the Society of Naval Architects of Japan*, vol. 1996, no. 180, pp. 373–381, 1996.

[64] G. Wu, "A note on non-linear hydrodynamic force on a floating body," *Applied Ocean Research*, vol. 22, no. 5, pp. 315–316, 2000.

[65] J. Mercier, "Evolution of tension leg platform technology," in *BOSS Conference*, 1982.

[66] O. Faltinsen, J. Newman, and T. Vinje, "Nonlinear wave loads on a slender vertical cylinder," *Journal of Fluid Mechanics*, vol. 289, pp. 179–198, 1995.

[67] O. Faltinsen, "Hydrodynamics of marine and offshore structures," *Journal of Hydrodynamics, Ser. B*, vol. 26, no. 6, pp. 835–847, 2015.

[68] T. Mai, D. Greaves, A. Raby, and P. Taylor, "Physical modelling of wave scattering around fixed FPSO-shaped bodies," *Applied Ocean Research*, vol. 61, pp. 115–129, 2016.